Active Mechanics of Cortical Actin : Geometry and Shape Deformation

by
Pragya Srivastava

A thesis submitted to the Jawaharlal Nehru University
for the degree of Doctor of Philosophy

July 2013

DECLARATION

I, hereby, declare that this thesis is composed independently by me at Raman Research Institute, Bangalore, India, under the supervision of Prof. Madan Rao. The subject matter presented in this thesis has not previously formed the basis of the award of any degree, diploma, associateship, fellowship or any other similar title in any other University.

Prof. Madan Rao
Raman Research Institute

Pragya Srivastava

CERTIFICATE

This is to certify that the thesis entitled **Active Mechanice of Cortical Actin : Geometry and Shape Deformation** submitted by Pragya Srivastava for the award of the degree of DOCTOR OF PHILOSOPHY of Jawaharlal Nehru University is her original work. This has not been published or submitted to any other University for any other degree or diploma.

Dr. Ravi Subramaniam
Director
Raman Research Institute

Dr. Madan Rao
Thesis Supervisor

To my family

ACKNOWLEDGEMENTS

I express my heartfelt gratitude to Madan whose energetic guidance has been a source of encouragement through out. His emphasis on the clarity of concepts and diverse ways of approaching a problem have been greatly useful in showing me the ways of sinking into a problem. Thanks to Jayashree for her caring concerns and welcoming attitude for discussions on academic as well as non-academic matters.

I was fortunate to have the opportunities to discuss with Prof. Sriram Ramaswamy during the course of several projects which added new facets to my understanding about the problems at hand. Discussions with Prof. Yashodan Hatwalne have been immensely helpful in providing valuable insights. I am thankful to Prof. Mohan Balasubramanian who has always been promptly clearing my doubts about the cellular cycle and Fission Yeast. I acknowledge critical inputs provided by Pramod Pullarkat and Satyajit Mayor and their groups, which helped me in developing new perspective on the projects I was involved with.

Soon after joining the group I interacted with wonderful labmates: Kripa, Gayathri, Bhaswati and Abhishek. I would like to specially acknowledge several sets of discussions with Kripa which were of immense help in getting me started. Collaboration with Roie in the inital phase of the work was a great learning experience. Collaborations on experimental systems with Srinivasan and Mithilesh were greatly useful in training me to ask more relevant set of questions about experiments and I thank both for bearing with the curiosity of a beginner. Many thanks to Ananyo and Suropriya for the brilliant discussions. I can not forget acknowledging Anirban, Nitin, Amit, Kabir, Debsankar, Sreekrishna and Debarshini for making the lab a pleasant and enjoyable environment to work in. Thanks to G. Manjunatha for going out of his ways to help me time and again.

I thank my friends Nipanjana, Giri, Renu and especially Habiba for organizing the fun-filled get-togethers and Abhijit for great teas at perfect and imperfect timings. Thanks to little Isa for being the sink of all worries. Many thanks are due to Ms. Ratna Sharma for her

precious lessons in music as well as for radiating positivity through her all-embracing smile since the time I first met her.

I fall short of words to thank the constant support I have found in the special bond that I formed with Anagha and Akhil and I thank them for having tremendous belief in me. Thanks to Pooja and Anupam for being great friends. I would like to express great deal of thanks to T.R. Seshadri and family for always being there ensuring smooth sailing throughout the voyage. Thanks to my lovely sister for lightening my heart with her sparkling smile. Finally I will like to acknowledge the support of every kind that my parents have given me. I thank them for being a constant source of inspiration and for their uncompromised trust in my fledgling flights.

Pragya Srivastava
Bangalore
July, 2013

SYNOPSIS

In this thesis, we study the interplay between cellular shape and the cortical actin. Cortical actin is a thin layer enriched in actin filaments, myosin motors and crosslinkers in the vicinity of plasma membrane which is driven far from equilibrium by constant consumption of ATP. As a result of 'treadmilling' and contractile stresses induced due to the action of myosin motors, both of which are active processes in that they require ATP consumption, active currents and mechanical stresses are generated in cortical actin. Cortical actin along with the plasma membrane engages into mechanical sensing and response during various cellular processes associated with the cell surface including cell migration, endocytosis and interaction with extracellular milieu.

We find that, when the shape of the cells is non-deformable, as is the case for Fission Yeast and a number of bacterial cells, geometry of the cell is crucial in determining the steady state patterns of the acto-myosin filaments. Cellular shape not only influences the possible steady state patterns but also determines the stability of these patterns. When the cellular shape is deformable, the interplay between the cell shape and the cortical actin gives rise to interesting instabilities comprising of the acto-myosin and membrane waves, tubules, and waves with growing amplitudes. Work in this thesis has two main parts. Motivation and results for each part are highlighted as follows :

Dynamics and patterning of the cortical actin on curved, tense membranes

Experiments on the cylindrical Fission Yeast cells, reconstituted cylindrical liposomes and rod-shaped bacteria provided sufficient evidence that the dynamics and patterning of active polar filaments is influenced by the cellular shape. To understand the effect of cell geometry we propose well established active hydrodynamic equations that incorporate couplings between filament orientation and cell geometry. This description naturally leads to the spontaneous formation of stationary or moving rings and cables and asters, as is observed in Fission Yeast and rod-shaped bacteria. We focus on the role of cell radius and acto-myosin contractility in bringing about the transition between various steady state patterns. Formation of the acto-myosin rings in cylindrical Fission Yeast cell typically proceeds by the

nucleation of actin patches and then growth in the form of cables which finally condense into acto-myosin rings. We understand this sequence of transition as a function of acto-myosin contractility, cell radius and the domain area as a nucleation and growth problem. In case of the rod shaped bacteria B. *Subtilis*, anisotropies rooted in the cell wall synthesis machinery provide 'easy directions' that can determine the relative orientation of segments of MreB filaments (homologues of actin in bacterial systems) with respect to the long axis of the cylindrical cells. Taking into account these anisotropies which enter the framework via the parameters of the theory results into moving helical segments on the surface of cylindrical cells.

Rings and asters are obtained as steady state solutions on the surface of cylindrical cells. We ask if these are the stable solutions when the shape of the cell is made spherical. We find that the asters are stable solutions. On the other hand, rings are unstable solutions on the surface of sphere and slide towards the poles. These predictions have also been confirmed in the experiments performed on the Fission Yeast cells of spherical shape, having acquired a spherical shape after the removal of cell wall. These experiments show sliding of the acto-myosin ring under the action of active contractile stresses generated in the ring. Fluorescence images of myosin-II indicate that the active force density along the ring is uniform and the mean force density is constant in time as the ring slides. This allows us to propose a simple mechanical model based on the interplay between acto-myosin contractility and cell geometry in high friction limit. Using this model, we predict linear scaling of the slippage time with the cell radius, also verified from experiments. With the same assumptions about the nature of active contractile stresses, we obtain the dynamics of ring on conical and saddle shaped surfaces. Noticing that the shape of the plasma membrane during budding and cell division can be obtained by combining simple shapes e.g. planar, cylindrical, spherical, cone and saddle shaped we make classify the steady state patterns of acto-myosin filaments on composite surfaces.

Deformable plasma membrane and active cortical actin

When the cellular shape is deformable, active currents and stresses of the cortical actin can induce interesting shape instabilities. Last part of this thesis is a study of interplay

between cortical actin and the shape of plasma membrane. Active stresses generated in the cortical actin can give rise to the membrane deformation leading to acto-myosin mediated instabilities, waves, ruffles and budding in cells. Motivated by these ubiquitous patterns observed in the lamellipodia of the motile and spreading cells, we propose active hydrodynamic equations for the coupled dynamics of active cortical actin and cell membrane shape. We study long wavelength instabilities of a plasma membrane coupled with active cortical actin and find spontaneous emergence of tubules, acto-myosin and membranal waves as well as waves with growing amplitudes. Towards the end of this thesis, we propose active mechanism of deformation of the plasma membrane due to active stresses generated in the cortical actin.

Our results clearly establish an important role played by the cellular geometry in governing the dynamics and patterning of the cortical actin and are supported by the experiments performed on Fission Yeast cells and bacterial systems. We highlight the role of an intimate coupling between the cellular shape and the cortical actin in giving rise to the shape deformations of the plasma membrane. This approach is generic and has the advantage of being applicable to a variety of cellular contexts.

Prof. Madan Rao
Raman Research Institute

Pragya Srivastava

Publications

- R.C. Sarasij, P. Srivastava and M. Rao,
  '*Textured domains on tense surfaces and membranes : Effect of tilt and chirality*',
  Phys. Rev. E **85**, 041920(2012).

- M. Mishra, Y. Huang, P. Srivastava, R. Srinivasan, M. Sevugan, R. Shlomovitz, N. Gov, M. Rao and M. Balasubramanian,
  '*Cylindrical cellular geomtry ensures fidelity of division site placement in fission yeast*',
  J. Cell Sci. **125**, 3850(2012).

- P. Srivastava, R. Shlomovitz, N.S. Gov and M. Rao,
  '*Patterning of polar active filaments on a tense cylindrical mmebrane*',
  Phys. Rev. Lett. **110**, 168104(2013).

- P. Srivastava, A. Maitra, S. Ramaswamy and M. Rao,
  '*Instabilities and kinematic waves in a steadily moving active fluid membrane with in-plane polar order*',
  Manuscript in preparation.

- P. Srivastava and M. Rao,
  '*Axi-symmetric patterns of active polar filaments on spherical and composite surfaces*',
  Manuscript in preparation.

Contents

Chapter 1

Introduction

1.1 Active Matter

Active matter consists of constituent particles that consume energy from an internal pool or ambient medium and systematically give rise to the movement or generate stresses by going through an internal cycle of dissipation. Examples of active matter are found over a vast range of length scales including micron sized cell cytoskeletal system to the bird flocks with length scale of order of a Kilometer. In recent years, active systems have attracted a lot of attention due to their ubiquitous nature, unusual mechanical and rheological properties and the features of pattern formation distinct from their passive counterparts [1]. Some representative examples of active matter consist of bird flocks, fish schools, bacterical suspension, vibrated granular rods, cell cystokeleton and reconstituted active components. Focus of the present work will be on the last two examples of active systems (Fig.1.1 (a)).

Living cells are outstanding example of active matter (Fig. 1.1(a)). Cellular medium is driven far from equilibrium by ATP-dependent molecular machines and the cytoskeletal filaments to bring about the organization as well as to execute various cellular process. There are three kind of cytoskeletal filaments : microtubules, intermediate filaments and actin filaments as shown in (Fig. 1.1(b)). Thin layer just beneath the plasma membrane called the cell cortex, is enriched in actin filaments and myosin motors which regulate the local composition and shape dynamics of the cell surface in a variety of contexts such as cell

division, cell migration and interaction with extracellular environment [2],[3],[4].

In this thesis, we provide a theoretical study of the interplay between cellular shape and the dynamics and patterning of cortical actin. Cellular shape affects the patterning of cortical actin and in turn gets affected by the active current and stresses generated in the cortical actin. We start by giving an overview of the concepts and systems that we will encounter through the thesis.

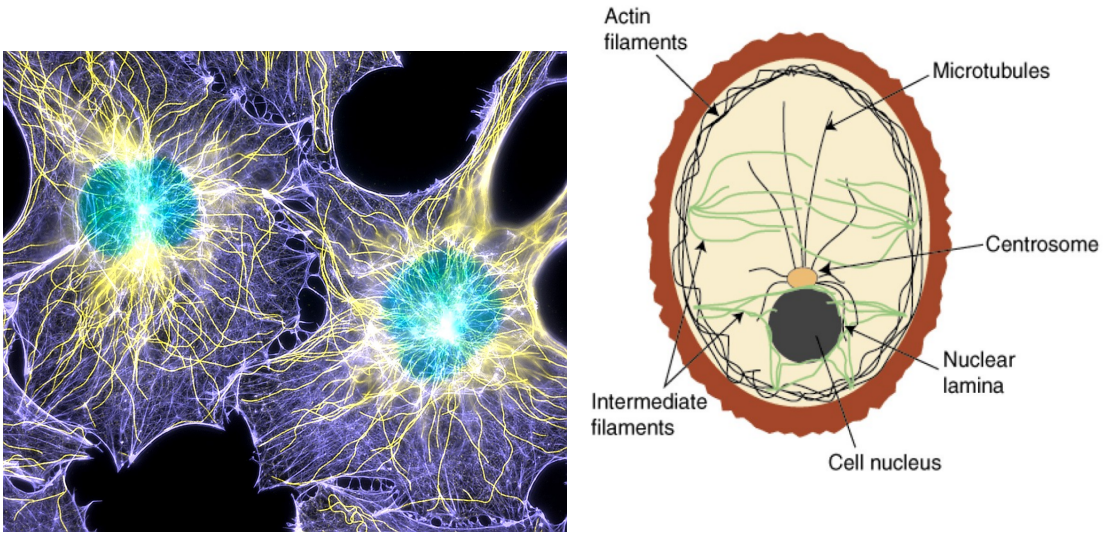

(a) (b)

FIGURE 1.1: (a) Active cellular medium : Components of the cell cytoskeleton. Nucleus is shown in green, microtubules in yellow and actin filaments in purple (Image courtesy : www.cellimagelibrary.org/images/240), (b) Schematic diagram of the cell showing nucleus and the cytoskeleton. Microtubules emanate from the centrosome near the nucleus while actin filaments are nucleated at the plasma membrane. The cell cortex is a dense crosslinked meshwork of actin filaments.

1.2 Cell Cortex as an Active Fluid

At the inner surface of plasma membrane actin filaments are organized in the form of dense crosslinked meshwork : the cell cortex. Nucleation of actin at the plasma membrane is assisted by actin nucleaters such as Arp2/3 and formins, which give rise to the different kind of structures of actin filaments. First step towards the polymerization of actin filaments is formation of a nucleus consisting of three actin monomers. This nucleus then grows by

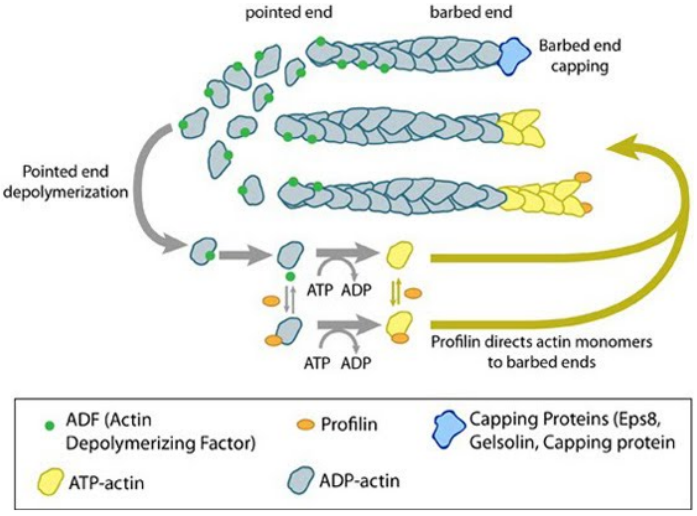

FIGURE 1.2: Polymerization of actin filaments and treadmilling : ATP bound monomers get attached to the barbed end and ADP bound monomers getting detached from the pointed end. In steady state actin filaments reach a constant length and a move with respect to the medium in a process called 'treadmilling'. Profilin enhances the rate of attachment at plus end while the capping proteins are used as length regulators (Courtesy : [4])

fast growth at one end known as the '+' or barbed end and a slower growth at the other, known as the '-' end or pointed end. For the concentration of actin monomers more than a critical concentration, the filament grows. In absence of the ATP hydrolysis the critical concentration beyond which the growth happens, is same at both the ends and the filament either grows or shrinks. ATP hydrolysis leads to a difference in the critical concentrations at the two ends so that there is net attachment at the '+' end and net detachment at the '-' end. In steady state the filament then reaches a steady state length. This process of polymerization makes the actin filaments inherently polar (Fig. 1.2) [4].

In addition to the actin filaments, crosslinkers (e.g. $\alpha-$actinin), motor proteins (e.g. myosin) and linker proteins organize the actin filaments into a dynamic mesh like structure with the thickness in the range of 50-100 nm [5]. Various components of this crosslinked meshwork turn over allowing for the structural relaxation of the network. While typical time scale for the turn-over of actin is in the range of 30-45s, actin crosslinkers and motor proteins turn over typically 5-10 times faster thus leading to the turn over of the whole meshwork at the time scale of less than a minute [5]. At the length scales of the order of microns and time scales of several minutes the cell cortex thus behaves as a two dimensional fluid. In this

thesis, we will be working in these regimes of length and time scales and will treat the cell cortex as an active polar fluid in two-dimension.

1.2.1 Active Stresses and Currents in the Cortical Actin

Another component of the cell cortex are molecular motors e.g. myosin-II that get attached to one or more number of actin filaments (Fig. 1.3). Myosin-II motors attach to actin filaments and walk towards the + end of filament by consumption of ATP. In this process they induce relative torques and relative sliding of actin filaments (Fig. 1.3)[4], thus generating active stresses and currents in a collection of acto-myosin filaments. We now elaborate more on the forms of active current and stresses.

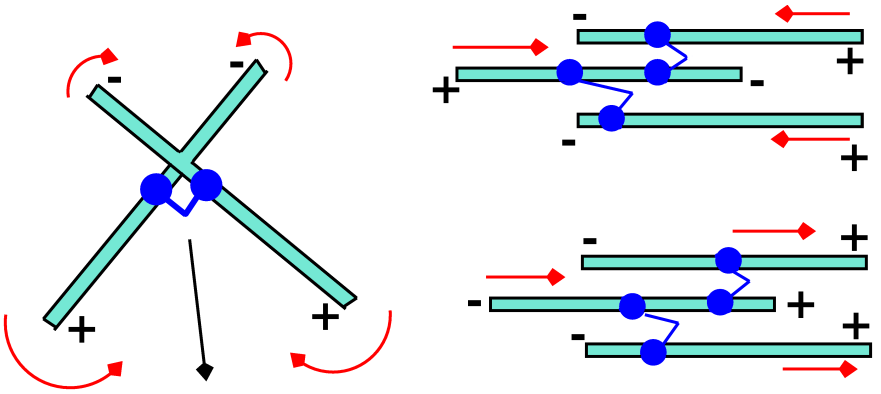

FIGURE 1.3: (a) Two actin filaments bound by myosin-II which walks towards the '+' end of the filaments, thus generating a torque (shown by the red arrows) leading to relative alignment of the filaments, (b) Action of myosin motors on the parallel and anti-parallel bundles of actin filaments : generation of relative sliding and contractile pulling (red arrows).

Active Stresses : Active forces are internal forces and to the lowest order, active particles are force dipoles. Total force in an elemental volume is zero i.e. $\int_\Omega f(\mathbf{r})d\mathbf{r} = 0$ (Fig. 1.4). Active force density thus can be written as $f(\mathbf{r}) = \nabla \cdot \sigma^{\mathbf{a}}$, where σ^a is active stress. Form of the active stress due to active force dipoles has been derived in [6] and is proportional to $Q_{ij} = (n_i n_j - \frac{1}{2}\delta_{ij})$ where $\mathbf{n}$ denotes the averaged polar orientation associated with the acto-myosin particles (Fig. 1.4). Active deviatoric stress σ^a is given as

$$\sigma^a_{ij} = -WcQ_{ij} \tag{1.1}$$

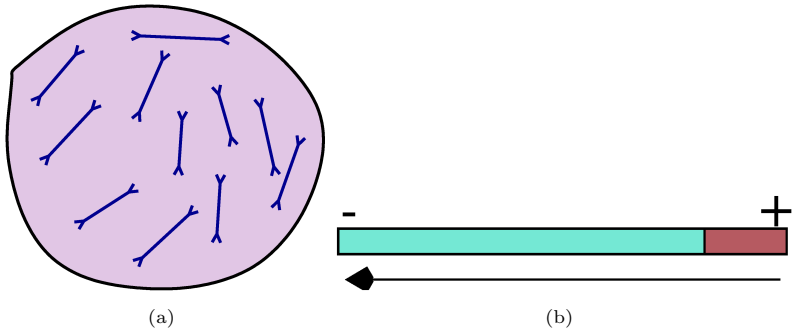

FIGURE 1.4: (a) Collection of acto-myosin filaments : Total force in an elemental volume is zero, (b) polar orientation **n** directed towards the '-' end of filaments.

where $c(\mathbf{r})$ denotes the coarse grained concentration of active particles. Parameter W refers to the extensile ($W > 0$) or contractile nature $W < 0$ of the active filaments. Collection of acto-myosin filaments is an example of contractile systems.

Active Currents : Polar active filaments can move with respect to their surrounding medium with a velocity $\mathbf{v}^a$ proportional to their polar orientation **n**. This relative motion can arise due to a process called 'treadmilling' or it can be motor driven. These two processes result in the relative motion of filaments in following ways :

- *Treadmilling :* As stated earlier, actin polymerization takes place by attachment of ATP bound actin monomers at the + end and ADP bound monomers getting detached from the − end. In steady state, this net assembly of actin monomers at + end and net diassembly of actin monomers at − end leading to movement of the filament with respect to the medium in a process known as 'treadmilling' and is illustrated in (Figs. 1.5(a))[4].

- *Motor driven motility :* Action of myosin-II motors on the actin filaments can also lead to the relative motion of filaments. Fig. 1.5(b) shows the diagram of a motility assay where myosin motors were attached to the glass surface. Actin filaments were added and bound to the myosin motor heads. Upon addition of ATP, actin filaments were moved by the action of myosin motors clearly demonstrating the motor driven motility of actin filaments [4].

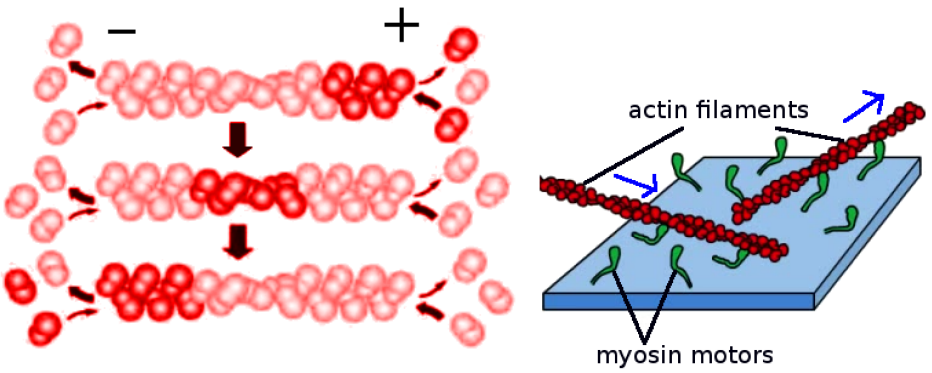

(a) (b)

FIGURE 1.5: (a) Treadmilling : In steady state, a net flux of the monomoers towards the '-' end of the filament leads to relative motion of the filament with respect to the medium (Image courtesy : [4]), (b) Actin motility assay : myosin motors attached to the glass surface move actin filaments upon addition of ATP (Image courtesy : [4]).

Gradients of the active stresses generate flow in the medium which are described by the hydrodynamic velocity $\mathbf{v}$. Due to the contribution from active stresses $\mathbf{v}$ will have terms proprotional to $\nabla \cdot \sigma^a$. Advection of the acto-myosin filaments thus can be because of (a) the velocity associated with the medium that has contributions from the active stress and, (b) relative velocity due to self propulsion of actin filaments coming from the treadmilling and motor driven motility. The second contribution accounting for the relative motion of filaments with respect to the medium will be the dominant one in experimental situations where the selective transport of acto-myosin filaments is observed in a relatively static background. In this thesis we will be dealing with situations where this will be the case, e.g. in Fission Yeast cells where the transport of actin filaments is assisted by the motor proteins such as Myosin-II and Myosin-V [7]. We will focus on the effect of this relative motion on the dynamics and patterning of acto-myosin filaments.

1.2.2 Mechanisms of Dissipation : Viscosity and Friction

Active stresses produced in a collection of acto-myosin filaments get balanced by the dissipative stresses. In the fluid model of cell cortex, there are two sources of dissipation : (a) viscosity and (b) effective friction of the quasi 2-d meshwork. Denoting hydrodynamic velocity by $\mathbf{v}$, the force balance reads :

$$-\nabla \cdot \sigma^a = \eta \nabla^2 \mathbf{v} - \Gamma \mathbf{v} \tag{1.2}$$

where η and Γ are viscosity and friction coefficients. Ratio of the viscosity and friction gives a hydrodynamic screening length scale $l = \sqrt{\frac{\eta}{\Gamma}}$. If length scales involved in the process are much larger than this hydrodynamics screening length friction is the dominant mechanism of dissipation, while for the length scales smaller than l viscosity dominates the dissipation. The dense cortical actin meshwork provides large friction leading to small values of the screening length. We work in the length scales larger than this screening length so that the dominant mechanism of dissipation is the effective friction due to the cell cortex.

1.3 Theoretical Framework : The Active Hydrodynamic Approach

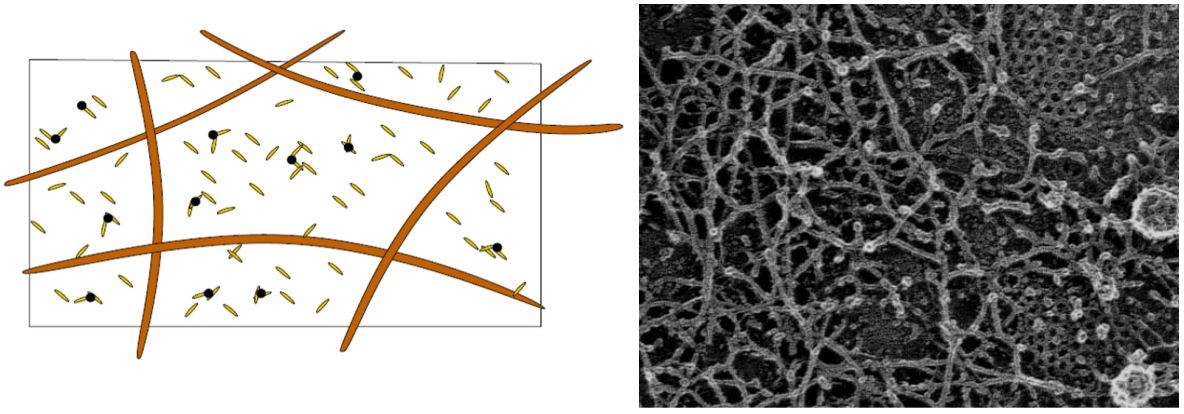

(a) (b)

FIGURE 1.6: (a) Short-dynamic actin filaments (in yellow) crosslinked by myosin (in black) in addition to the relatively static long filaments on the inner side of plasma membrane (Courtesy : [8]), (b) Cryo-electorn micrograph image of the cortex in Normal Rat Kidney cells showing a static crosslinked meshwork (Courtesy : Morone et al, http://www.nanobio.frontier.kyoto-u.ac.jp/lab/slides/4/e.html).

To describe the collection of acto-myosin particles, we follow the well-established framework of 'Active hydrodynamics' which comprises of two steps : (a) identification of the 'slow' variables whose dynamics is slow as compared to microscopic time scales, and (b) proposing the equations of motion for these slow variables using general symmetry based arguments that include all the terms allowed by symmetries upto the lowest orders in fields and gradients.

Because of active driven nature of the systems under consideration, the sign of parameters entering of the theory is not constrained by the requirements of stability. This approach has the advantage of being valid across a variety of systems where context-dependent microscopic details go into setting the parameters.

We display the dynamical equations of motion for the hydrodynamic variables which were proposed in the context of an Active Composite Membrane [2], with a purpose to introduce the theoretical framework. In order to understand the non-trivial features of the organization of the GPI-APs on the plasma membrane of mammalian cells, the notion of *Active Composite Membrane* was proposed by Gowrishankar et al. [2]. The time scales associated with the dynamics of formation and fragmentation of GPI-APs nanoclusters on the plasma membrane were of the order of 1-10s. Experimental evidences suggesting that the patterning and dynamics of GPI-APs was coupled to the cortical actin meshwork motivated the idea of a thin layer of dynamic actin filaments (Fig. 1.6(a)) in addition to the the relatively crosslinked actin meshwork showed by cryo-electron micrographs (Fig. 1.6(b)) [2]. It is at this point that the experimental systems which we will be dealing with in the present thesis differ. Although the notion of an additional layer of dynamic actin filaments need not be invoked in the present work, the underlying theoretical framework is same.

1.3.1 Hydrodynamic Description

First step towards developing the '*active hydrodynamic*' description is to identify the appropriate variables. These variables belong to two categories (a) variables associated with conservation laws, and (b) variables associated with 'broken symmetries' of the system. The time scales under consideration in [2] were less than the turnover time scale so that the total number of acto-myosin filaments in cortex remains constant. The coarse grained concentration $c(\mathbf{r}, t)$ of acto-myosin filaments is thus associated with a conservation law and is defined as

$$c(\mathbf{r}, t) = (1/V)\Sigma_i \delta(\mathbf{r} - \mathbf{r}_i(t)) \tag{1.3}$$

Where V is elemental area of coarse graining.

Another 'slow' variable corresponds to the polar orientation of the dynamic filaments $\mathbf{n}(\mathbf{r}, t)$

which breaks the rotational symmetry in the plane of membrane above a critical density of filaments and, is defined as

$$c(\mathbf{r},t)\mathbf{n}(\mathbf{r},t) = (1/V)\Sigma_i \mathbf{n}_i \delta(\mathbf{r} - \mathbf{r}_i(t)) \tag{1.4}$$

The concentration of acto-myosin filaments denoted by $c(\mathbf{r},t)$ follows a conservation law whose dynamics is given by continuity equation :

$$\frac{\partial c}{\partial t} = -\nabla \cdot \mathbf{J} \tag{1.5}$$

where the current $\mathbf{J} = v_0 c\mathbf{n} - D\nabla c$; $v_0 c\mathbf{n}$ is motor driven active current and D is the diffusion coefficient defined as the trace of diffusion matrix

$$\mathbf{D} = D_{\parallel}\mathbf{nn} + D_{\perp}(\mathbf{I} - \mathbf{nn}) \tag{1.6}$$

Dynamical equation for $\mathbf{n}$ is similar to the Toner-Tu equations [9] and is given by

$$\frac{\partial \mathbf{n}}{\partial t} = -\lambda \mathbf{n}\cdot\nabla\mathbf{n} + K_1\nabla^2\mathbf{n} + K_2\nabla(\nabla\cdot\mathbf{n}) + \alpha(c_0 - c^*)\mathbf{n} - \beta|\mathbf{n}|^2\mathbf{n} + \zeta\nabla c \tag{1.7}$$

Terms on the R.H.S. are contributions from (a) non-linear self advection, (b) active alignment torques, (c) a soft potential $\alpha(c_0 - c^*)\mathbf{n} - \beta|\mathbf{n}|^2\mathbf{n}$ ensuring uniform order above a critical mean concentration c^*, and (d) symmetry allowed coupling to gradients of c.

Equations 1.5 and 1.7 lead to the formation of asters in steady state, for high values of the contractile activity (Fig.1.7). Gowrishankar et al. discuss the patterning of acto-myosin filaments and sequence of transitions in these patterns in planar geometry in detail [10]. Results of this study have successfully been used to explain the dynamics of composition of the plasma membrane [2] as well as to understand the active enhancement of chemical reaction rates at the cell surface [11].

Active currents in cortical actin thus provides a novel mechanism to understand the heterogeneous organization of plasma membrane. In addition, active currents and stresses can get

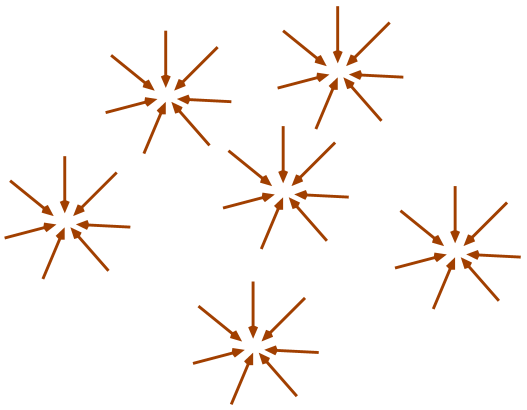

FIGURE 1.7: A collection of asters obtained in steady state shown schematically (Courtesy : [8]).

affected by the geometry of the cell. We now discuss some examples where cellular shape is important to determine the patterning of acto-myosin filaments.

1.3.2 Patterning of Cortical Actin : Substrate Geometry

Fission yeast cells are simple and attractive model to study cell cycle because of their small and well characterized genome. Shape of the Fission Yeast cells is cylindrical with two hemispherical end-caps and is maintained by a rigid cell wall. In planar geometry a collection of acto-myosin filaments has been observed to assemble into a variety of structures including asters, vortices and active networks [12]. In Fission Yeast cells, actin organizes itself into three structures : actin cables, actin rings and actin patches [13]. When cell wall of the Fission Yeast cells is removed they acquire spherical shape. Patterns of the acto-myosin filaments on spherical Fission Yeast cells are rings and patches. Cellular shape not only affects the patterning of acto-myosin filaments, but also the stability of those patterns. Acto-myosin rings formed on the Fission Yeast cells which are not of right shape are not stable leading to failed or inappropriate cell division [14]. Fidelity of the cell division thus crucially depends on the shape of dividing cells.

For large part of this thesis we address the question of dynamics and patterning of acto-myosin filaments on non-deformable curved geometries by generalizing 'active hydrodynamic framework' which explicitly includes the coupling between cortical actin dynamics and the

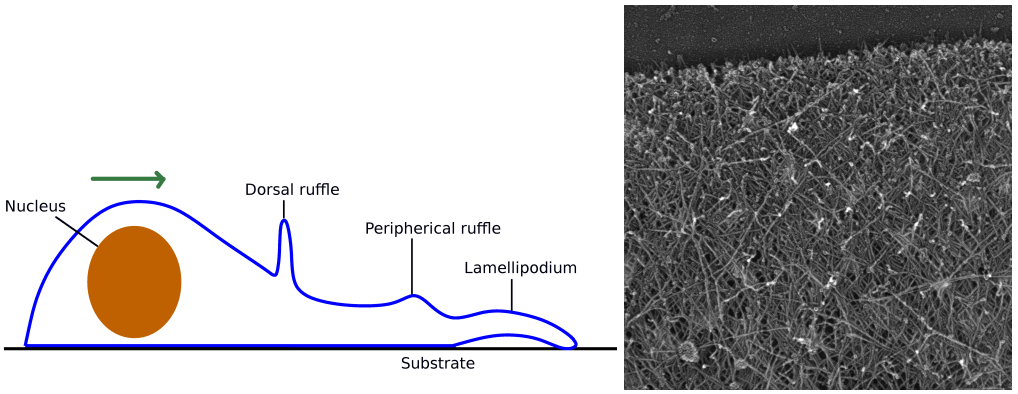

(a) (b)

FIGURE 1.8: (a) Lamellipodia, peripheral and dorsal membrane ruffles are shown schematically in a cell migrating along the direction shown by green arrow. (Courtesy: [15]). Associated actin structures are displayed in Fig. 1.9 (b)Electron micrograph image of the lamellipodia in Xenopus keratocytes, showing highly branched meshwork of actin filaments organized in sheet like structure. (Courtesy : [16])

curvature of the substrate.

When the cellular shape is deformable, dynamics of the shape changes of plasma membrane gets coupled to the active cortical actin. This intimate interplay between acto-myosin contractility and shape changes of the plasma membrane gives rise to the self organized waves and ruffles. We present few relevant examples highlighting the role of active stresses generated in the cortical actin in deforming the plasma membrane.

1.4 Migrating and Spreading Cells

1.4.1 Lateral Membrane Waves and Ruffles

Leading edge of the migrating cells typically has a flat sheet like structure called lamellipodium (Fig. 1.8(a)) which is made up of highly branched actin meshwork (Fig. 1.8(b)) and undergoes rapid turnover. Immediately following this is a structure called lamella which contains actin bundles and myosin-II [15]. These two actin modules regulate the cell motility by co-ordinating actin polymerization in the lamellipodium and the contractile activity in the lamella. Periodic protrusion and retraction of membrane and acto-myosin self organize into lateral membrane waves and ruffles at the leading edge and are ubiquitous patterns of

motile cells [17]. Some common acto-myosin structures and the corresponding membrane shape at the leading edge are displayed in Fig.1.9[15]. A number of studies have identified the dynamics of actin polymerization and the acto-myosin contracility coupled with the traction forces on the substrate, as the regulatory mechanism for the cell motility and the generation of waves and ruffles at the leading edge [18],[19],[20],[21].

Following this, leading edge of the motile and spreading cells can be treated as a thin layer of acto-myosin filaments on a substrate. This layer exhibits waves in the membrane shape as well as the acto-myosin density. We will use these features to build up dynamical equations for membrane shape and the acto-myosin filaments with a purpose to understand the spontaneous emergence of waves, ruffles and other membrane instabilities.

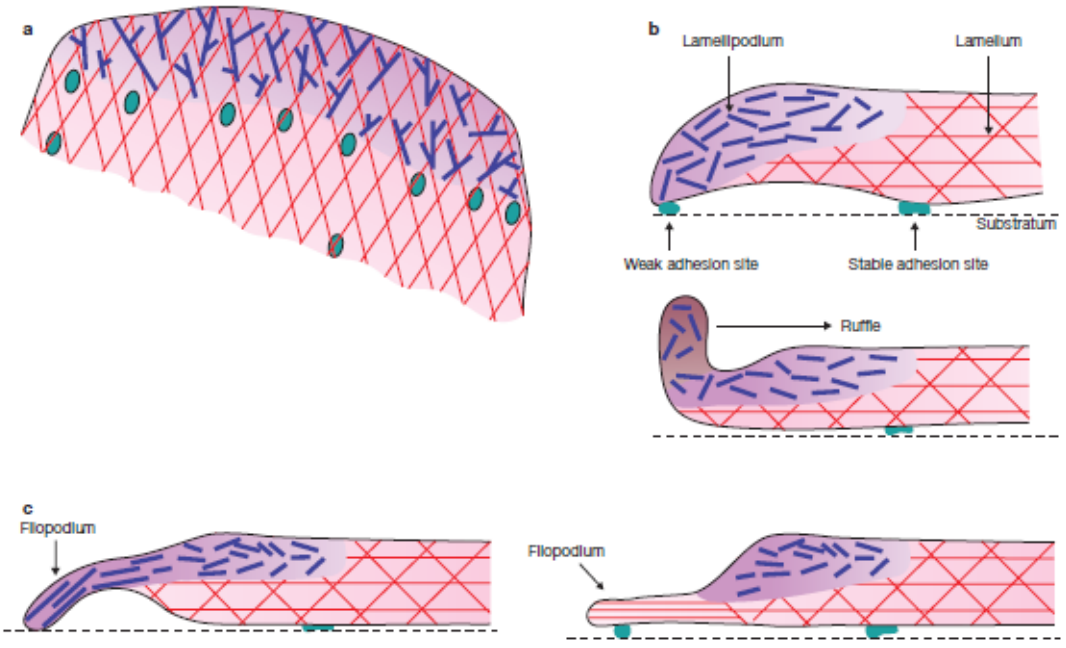

(a)

FIGURE 1.9: Schematic diagrams of the actin structures in lamellipodia, ruffles and filopodia (Courtesy :[15])

1.4.2 Endocytosis

Endocytosis is the process of internalization of plasma membrane with its constituent molecules and surface proteins. The nanoclusters of GPI-APs are internalized by a pathway that is independent of the specific proteins such as clathrin and dynamin and is known as GPI-enriched endocytic compartments (GEEC) pathway. Though the mechanisms of membrane deformation and endosome scission are not properly understood, a number of experiments have established major role played by actin in the GEEC pathway. Direct perturbations to the actin polymerization result in the blocking of the GEEC pathway [22]. Experiments performed by Chadda et al. provide evidence for the GEEC pathway to be based on Cdc42 mediated actin polymerization [22]. Cdc42 is a small GTPase that regulates actin polymerization by binding to N-WASP activating Arp2/3 complex. Since Arp2/3 complex is responsible for branched structure of actin we speculate that the deformation of plasma membrane for GEEC pathway can be caused by the active stresses generated in the cortical actin that is 'horizontal' to it.

Another piece of indirect evidence for the architecture of actin involved in GEEC, comes from the work of Gowrishankar et al. where they clearly demonstrate the major role of active currents in sorting out the membrane proteins and in the formation of GPI-APs nanoclusters. These nanoclusters form at the flat regions of the cells where actin meshwork is horizontal to the plasma membrane [2] which are then endocytosed via GEEC pathway. There can be two possibilities for the mechanism of membrane deformation in the GEEC pathway, (a) passive deformation because of the spontaneous curvature and chiral interactions [23] and, (b) active deformation because of the stresses applied by cortical actin. We propose in this thesis that the localized membrane deformation in GEEC pathway are induced by the active mechanical stresses applied by the horizontal cortical actin.

We now discuss the idea of active membranes which we will encounter in the final chapter of this thesis.

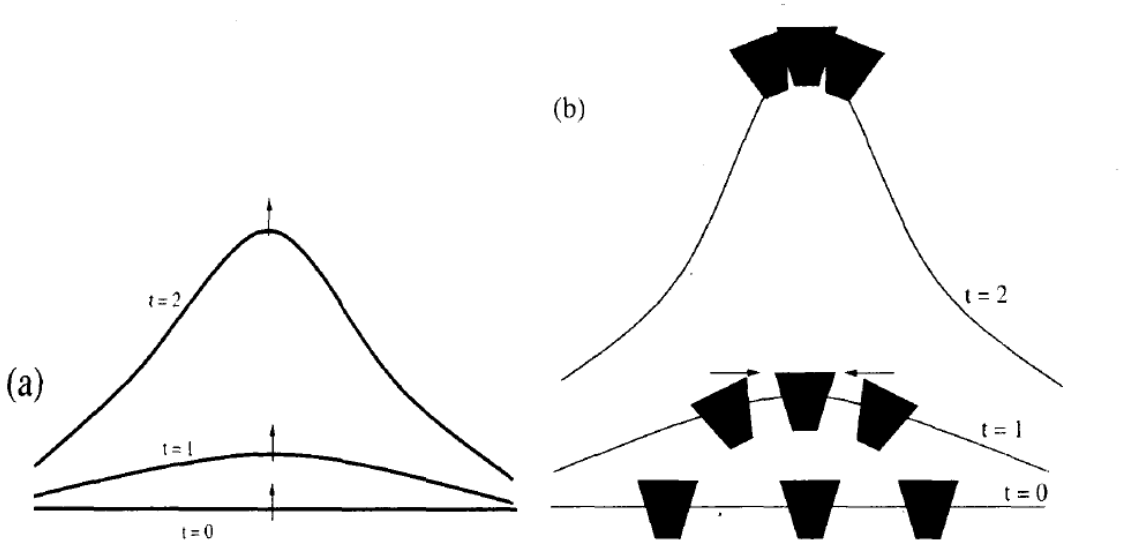

FIGURE 1.10: Mechanisms leading to the instability of an active membrane (Courtesy [26])

1.5 Active Membranes

Studies on the shape fluctuations of the membranes with ion pumps such as bacteriorhodopsin, ion channels and actively generated forces normal to the membrane, motivated the idea of active membranes [24],[25]. Active membranes are membranes with the active force centers withthe direction of active forces normal to the membrane. Depending on the relative orientation of force with respect to the local normal active pumps can be '+pump' or '−'pump. The difference in the number density of ± pumps gives rise to an imbalance density. A coarse grained model based on the coupling between the membrane shape and imbalance density has been constructed in [26]. Pressence of an active pump induces local curvature of a preferred sign in the membrane. For appropriate signs of the local spontaneous curvature and the activity of the pumps active membranes are linearly unstable [26]. The two mechanisms that drive an active membrane to instability are depicted in the Fig. 1.10. In the parameter regime where membrane is stable, activity suppresses the thermal fluctuations of a tensionless membrane. Some examples of active membranes are the membranes with ion pumps and ion channels [26] and a fluid membrane with the active fission and fusion processes [23].

1.6 Theme of the Thesis

In the next chapter, we present an extensive analysis of the steady state patterns on the cylindrical surfaces and predict transitions in these patterns as the cell diameter or motor-driven activity are varied.

In chapter 3, we explore the formation and stability of axi-symmetric patterns on spherical, saddle shaped and conical surfaces. Noticing that the shapes of endocytic buds and the cells undergoing division resemble the composite shapes that can be obtained by combining planar, cylindrical, spherical and saddle shaped geometries, we make predictions about the stability of patterns of acto-myosin filaments. In chapter 4, we describe the experiments on spherical Fission Yeast cells that confirm our predictions on the stability of acto-myosin rings and understand the dynamics of these rings using a mechanical model based on interplay between cell shape and the acto-myosin contractility.

The final chapter presents the analysis of long wave-length instablities of the plasma membrane coupled with the cortical actin network lying horizontal to it and proposes active mechanisms for the deformation of membrane.

Bibliography

[1] M.C. Marchetti, J.F. Joanny, S. Ramaswamy, T.B. Liverpool, J.Prost, M. Rao and R.A. Simha, arXiv:1207.2929.

[2] K. Gowrishankar, S. Ghosh, S. Saha, Ruma C., S. Mayor and M. Rao, Cell **149**, 1353(2012).

[3] J.Allard and A. Mogilner, Curr. Opin Cell. Biol. **25**, 1(2012).

[4] B. Alberts, A. Johnson, J. Lewis, M. Raff, K. Roberts and P. Walter, '*Molecular Biology of the Cell*', 4^{th} edition (2002).

[5] G. Salbreux, G. Charras and E. Paluch, Trends in Cell Biology **22**, 536(2012).

[6] R.A. Simha and S. Ramawamy, Phys. Rev. Lett. **89**, 058101(2002).

[7] J. Huang, Y. Huang, H. Yu, D. Subramanian, A. Padmanabhan, R. Thadani, Y. Tao, X. Tang, R.W. Solnder and M. Balasubramanian, J. Cell Biol. **199**, 831(2012).

[8] K. Gowrishankar, 'Dynamics of Shape and Composition of an Active Composite Membrane', *Thesis Submitted to Jawaharlal Nehru University*(2009).

[9] J. Toner and Y.H. Tu, Phys. Rev. E **58**, 4828(1998).

[10] K. Gowrishankar and M. Rao, arXiv:1201.3938.

[11] A. Chaudhuri, B. Bhattacharya, K. Gowrishankar, S. Mayor and M. Rao, Proc. Nat. Acad. Sci. **108**, 14825(2011).

[12] F. Backouche, L. Haviv, D. Grosswasser and A.B. Grosswasser, Phys. Biol. **3**, 264(2006).

[13] M.L. Pollard, Nat. Education **3**, 53(2010).

[14] M. Mishra, Y. Huang, P. Srivastava, R. Srinivasan, M. Sevugan, R. Shlomovitz, N. Gov, M. Rao and M. Balasubramanian, J. Cell Science **125**, 3850(2012).

[15] E.S. Chhabra and H.N. Higgs, Nat. Cell Biol. **9**, 1110(2007).

[16] T.M. Svitkina and G.G. Borisy, J. Cell Biol. **145**, 1009(1999).

[17] H.G. Dobereiner, B.J. Dubin-Thaler, J.M. Hofman, H.S. Xenias, T.N. Sims, G. Giannone, M.L.Dustin, C.H. Wiggins and M.P. Sheetz, Phys. Rev. Lett. **97**, 038102(2006).

[18] T.D. Pollard and G.G. Borisy, Cell **112**, 4532003.

[19] A. Mogilner and K. Keren, Curr. Biol. **19**, R762(2009).

[20] G. Giannone, B.J.Dubin-Thaler, HG. Dobereiner,N. Kieffer, A.R. Bresnick and M.P. Sheetz, Cell **116**, 431(2004)

[21] D.T. Burnette, S. Manley, P. Sengupta, R. Sougrat, M.W. Davidson, B. Kachar and J. Lippincott-Schwartz, Nat. Cell. Biol. **13**, 371(2011).

[22] R. Chadda, M.T. Howes, S.J. Plowman, J.F. Hancock, R.G. Parton and S. Mayor, Traffic **8**, 702(2007).

[23] M. Rao and Sarasij R.C., Phys. Rev. Lett. **87**, 128101(2001).

[24] J.B. Manneville, P. Bassereau, D. Levy and J. Prost, Phys. Rev. Lett. **82**, 4356(1999).

[25] J.B. Manneville, P. Bassereau, S. Ramaswamy and J. Prost, Phys. Rev.E **64**, 021908(2001).

[26] S. Ramaswamy and M. Rao, C.R. Acad. Sci. Paris,t.2, Series IV, 817(2001).

Chapter 2

Polar Active Fluid on a tense cylindrical membrane

2.1 Shape is Important

Fission Yeast (*S. pombe*) is a well characterized model organism to understand the process of cell division. Fission Yeast is a unicellular organism and its cylindrical shape is maintained by a rigid cell wall. During Cytokinesis, the final stage of cell division, actin filaments, Myosin-II and a number of specific proteins assemble the cytokinetic ring, which then constricts resulting into the two daughter cells. In addition to the acto-myosin rings, acto-myosin filaments also form cables and nodes in a wild type Fission Yeast [1], [2] (Fig. 2.1). A recent study reveals that the formation of acto-myosin rings for cytokinesis proceeds by the nucleation of actin filaments throughout the Fission Yeast cell, which are then '*reeled in*' to the maturing ring via non-medial acto-myosin cables [1]. If the shape of Fission Yeast cell is made spherical then acto-myosin rings do not stably maintain their position and slip towards the poles [3]. This remarkably demonstarates the significance of cell geometry and in general the influence of geometry on the steady state patterns of actin filaments.

Focus of this chapter is on the role of shape in determining the steady state patterns of active polar filaments. We propose a theoretical framework based on the 'Active hydrodynamics' that includes coupling between the cortical actin and cell geometry and is applicable to a

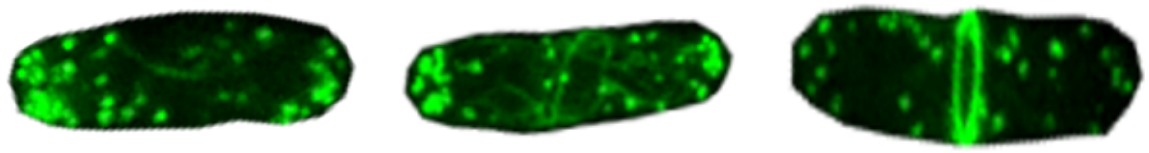

(a) Actin patches (b) Actin cables (c) Actin rings

FIGURE 2.1: Actin labelled with Lifeact is observed to assemble in (a) patches, (b) cables and (c) rings in Fission Yeast cell : [1]

variety of cellular contexts such as : (i) patterning and dynamics of the MreB filaments on rod shaped bacteria *B. Subtillis*, (ii) reconstitued cylindrical liposomes [**?**] and, (iii) FtsZ filaments in bacteria(and reconstituted in yeast). We first propose dynamical equations for the cortical actin in curved geometries using the same approach and asumptions as discussed in the previous chapter.

2.2 General Framework : Curvature Orientation Coupling

As argued in the previous chapter, we describe the cortical actin as a 2-dimensional polar active fluid on the inner surface of a cell. Assuming that the (de)polymerization processes of actin filaments (into)from actin monomers have reached at the steady state, total number of the actin filaments of the steady state length l in the cortex is conserved. The concentration of actin filaments, thus, is a conserved variable and is denoted by $c(\mathbf{r}, t)$. Dynamics of concentration $c(\mathbf{r}, t)$ follows the continuity equation $\partial_t c = -\nabla \cdot \mathbf{J}$, where the operator ∇ is covariant derivative defined on the surface of cell [**?**]. Current for the concentration has following expression

$$J_i = v_0 c n_i + \Lambda_{ij}^{kl} \kappa_k^j c n_l - D \nabla_i c \tag{2.1}$$

R.H.S. of the Eqn. (2.1) has (a) an active contribution due to the ability of filaments to move with respect to the background fluid with a velocity proportinal to $\mathbf{n}$, (b) a symmetry allowed curvature-orientation coupling via phenomenological 4^{th}-rank tensor Λ_{ij}^{kl}, where κ_k^j is the curvature tensor specifying the geometry of the cell, and (c) diffusive current with

the isotropic diffusion coefficient D. The coupling via coefficients Λ renormalizes the active current in Eqn. (2.1) resulting into anisotropic current and is a term of purely active origin. Note that, the diffusion coefficient D can also depend upon the cell geometry which we have ignored in our treatment, while retaining only the lowest order contribution involving the coupling between the polar orientation and cell geometry.

Another slow variable, as described in the first chapter, is the polar orientaion of the actin filaments denoted by $\mathbf{n}$. The dynamics of polar orientation $\mathbf{n}$ of filaments is given by the Toner-Tu equations [5],[6] generalized to include coupling between orientation and the cell geometry

$$\frac{\partial \mathbf{n}}{\partial t} + \lambda \left(\mathbf{n} \cdot \nabla\right) \mathbf{n} \;\; = \;\; K_1 \nabla^2 \mathbf{n} + K_2 \nabla \left(\nabla \cdot \mathbf{n}\right) + \zeta \nabla c + \left(\alpha - \beta |n|^2\right) \mathbf{n} + \boldsymbol{\gamma}\, \boldsymbol{\kappa}\, \mathbf{n} \tag{2.2}$$

The term on L.H.S. with coefficient λ denotes advective non-linearity with $\lambda \neq 1$ as a result of absence of Galilean invariance [5]. Terms on the R.H.S. are explained as follows: (a) $K_{1,2}$ are active torques promoting alignment of neighboring filaments, (b) active motor driven contractility re-orienting $\mathbf{n}$ along the concentration gradients, (c) a term governing the transition from orientationally disordered to polar ordered phase and, (d) a phenomenological coupling between the curvature and polar orientation via coefficient γ. Note that the coupling via parameters γ can be present even in an equilibrium membrane with tilt field [7]. The fourth rank coupling parameters Λ and γ will have 16 components in two dimesions. However the number of non-zero independent contributions of these coupling constants is restricted by the symmetries and the substrate geometry.

As stated in the previous chapter, the hydrodynamic velocity $\mathbf{v}$ is not a slow variable and is determined by the local force balance $\Gamma \mathbf{v} = \nabla \cdot \sigma$ where σ has contibutions from viscous and active stresses. We work in the limit of high friction so that the momentum density does not correspond to a conservation law.

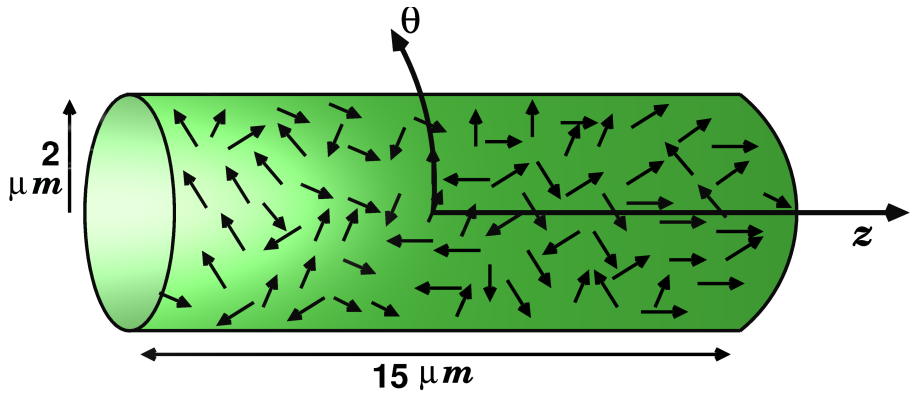

FIGURE 2.2: Polar active filaments on the surface of a cylindrical cell; The dimensions correspond to Fission Yeast cell.

2.3 Patterns on the Cylindrical Cell

The dynamical Eqns. (2.1) and (2.2) in the previous section are proposed on the surface of a cell of arbitrary geometry. We now take the case of cylindrical geometry which is appropriate for the Fission Yeast and obtain the dynamical equations for c and $\mathbf{n}$ (Fig. 2.2) explicitly. First step towards this is to obtain the non-zero and independent components of Λ and γ. We now present the symmetry arguments that restrict the number of non-zero independent components of Λ and γ for cylindrical geometry.

- *Invariance of dynamical equations under $z \to -z$ and $\theta \to -\theta$* : The requirement that the dynamical equations be invariant under $z \to -z$ (reflection about a plane perpendicular to cylindrical axis), and $\theta \to -\theta$ (right/left handedness), forces 8 components of Λ and γ (with indices appearing an odd number of times) to be zero. This leaves 8 non-zero components each : 2 of the form $\left(\Lambda^{zz}_{zz}, \Lambda^{\theta\theta}_{\theta\theta}\right)$ and 6 of the form Λ^{ij}_{ij}, Λ^{ii}_{jj}, Λ^{ij}_{ji} , with $i, j = \theta, z$ and $i \neq j$, where each index appears twice (similarly for γ).

- *Symmetry of κ^i_j* : The fact that the curvature tensor κ^i_j is symmetric under interchange of i, j further restricts the number of independent components of Λ and γ; only 4 of components which have each index (θ, z) appearing twice, are independent (similarly for γ); thus along with the 2 components Λ^{ii}_{ii}, this leaves the net number of independent components to be 6 (similarly for γ).

- *Form of κ^i_j for cylinder* : Finally, upon contracting Λ and γ with the curvature tensor for the cylinder, $\kappa = \begin{pmatrix} 1/R & 0 \\ 0 & 0 \end{pmatrix}$, we find that the number of independent components of Λ and γ appearing in the dynamical equations are only 2, *viz.*, $\left(\Lambda^{\theta\theta}_{\theta\theta}, \Lambda^{z\theta}_{\theta z}\right)$ and $\left(\gamma^{\theta\theta}_{\theta\theta}, \gamma^{z\theta}_{\theta z}\right)$, which we denote as $(\Lambda_\theta, \Lambda_z)$ and $(\gamma_\theta, \gamma_z)$, respectively.

As mentioned in the previous section, the coefficients Λ lead to the anisotropic advective current by renormalizing v_0 to $v_i = v_0 + \frac{\Lambda_i}{R}$. The anistropic current is explicitly dependent on the radius R of the cell. Similarly γ coefficients renormalize the coefficient of linear term in Eqn. (2.2) to $\alpha_i = \alpha + \gamma_i/R - \delta_{i\theta}K_1/R^2$ where δ_{ij} is the Kronecker delta.

Using above arguments the final equations for c and $\mathbf{n}$ are obtained as

$$\partial_t c = D\left(\frac{1}{R^2}\frac{\partial^2 c}{\partial\theta^2} + \frac{\partial^2 c}{\partial z^2}\right) - v_\theta \frac{1}{R}\frac{\partial c n_\theta}{\partial\theta} - v_z \frac{\partial c n_z}{\partial z} \tag{2.3a}$$

$$\begin{aligned}\partial_t n_\theta &= -\lambda\left(\mathbf{n}\cdot\nabla\right) n_\theta + K_1\left(\frac{1}{R^2}\frac{\partial^2 n_\theta}{\partial\theta^2} + \frac{\partial^2 n_\theta}{\partial z^2}\right) + K_2\left(\frac{1}{R^2}\frac{\partial^2 n_\theta}{\partial\theta^2} + \frac{1}{R}\frac{\partial^2 n_z}{\partial\theta\partial z}\right) \\ &\quad + \zeta\frac{1}{R}\frac{\partial c}{\partial\theta} + \left(\alpha_\theta - \beta|\mathbf{n}|^2\right) n_\theta \end{aligned} \tag{2.3b}$$

$$\begin{aligned}\partial_t n_z &= -\lambda\left(\mathbf{n}\cdot\nabla\right) n_z + K_1\left(\frac{1}{R^2}\frac{\partial^2 n_z}{\partial\theta^2} + \frac{\partial^2 n_z}{\partial z^2}\right) + K_2\left(\frac{\partial^2 n_z}{\partial z^2} + \frac{1}{R}\frac{\partial^2 n_\theta}{\partial\theta\partial z}\right) \\ &\quad + \zeta\frac{\partial c}{\partial z} + \left(\alpha_z - \beta|\mathbf{n}|^2\right) n_z \end{aligned} \tag{2.3c}$$

The symbols $v_{\theta,z}$ and $\alpha_{\theta,z}$ are symbols for renormalized parameters and should not be treated as components of a vector.

2.4 Parameters and Units

The dynamical equations are non-dimensionalized by choosing appropriate units for length, time and order parameter,

1. Unit of length, $l = \frac{R}{5}$. Taking $R = 2\,\mu$m for fission yeast [2], this translates to $l = 0.4\mu$m. All length scales are measured in units of l.

Parameters	Physical values	Scaled values
R	2 μm [2]	5 (l)
L	15 μm [2]	$37.5(l)$
D	$0.1 - 1\mu\text{m}^2 s^{-1}$ [8]	$0.625 - 6.25(l)$
v_0	$0.4\ \mu\text{m}s^{-1}$ [9]	$1\ (l/\tau)$
K_1	$0.16\ \mu\text{m}^2 s^{-1}$	$1(l^2/\tau)$
K_2	$0\ \mu\text{m}^2 s^{-1}$	$0(l^2/\tau)$
α	$10\ s^{-1}$	$10(\tau^{-1})$
γ_i	$-20 - 10\mu\text{m}s^{-1}$	$-50 - 25(l/\tau)$
Λ_i	$-0.8 - 1.2\mu\text{m}^2 s^{-1}$	$-5 - 7.5(l^2/\tau)$

TABLE 2.1: Parameter ranges in physical and scaled units

2. Unit of time, $\tau = \frac{R}{5v_0}$. Taking $v_0 = 0.4\mu m s^{-1}$ for fission yeast [9], this translates to $\tau = 1\,\text{s}$. All time scales are measured in units of τ.

3. Unit of magnitude of polarization, $n = \sqrt{\alpha/\beta}$. The values of α and β have been chosen to be large (= 10) and equal so as to ensure that the magnitude of $\mathbf{n}$ is 1 almost everywhere in ordered phase.

To obtain the values of parameters in real units, the number used in the simulation should be multiplied by its appropriate dimension in units of ℓ, τ and n. The values of other parameters chosen for the numerical integration are enlisted in the table.

Note that in the Table (2.1), K_1 has been chosen to be of the same order as D. For simplicity, one constant approximation has been taken, thus $K_2 = 0$. In the analysis that follows we have taken $K_{1,2}$ to be positive thus favoring parallel alignment of filaments. However the steady states that we obtain also admit *anti-parallel* filament orientations if $K_{1,2} < 0$; we then need to augment Eqn.(2.2) by a symmetry allowed 4th-order spatial derivative for stability. Values of γ_i and Λ_i are chosen such that $\frac{\gamma_i}{R}$ and $\frac{\Lambda_i}{R}$ are of same order as α and v_0.

The parameter α is a linear function of mean filament concentration c_0 and governs the transition from orientationally disordered to polar ordered phase. The critical value at which this transition takes place is now curvature dependent. $\zeta > 0$ describes the tendency of contractile filaments to reorient towards the gradient of concentration [10]. Due to activity, the filaments move relative to the solvent in the direction of $\mathbf{n}$, thus reorientation is accompanied by movement of filaments towards each other for $\zeta v_i > 0$ and can be enhanced by

increasing the motor activity. The Eqns 2.3a, 2.3b and 2.3c have large number of parameters, but we restrict ourselves only to the parameters which are both representative and accessible to experimental manipulation. We explore the steady state patterns of active filaments on a cylindrical cell as a function of (i) c_0, (ii) ζ and (iii) cell size R. Having specified the dynamics of cortical actin in terms of the local concentration and polar orientation of filaments we now proceed to determine the stability of homogeneous phases as a function of the parameters mentioned above.

2.5 Spinodal Instability of Homogeneous phases

We first study the spinodal instability of the homogeneous configuration with concentration c_0, which is stable when $\zeta = 0$. At high mean concentration of the actin filaments the uniform phase is orientationally ordered. This transition from orientationally disordered to ordered phase happens when either of α_i becomes positive. Let us write the bare α as $\alpha = \alpha_0 (c_0 - c^*)$ i.e. a function of deviation of mean concentration c_0 from c^* where c^* is the Onsager value of mean density at which disordered to ordered phase transition takes place in planar geometry. Because of the anisotropic renormalization of α as α_i $(i = \theta, z)$, the transition from orientationally disordered to polar ordered phase takes place at different densities and is governed by either of α_i becoming positive. Solving $\alpha_i = \alpha_0 (c_0 - c^*) + \gamma_i/R - \delta_{i\theta} K_1/R^2 = 0$ gives the values of mean density at which α_i become positive. These values of c_0 are plotted as functions of R in the Fig. 2.3 for both the signs of γ_θ and γ_z.

When the filament concentration is low such that $\alpha_i(c_0, R) < 0$, the stable homogeneous phase has no orientational order, $\langle \mathbf{n} \rangle = 0$. As the mean concentration is increased so that either of $\alpha_i(c_0, R)$ becomes positive the homegeneous phase acquires polar orientational order. When $\alpha_\theta > \max(\alpha_z, 0)$ $(\alpha_z > \max(\alpha_\theta, 0))$ the direction of polar order is along θ(z).

To analyze the stability of homogeneous configurations, perturbations to the homoegeneous states are added which are of the form $c(\mathbf{r}, t) = c_0 + \delta c(\mathbf{r}, t)$ and $\mathbf{n}(\mathbf{r}, t) = \mathbf{n}_0 + \delta \mathbf{n}(\mathbf{r}, t)$. The dynamical equations are then expanded to the linear order in perturbation . The perturbations are then decomposed into fourier modes as $\delta c = \Sigma_{\mathbf{q}} c_{\mathbf{q}} e^{i\mathbf{q}\cdot\mathbf{x}}$ and $\delta \mathbf{n} = \Sigma_{\mathbf{q}} \mathbf{n}_{\mathbf{q}} e^{i\mathbf{q}\cdot\mathbf{x}}$,

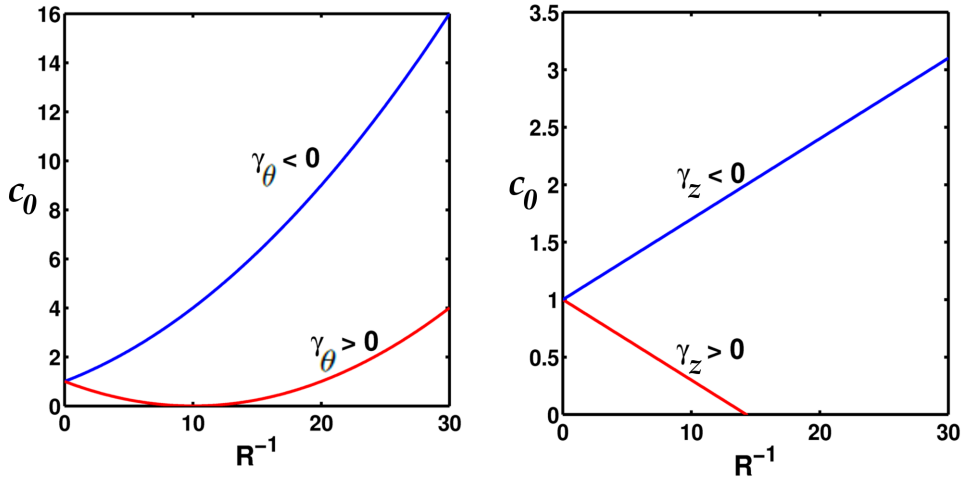

FIGURE 2.3: Phase boundaries for transition from homogeneous disordered phase to uniformly polarized phase oriented along (a) $\hat{\theta}$ and (b) $\hat{z}$ for $\gamma_{1,2} > 0$ (solid red line) and $\gamma_{1,2} < 0$ (solid blue line). c_0 is in the units of c^*.

where $\mathbf{q} = (m\theta, \frac{2\pi l}{L})$, m, l are integers and L is the length of Fission Yeast cell. Eqns. 2.1 and 2.2 can be written in the following matrix form

$$\partial_t \begin{pmatrix} c_{\mathbf{q}} \\ n_{\theta,q} \\ n_{z,q} \end{pmatrix} = \mathcal{M} \begin{pmatrix} c_{\mathbf{q}} \\ n_{\theta,q} \\ n_{z,q} \end{pmatrix} \tag{2.4}$$

Depending on the sign of the real part of eigenvalues of the stability matrix $\mathcal{M}$, the perturbations grow (positive) or decay (negative). A non-zero imaginary part of the eigen values suggests travelling solutions with the amplitudes that again can be unstable or decaying depending on the sign of real part of the corresponding eigen value. The eigen vectors suggest the nature of pattern towards which the homogeneous phase is unstable but does not confirm the final steady state. To obtain the steady state configurations we numerically integrate the dynamical equations for c and $\mathbf{n}$ using an '*implicit and alternating direction method* [11]. This is explained in more detail in a later section of this chapter.

The finite wavevector instability seen in the linear analysis shows up as a density clumping along a specific direction. For the parameter ranges which result in only one maxima in the dispersion surface, the direction of the density clumping is set by direction of the fastest growing wavevector $\mathbf{q}_m$. When $\mathbf{q}_m$ is along z, we obtain *rings*, while when $\mathbf{q}_m$ is along θ, we

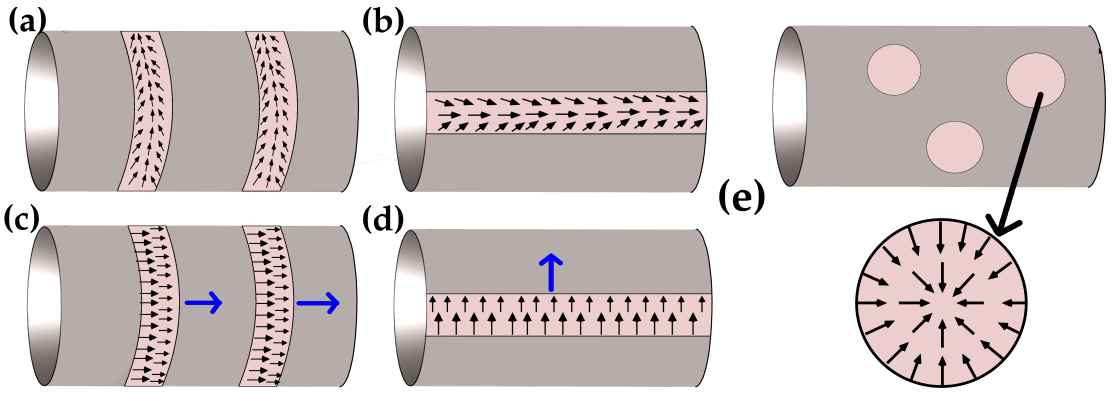

FIGURE 2.4: Schematics of the steady state patterns characterizing the phases obtained as numerical solutions of the dynamical equations : (a) stationary rings, (b) stationary cables, (c) moving rings, (d) moving cables and (e) asters/nodes. Small arrows (black) show texture and thick arrow (blue) denotes the direction of movement of the rings/cables.

get *cables*. For the parameter range where the dispersion surface shows two maxima (along both q_z and q_θ), the final configurations correspond to *asters or nodes*. Stationary rings or cables are different from the moving rings or cables in the steady state arrangement of the orientation vector. Schematic diagrams of all these steady states are shown in the Fig. 2.4. We now examine the instabilities of homogeneous phases.

2.5.1 Low Mean Concentration of the Actin Filaments

We fix the mean concentration c_0 such that $\alpha_i(c_0, R) < 0$ and determine the stability of this state as the contractility ζ is increased. Using linear stability analysis we find that for $\zeta > \zeta_c(\{\alpha_i\}; \{v_i\})$ homogeneous disordered phase is unstable. The stability matrix for the perturbations about homegenous disordered phase has the following expression

$$\mathcal{M} = \begin{pmatrix} -Dq^2 & -ic_0 v_\theta q_\theta & -ic_0 v_z q_z \\ i\zeta q_\theta & \alpha_\theta - Kq^2 - \delta K q_\theta^2 & -Kq_z q_\theta \\ i\zeta q_z & -\delta K q_z q_\theta & \alpha_z - Kq^2 - \delta K q_z^2 \end{pmatrix} \tag{2.5}$$

As mentioned in the previous section, dispersion surface shows single maxima along (a) q_z direction, when $\left|\frac{D\alpha_\theta}{v_\theta}\right| = \zeta_1 > \zeta > \zeta_2 = \left|\frac{D\alpha_z}{v_z}\right|$ and along (b) q_θ direction, when $\left|\frac{D\alpha_z}{v_z}\right| = \zeta_2 > \zeta > \zeta_1 = \left|\frac{D\alpha_\theta}{v_\theta}\right|$. When $\zeta > \max(\zeta_1, \zeta_2)$ the dispersion relation shows two maxima parallel to each q_θ and q_z directions (Fig. 2.5(a)). Since the fastest growing wave vector is either

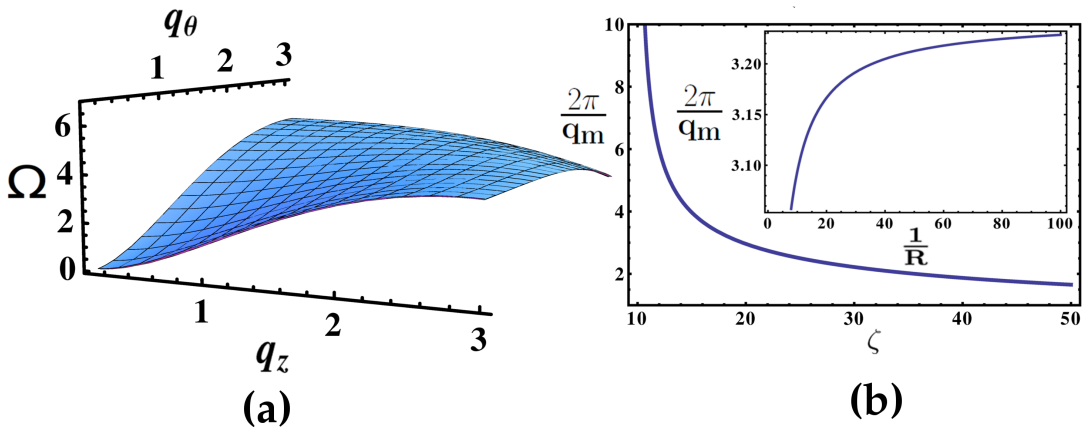

FIGURE 2.5: (a) Dispersion surface showing two maxima; one on q_θ and other on q_z axis, (b) magnitude of fastest growing wave vector with ζ and R(inset).

parallel or perpendicular to the long axis of the cylinder we give the expression of dispersion surface only along q_θ ($q_z = 0$) and $q_z(q_\theta = 0)$ axes.

1. Along q_z axis i.e. $q_\theta = 0$:

$$\Omega = \frac{\alpha_z - D_+ q_z^2}{2} + \frac{1}{2}\sqrt{(\alpha_z - D_- q_z^2)^2 + 4c_0 v_z \zeta q_z^2} \tag{2.6}$$

2. Along q_θ axis i.e. $q_z = 0$:

$$\Omega = \frac{\alpha_\theta - D_+ q_\theta^2}{2} + \frac{1}{2}\sqrt{(\alpha_\theta - D_- q_\theta^2)^2 + 4c_0 v_\theta \zeta q_z^2} \tag{2.7}$$

where $D_+ = D + K_1 + K_2$ and $D_- = D - K_1 - K_2$. Other two modes do not show instability in any parameter regime for $K_{1,2} > 0$. The magnitude of the most unstable wavevector is determined by the maxima of Ω, and is plotted as a function of R and ζ in (Fig. 2.5(b)). This takes a simple form when we set $D_- = 0$,

$$q_m = \frac{1}{2D_+}\sqrt{\frac{c_0^2\zeta^2 v_z^2 - \alpha_z^2 D_+^2}{c_0 v_z \zeta}} \ . \tag{2.8}$$

To know the behaviour of q_m with R and ζ, it is instructive to look at the asymptotic forms of q_m :

1. As $R \to \infty$, $q_m \sim \frac{1}{2D_+}\sqrt{\frac{c_0^2\zeta^2 v_0^2 - \alpha_0^2 D_+^2}{c_0 v_0 \zeta}} + O(\frac{1}{R})$.
2. $q_m \sim \sqrt{\zeta - \left|\frac{D\alpha_z}{v_z}\right|}$, for ζ close to the threshold $\zeta_2 = \left|\frac{D\alpha_z}{c_0 v_z}\right|$.
3. $q_m \sim \frac{c_0 v_z}{2D_+}\sqrt{\zeta}$, for large ζ.

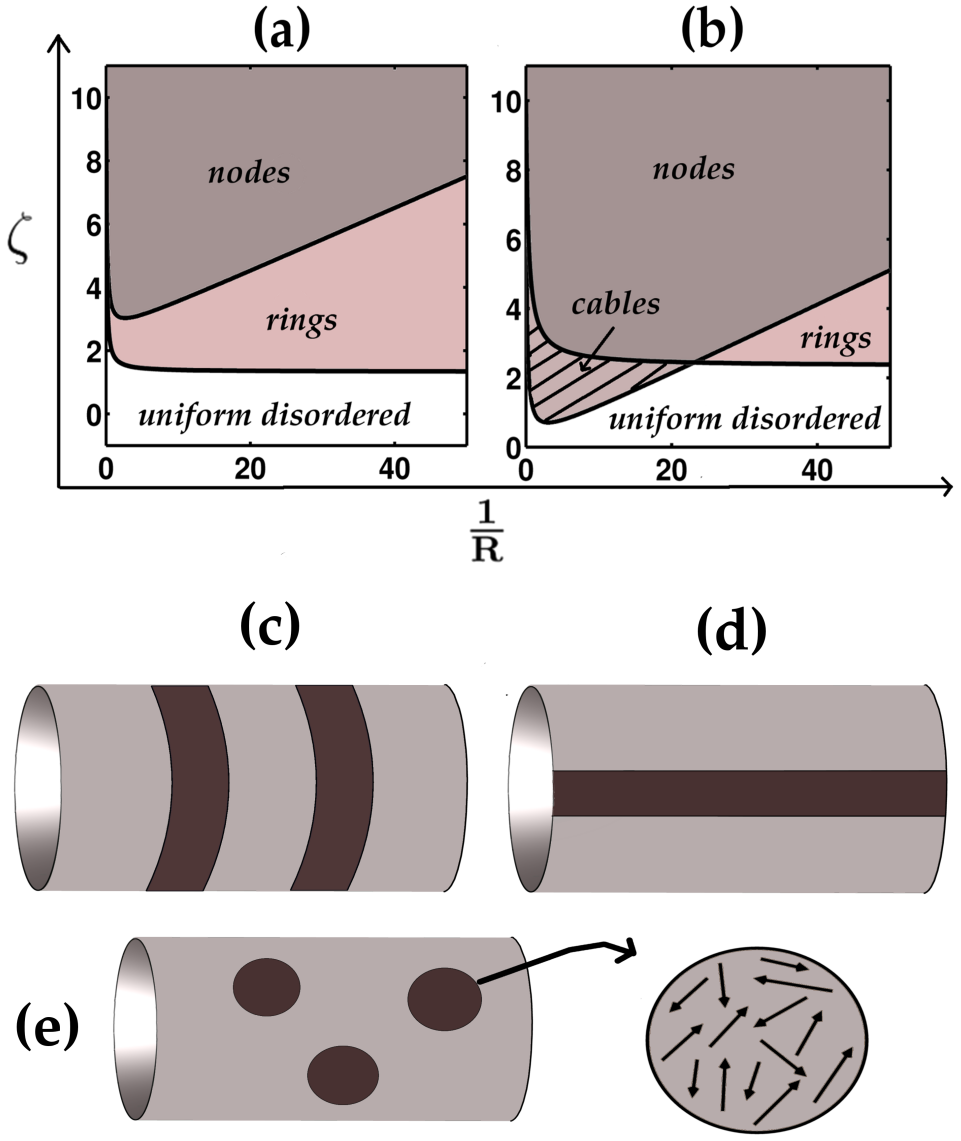

FIGURE 2.6: (a)-(b) Phase diagrams in $\zeta - R$ at low filament concentration, $\alpha_i < 0$, corresponding to zero mean orientation $\langle \mathbf{n} \rangle = 0$. The final steady state configurations obtained from a numerical solution of the dynamical equations for c and $\mathbf{n}$, correspond to (c) rings, (d) cables and (e) nodes. (a) When $\zeta_1 > \zeta_2$, the homogeneous phase is unstable to *rings* and *nodes* as ζ increases, (b) When $\zeta_2 > \zeta_1$, the homogeneous phase is unstable to cables, at large R. As R is lowered, the phase boundaries cross and the sequence of transitions resembles (a).(c)-(e) show schematic diagrams of steady state patterns as obtained from the numerics with (c) rings, (d) cables and (e) nodes.

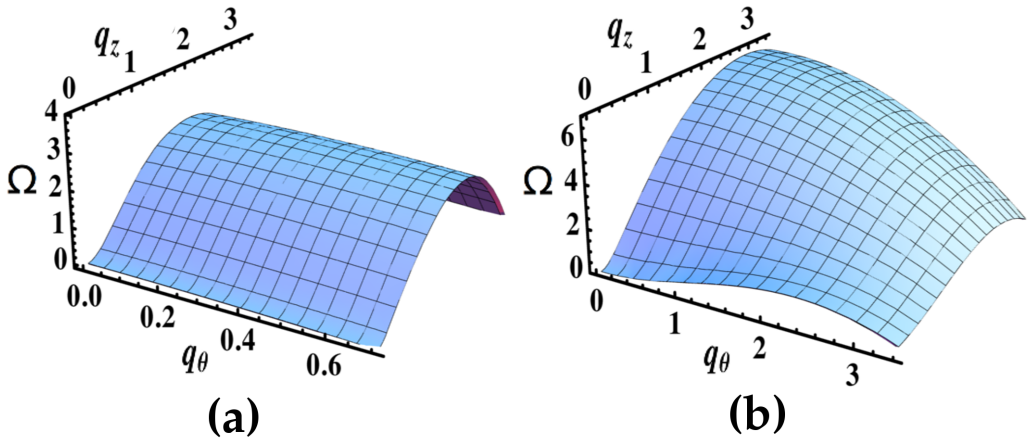

FIGURE 2.7: Dispersion surface showing (a) one maximum on q_z axis, (b) two maxima; along q_θ as well as q_z axes.

The steady state patterns are obtained from numerical integration as mentioned in the previous section. The phase diagram exhibiting various instabilities and corresponding steady state patterns are displayed in the Fig. 2.6. In the next section we proceed to determine the instabilities of homogeneous phase with macroscopic polar order.

2.5.2 High Mean Concentration of the Actin Filaments

In this section we apply perturbation about a uniform phase with mean polar orientation along θ direction which is stable when the mean concentration is such that $\alpha_\theta > \max(0, \alpha_z)$ (in absence of any contractile activity). This homogeneous polar phase becomes linearly unstable to the formation of spatial structures, when ζ is increased beyond a threshold. This result is different from the case of planar geometry where a uniform polar oriented phase is unstable for any non-zero activity [5], [10]. The nature of instability is the same whether $\alpha_\theta > \alpha_z$ or vice versa and hence we discuss only the former case, where we perturb the system around $\mathbf{n}_0 = \sqrt{\frac{\alpha_\theta}{\beta}}\,\hat{\theta}$. The instabilities about this homogeneous ordered phase are obtained as follows :

1. when $\zeta_{c2} > \zeta > \zeta_{c1}$, where $\zeta_{c1} = \frac{D(\alpha_\theta - \alpha_z)}{c_0 v_z}$ and $\zeta_{c2} = \frac{2D\alpha_\theta}{c_0 v_\theta}$, the dispersion surface has only one maxima on q_z axis (Fig. 2.7(a)). The steady state structure obtained in this case consists of periodically separated rings that are stationary. The magnitude of

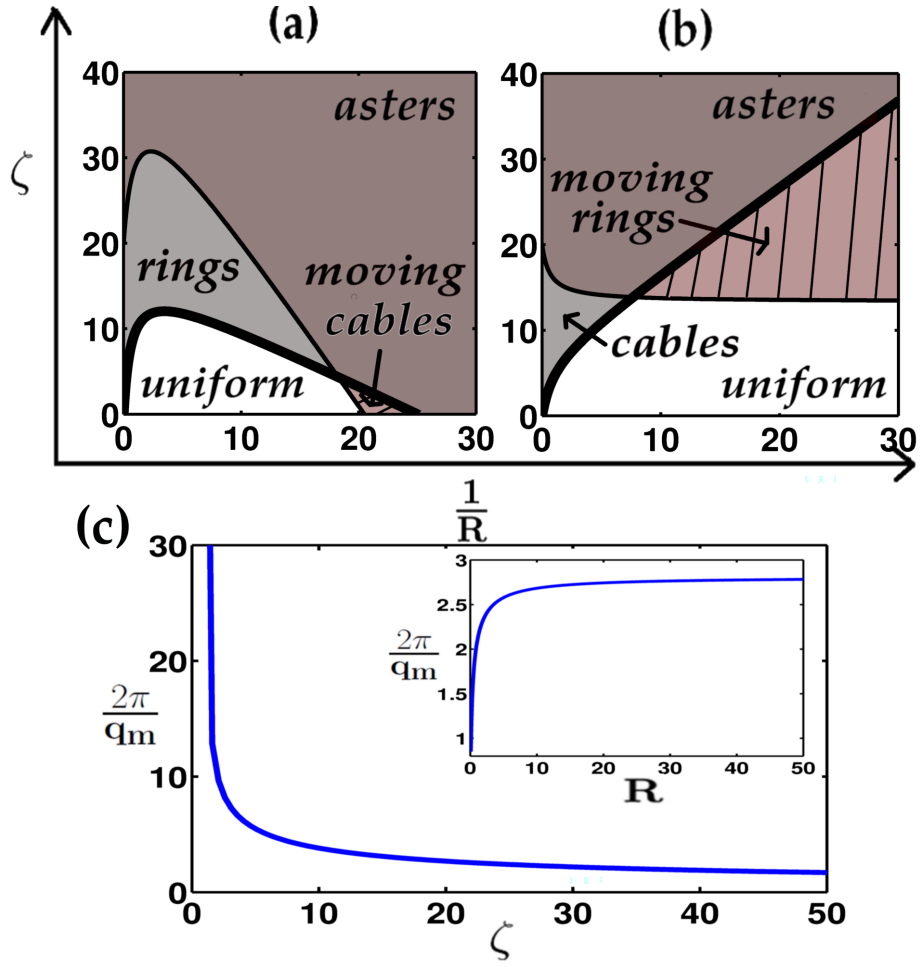

FIGURE 2.8: Phase diagram in $\zeta - R$ at high filament concentration and net mean orientation, obtained from linear stability analysis, for (a) $\alpha_\theta > 0$ and $\alpha_\theta > \alpha_z$ and (b) $\alpha_z > 0$ and $\alpha_z > \alpha_\theta$. The steady state patterns corresponding to these phases are depicted in Fig. 2.4. Uniform phase refers to homogeneous, oriented phase along (a) $\hat{\theta}$ and (b) $\hat{z}$. The phase boundaries in (a) correspond to $\zeta_{c1} = \frac{D(\alpha_\theta - \alpha_z)}{c_0 v_z}$ (thick line) and $\zeta_{c2} = \frac{2D\alpha_\theta}{c_0 v_\theta}$ (thin line), and in (b) correspond to $\zeta_{c1} = \frac{D(\alpha_z - \alpha_\theta)}{c_0 v_\theta}$ (thick line) and $\zeta_{c2} = \frac{2D\alpha_z}{c_0 v_z}$ (thin line). (c) Scaling of the inverse of the fastest growing wavevector q_m with ζ (for fixed $R = 10$) and (inset) with R (for fixed $\zeta = 20$), corresponding to the 'ring' phase in (a)

fastest growing wave vector in this case has following expression in D_- limit, is given by

$$q_m = \frac{1}{2D_+}\sqrt{\frac{c_0^2 v_z^2 \zeta^2 - D_+^2\left(\alpha_\theta - \alpha_z\right)^2}{c_0 v_z \zeta}} \tag{2.9}$$

The corresponding growth rate is given as

$$\Omega = \frac{\alpha_z - a_\theta - D_+ q_z^2}{2} + \frac{1}{2}\sqrt{\left(\alpha_z - a_\theta - D_- q_z^2\right)^2 + 4c_0 v_z \zeta q_z^2} \tag{2.10}$$

The magnitude of fastest growing wave vector has the following asymptotic forms,

$q_m \sim \frac{\sqrt{v_0 \zeta c_0}}{2D_+}\left(1 + \frac{\Lambda_z}{2v_0 R} + \ldots\right)$, as $R \to \infty$, and

$q_m \sim \frac{1}{2D_+}\sqrt{c_0 v_z \zeta} + \ldots$, for large ζ (Fig. 2.8(c))

2. when $\zeta_{c1} > \zeta > \zeta_{c2}$, the dispersion surface has again only one maxima on q_θ axis. The steady state pattern obtained in this case consists of moving cables. Fastest growing wave vector is given by (again for $D_- = 0$)

$$q_m = \frac{1}{2D_+}\sqrt{\frac{\left(\frac{\alpha_\theta}{\beta}(v_\theta - \lambda)^2 - 4c_0\zeta v_\theta\right)^2 - 16D_+^2\alpha_\theta^2}{4c_0 v_\theta \zeta - \frac{\alpha_\theta}{\beta}(v_\theta - \lambda)^2}} \tag{2.11}$$

with growth rate given by

$$\begin{aligned}\Omega \;=\; & \frac{-2\alpha_\theta + D_+ q_\theta^2 - i\sqrt{\frac{\alpha_\theta}{\beta}}\,(v_\theta - \lambda)}{2} \\ & + \frac{1}{2}\sqrt{\left(-2\alpha_\theta + D_- q_\theta^2 + i\sqrt{\frac{\alpha_\theta}{\beta}}\,(v_\theta - \lambda)\right)^2 + 4c_0 v_\theta \zeta q_\theta^2}\end{aligned} \tag{2.12}$$

3. When $\zeta > \max(\zeta_{c1}, \zeta_{c2})$, the dispersion surface shows two maxima (Fig. 2.7(b)). The steady state pattern in this case generically consists of asters.

The corresponding phase diagram is shown in Fig. 2.8(a). For the case when mean density of filaments is such that the uniform phase is polarized along z direction i.e. $\alpha_z > \max(\alpha_\theta, 0)$ we find that uniform polarized phase is unstable towards formation of stationary cables, moving rings and asters. This phase diagram is shown in the Fig. 2.8(b). The Phase boundaries correspond to the onset of instabilities obtained from linear stability analysis. The steady state patterns are obtained from numerical integration of the dynamical PDEs as before.

The magnitude of $\mathbf{q}_m^{-1}$ corresponds to the periodic separation between rings, as verified from a numerical solution of the equations. This quantity has been plotted in Fig. 2.8(c) as

a function of contractility ζ and inverse radius $1/R$. The bahaviour of magnitude of $\mathbf{q}_m$ with ζ and R leads to two testable predictions : (i) the separation between rings increases monotonically with R and saturates to a constant which depends on $\zeta$and (ii) for fixed R , the separation decreases with contractility as $1/\sqrt{\zeta}$ (Eqns.(2.9,2.11)).

While periodicity of the rings and cables is set by the fastest growing wave vector, the size of stationary rings and cables is set by the anisotropic Peclet length, obtained from balancing diffusive and anisotropic advective parts of the current. The velocity of the moving rings or cables is set by the $v_{\theta,z}$ to lowest orders. We present an account of the numerical technique used to integrate the PDEs before going on to study the steady state features of the stationary and moving rings and cables.

2.5.3 Numerical Integration of the Dynamical Equations

As stated earlier, to ascertain the nature of steady state solutions predicted from the linear stability we perform numerical integration of the dynamical equations. We choose the discretization time step $\Delta t = 0.01$ and grid size $\Delta z \sim R\Delta\theta = 0.3$. The units of length scale and time scale are same as chosen in the table 2.1. We then use 'implicit scheme with alternating direction method' to evolve the PDEs. In addition to confirming the nature of steady states in various parameter regimes, we use numerics to explore the axi-symmetric solutions and observe coarsening dynamics.

2.5.4 Axi-symmetric Solutions

In this section, we study the two axi-symmetric solutions, the stationary and moving rings. We determine the width and profile of stationary rings and the velocity of moving rings using simple approximations and motivations from the numerics.

(a) *Stationary rings* : The profiles of concentration and the z-component of polar order for a stationary ring, as obtained from the numerics, are plotted against z-axis in Fig. 2.9. The stationary ring solution can be parametrized as $c(\mathbf{r}) = c(z - z_0)$ and $\mathbf{n} = \mathbf{n}(z - z_0)$. In

this section, we solve for the profiles of c and n_z using an ansatz for n_z motivated from the numerics. Integrating the continuity equation once gives,

$$c = c_0 \exp\left(\frac{v_z}{D}\int n_z dz\right) \tag{2.13}$$

where c_0 is the value of c at the center of ring denoted by z_0. Appropriate boundary conditions on n_z for a stationary ring are $n_z = 1$ at $z - z_0 = -\infty$ and $n_z = -1$ at $z - z_0 = +\infty$. Ansatz for n_z consistent with this is $n_z = n_0 \tanh\left(\frac{z-z_0}{\xi_n}\right)$ where ξ_n is a length scale fixed by the dynamics of $\mathbf{n}$.

$$c = c_0 \left[\cosh\left(\frac{z - z_0}{\xi_n}\right)\right]^{-\frac{v_z \xi_n}{D}} \tag{2.14}$$

consistent with the condition $\partial_z c = 0$ at $z = z_0$. We have matched these profiles with the numerical profiles of c and cn_z by fitting the parameters c_0 and ξ_n for 3 values of Peclét length (Fig. 2.9 (a),(b)). The fitted values of ξ_n for the 3 curves are $3.6, 5.44$ and 9.72. Different values of ξ_n show that ξ_n is not entirely determined by the dynamics of $\mathbf{n}$. This can be due to the strong coupling between the dynamics of c and $\mathbf{n}$ and indicates that the time scales of the two are not simply separated. The approximate functional form of Eqn. 2.14 however fits well with the numerical profile. We plot the full ring-width at half maximum against the Peclet length (Fig. 2.9(c)), which shows a linear increase with D/v_z.

Case 2 (Moving rings) : We obtain the speed of moving rings in a simplified description. The profiles of c and n_z for a moving ring, as obtained from numerics, are shown in Fig. 2.10. Let us consider the equations for c and n_z. Since the magnitude of n_z is unity almost everywhere we drop the non-linear term fixing the magnitude of $\mathbf{n}$. We also keep only the terms that are responsible for pattern formation i.e. we do not include the diffusive terms which go into setting the length scales of the patterns. With these major simplifications and using the ansatz for moving rings, $c = c\,(z - z_0(t))$ and $n_z = n_z\,(z - z_0(t))$ ($z_0(t)$ is the

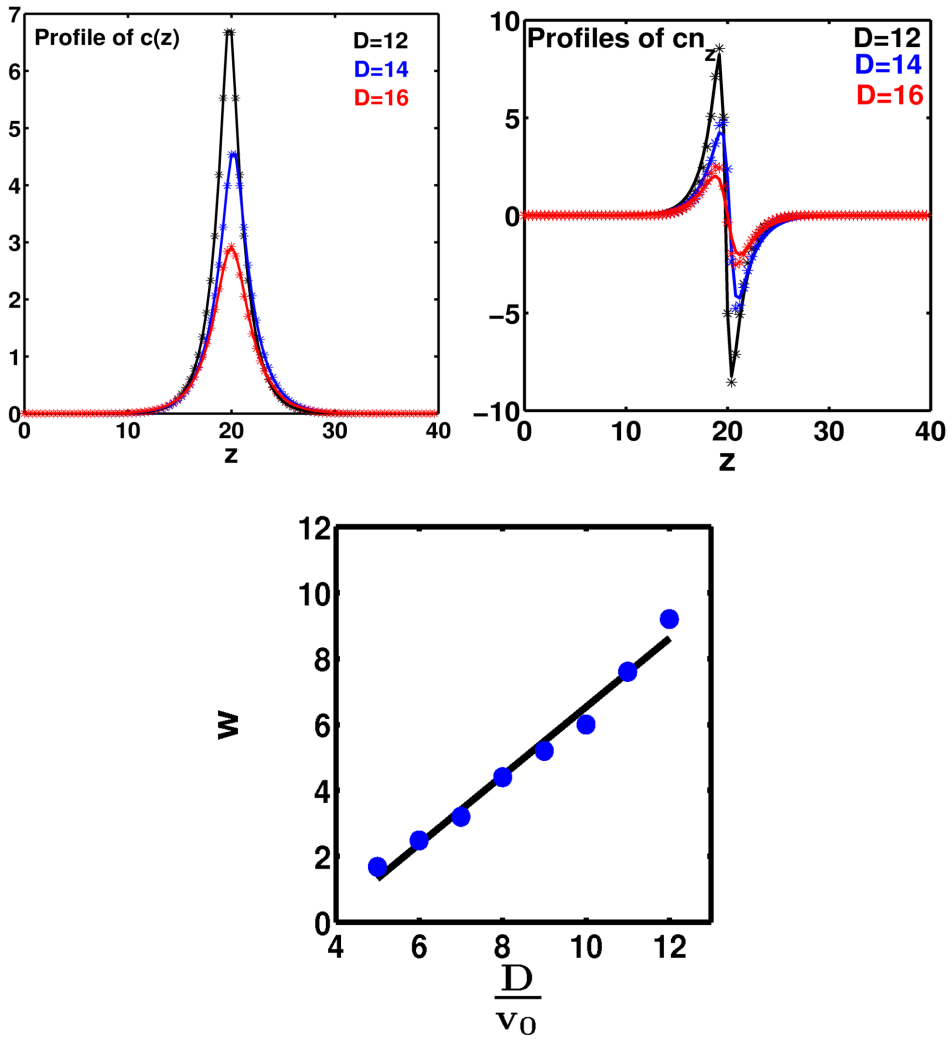

FIGURE 2.9: concentration (a) and orientation profile (b) for a stationary ring for three values of Peclét length. (c) The width of the ring is proportional to the Peclét length.

instantaneous position of moving rings (defined as the location of concentration maximum within the ring), we obtain the following equations

$$\dot{z}_0(t)c' = v_z\,(cn_z)' \tag{2.15a}$$

$$\dot{z}_0(t)n_z' = -\zeta c' + \frac{\lambda}{2}(n_z^2)' \tag{2.15b}$$

Since n_z is unity almost everywhere except at the edge of ring (Fig. 2.10), as first step we assume that n_z is uniformly unity everywhere. This gives, using Eqn. 2.15b, the ring

velocity $\dot{z}_0(t) = -v_z$ to lowest order. Since $v_z = (v_0 + \gamma_z/R)$ increases with decreasing radius as $1/R$, this suggests that the velocity of rings should be higher in smaller rings for fixed value of the coupling parameter γ_z.

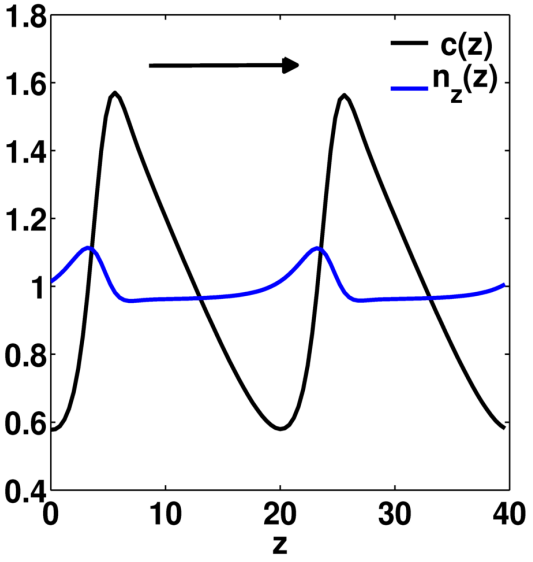

FIGURE 2.10: Profiles of c and n_z for a moving ring.

2.5.5 Coarsening and Ring Merger

The uniform homogeneous phases self assemble into multiple rings or cables as a result of spinodal instability separated by a distance determined by the fastest growing wave vector. In non-linear regime, the proximal rings are observed to merge into each other via a coarsening process, while maintaining the initial ring width (Fig. 2.11). Since the ring width is still primarily being determined by the ratio of diffusive and advective currents, the mechanism of merger is active contractile pulling. Numerical quanitification of the process of ring merger via coarsening is not covered in the present thesis and is taken up elsewhere [12].

2.6 Nucleation and Growth

In the context of fission yeast, assembly of the acto-myosin rings typically proceeds by the nucleation of actin filaments by *formin* nucleators in the form of nodes at non-medial regions

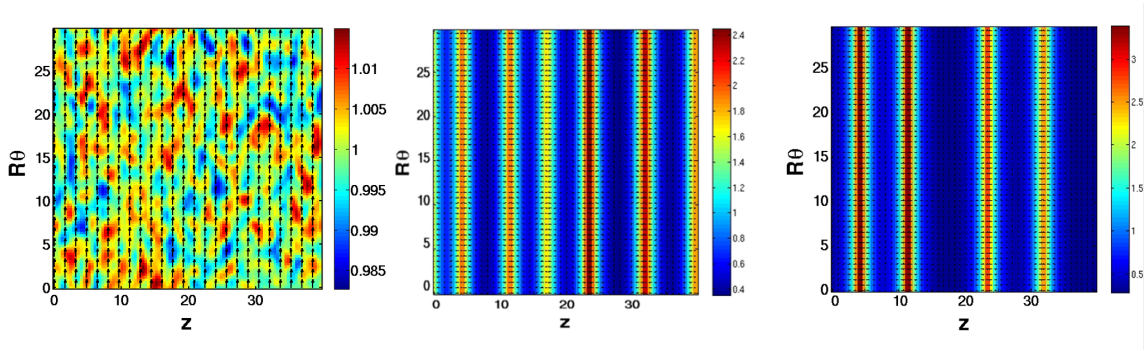

FIGURE 2.11: Time evolution of the configurations starting from an (a) initial homogeneous, orientationally ordered configuration along θ, which shows an (b) early time spinodal instability toward ring formation, followed by a (c) slow coarsening regime. Colorbar denotes the concentration of actin filaments, in units of mean concentration c_0

[1]. Cables then grow from these nodes which are finally incorporated in the acto-myosin ring in myosin-II and myosin-V dependent manner. We study the transition between these domain-shapes (aster→ring or cable-segment, Fig.2.12(c)) using a variational calculation.

Actin nucleation is modeled by a source term in the c-equation. Assuming that the concentration is uniform at c_0, this nucleation leads to increase in area A. The aster size is completely fixed by A, while the dimensions of the ring or cable segments are fixed by A and the width. The width of ring or cable segment is obtained from current balance, and is given by the active Peclét length $D/v_{\theta,z}$. To obtain the texture within the domain $\mathcal{S}$, we note that when $\lambda \to 0$, the steady state solutions of $\mathbf{n}$, Eqn. (2.2), can be obtained as minimizers of an "energy" functional (strictly, a lyapunov functional [13]),

$$E\left[c,\mathbf{n}\right]=\int_{\mathcal{S}}\left[\left(K_1+K_2\right)\left(\nabla\cdot\mathbf{n}\right)^2+K_1\left(\nabla\times\mathbf{n}\right)^2+\zeta c\left(\nabla\cdot\mathbf{n}\right)\right] \tag{2.16}$$

together with a local constraint on the magnitude, $\mathbf{n}\cdot\mathbf{n}\equiv n_0^2=\alpha_{\theta,z}/\beta$. The magnitude of $\mathbf{n}$ is assumed to relax fast to unity and hence the configuration of $\mathbf{n}$ can described by an angle field $\Phi(\mathbf{r})$. In one constant approximation $K_1=K_2=K$

$$E[c,\mathbf{n}]=\int_{\mathcal{S}}\left[K(\nabla\Phi)^2+\zeta c\nabla\cdot\mathbf{n}\right] \tag{2.17}$$

We now calculate "energies" for the three configurations (a) aster (E_a) (b) ring segment (E_θ) and (c) cable segment (E_z).

1. Aster : – For an aster configuration, the angle field $\Phi(\mathbf{r})$ can be parametrized by $\Phi = \phi + \pi$ where ϕ is the angle measured from the cylindrical long axis. For uniform concentration in the aster, $c = c_0\left(1 - H(r - \sqrt{\frac{A}{\pi}})\right)$ where r is the distance measured from the core of aster, A is the area and $H(r)$ denotes the heaviside function. Because of the uniform concentration, the second term in Eqn. 2.17 has contributions only from the edge. The functional E for an aster then is computed as follows :

$$\begin{aligned} E_a &= K\int_{\xi}^{\sqrt{A/\pi}} (\nabla\Phi)^2 r dr d\phi + \zeta\int_{\mathcal{S}} c\nabla\cdot\mathbf{n} \\ &= \pi K \log\frac{A}{\pi\xi^2} + \zeta\left[\int c_0\mathbf{n}\cdot\mathbf{N}dl - \int \mathbf{n}\cdot\nabla c\right] \\ &= \pi K\log\frac{A}{\pi\xi^2} - 2\pi\zeta c_0\sqrt{\frac{A}{\pi}} - 2\pi\zeta\int c_0\delta\left(r - \sqrt{\frac{A}{\pi}} r dr\right) \\ &= \pi K\log\frac{A}{\pi\xi^2} - 4\pi\zeta c_0\sqrt{\frac{A}{\pi}} \end{aligned} \tag{2.18}$$

   where ξ and ϵ_c are the core size and energy, respectively. Note that E_a is the same as in a planar geometry, as expected since the gaussian curvature of a cylinder is zero [14].

2. Ring/Cable segment : – The width of ring(cable)-segment is fixed by the anisotropic Peclét length $\frac{D}{v_z}\left(\frac{D}{v_\theta}\right)$, as mentioned earlier. The angle field Φ within a ring segment with the texture shown in Fig. 2.12(c) will only be a function of z and can be parametrized as $\Phi(z) = \frac{\pi}{2} + \frac{\pi}{w}(z - z_0)$, where w is the width of ring segment. The lyapunov functional for the ring segment is then computed to be

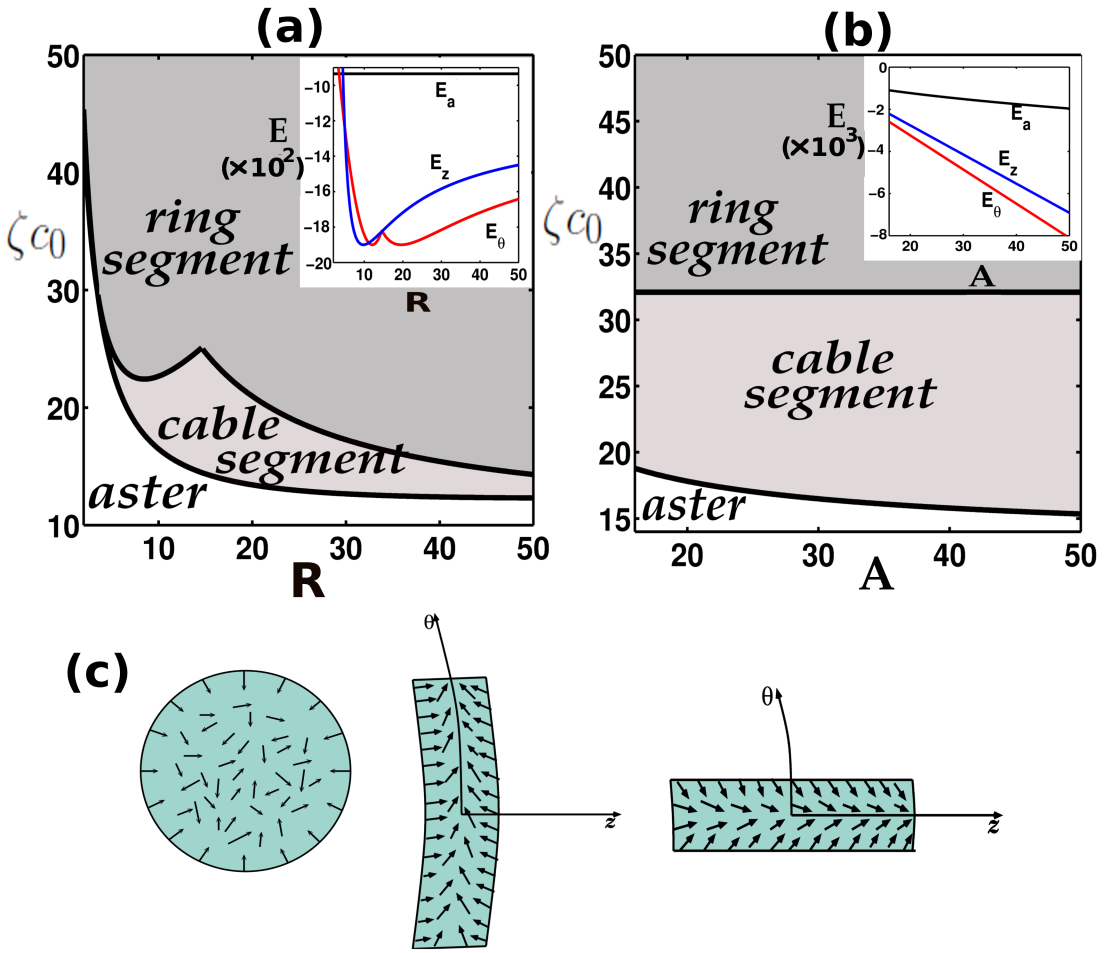

FIGURE 2.12: Phase diagram in ζc_0 versus (a) R (at constant A=30) and (b) A (at constant R=10) showing asters (nodes), ring-segment and cable-segment. Insets show the "energy" branches (units of K) of the 3 configurations, Eqns.(2.18,2.19,2.21). The energy branches in the insets have been plotted for (a) $\zeta c_0 = 25$, and (b) $\zeta c_0 = 40$. Note that the form of E_θ in Eqn. (2.19) is valid for a ring-segment of width D/v_z, which does not encircle the cylinder. For smaller values of R (below the kink in (a)), the ring-segment completely encircles the cylinder, its width is now set by $A/2\pi R$ and the "energy" functional is now given by Eqn. (2.20). The orientation of $\mathbf{n}$ in these configurations are shown in (c).

$$\begin{aligned} E_\theta &= K\int_{\mathcal{S}} (\nabla\Phi)^2 R d\theta dz + \zeta c_0 \int_{\mathcal{S}} \mathbf{n}\cdot\mathbf{N} dl \\ &= K\frac{\pi^2}{w^2}A - 2\zeta c_0 \frac{A}{w} \\ &= \left[K\frac{\pi^2}{D^2}\left(v_0 + \frac{\Lambda_z}{R}\right)^2 - 2\zeta\frac{c_0}{D}\left(v_0 + \frac{\Lambda_z}{R}\right)\right] A \end{aligned} \tag{2.19}$$

Note that, this expression is valid only for a ring segment which does not encircle the cylinder. For a ring segment that has grown into a ring enclosing the cylinder,

increasing the area further will lead to the increase in width (since the ring length is now same as the perimeter of the cylinder). The width is no longer determined by the balance of currents but by the ratio of total number of filaments and the perimeter of cylinder. In this case the relative contributions from bulk and surface terms will be different and the functional in this case is computed as

$$E_\theta = 4K\frac{\pi^4}{A}R^2 - 4\pi\zeta c_0 R \tag{2.20}$$

On similar lines "energy" of a cable segment is calculated as

$$E_z = \left[K\frac{\pi^2}{D^2}\left(v_0 + \frac{\Lambda_\theta}{R}\right)^2 - 2\zeta\frac{c_0}{D}\left(v_0 + \frac{\Lambda_\theta}{R}\right)\right]A \tag{2.21}$$

The "energy" branches E_a, E_θ and E_z are plotted as function of cylinder radius R and the area A in insets of Fig. 2.12 (a) and (b). The phase diagrams based on this are displayed in Fig. 2.12. A typical nucleation and growth scenario would correspond to a trajectory in the $(\zeta c_0, A)$ plane and shows the transition between node→cable-segment→ring-segment seen in the experiments [1].

2.7 Helices on the Cylinder

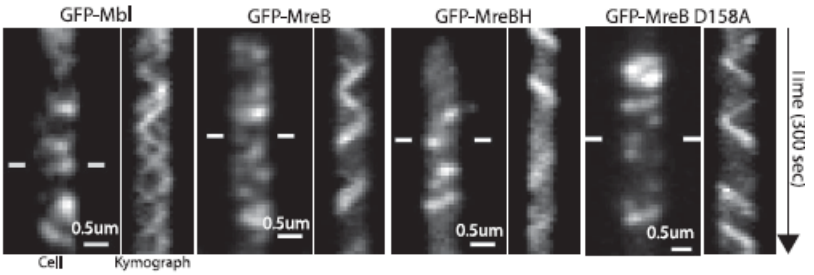

FIGURE 2.13: Circumferential and helical movements of MreB filaments during the cell growth in the bacteria *B.Subtilis* (Courtesy : [17]).

Cellular shape in the baterial systems is determined by the rigid cell wall which is crosslinked meshwork made up of peptidoglaycan (PG) and MreB-cytoskeleton. MreB filaments are the homologues of actin filaments in bacterial systems and are intimately linked to cell-wall synthesis enzymes during cell growth [15]. MreB filaments are strongly coupled with the cell

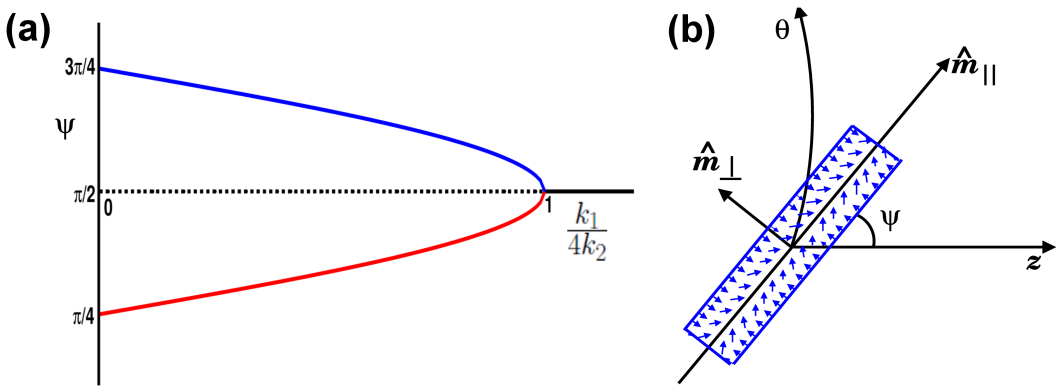

FIGURE 2.14: (a) Orientation of tilted segment ψ, schematically represented in (b), with (short) arrows showing $\mathbf{n}$ within the segment. The steady state tilt plotted as a function of $\frac{k_1}{4k_2}$ shows a continuous transition from a ring-segment ($\psi = \pm\frac{\pi}{2}$) to a tilted segment (see text) at $\frac{k_1}{4k_2} = 1$. The symmetries of a cylinder allow for 4 stable solutions, the two shown above have a net orientation of $\mathbf{n}$ along ψ, while two more have a net orientation of $\mathbf{n}$ along $-\psi$.

wall synthesis enzymes and appear to rotate around the cell wall circumferentially and sometimes along helical tacks (Fig. 2.13)[17]. Anisotropies of the cell wall synthesis can provide "easy-directions" for anchoring of the segments of MreB filaments [16]. This possibility can be included in our framework by allowing the parameters accompanying the *nonlocal* terms in (2.2), namely K_1, K_2 and ζ, to have anisotropies consistent with cylindrical symmetry. We demonstrate that including such dependence will lead to inclination of segments different from $\psi = 0$ (cable-segment) and $\psi = \frac{\pi}{2}$ (ring-segment) where ψ is the angle between segment and the long axis of the cylinder.

Consider a tilted segment at an angle ψ to the cylinder axis ($\psi = \cos^{-1}(\hat{\mathbf{m}}_{\parallel} \cdot \hat{\mathbf{z}})$, where $\hat{\mathbf{m}}_{\parallel}$ is the unit vector along the segment boundary, Fig. 2.14(b), having a uniform width $w(\psi)$ and length $l(\psi)$ such that the area $A = wl$ is fixed. For simplicity, we assume that within the tilted segment, the filament concentration $c = c_0$ is uniform. The texture within the tilted segment is shown in Fig. 2.14(b), the orientation of $\mathbf{n}$ changes by π on a length scale $w(\psi)$. The width of the tilted segment $w(\psi)$ is set by a balance of the net current $\mathbf{J} \cdot \hat{\mathbf{m}}_{\perp}$, where $\hat{\mathbf{m}}_{\perp}$ is a unit vector normal to the boundary. In the equal constants approximation, $K_1 = K_2 = K$, the "energy" (Eqn. 2.16) of this tilted segment is given by,

$$E(\psi) = K(\psi)\frac{\pi^2 A}{w(\psi)^2} - 2\zeta(\psi)c_0\frac{A}{w(\psi)} \tag{2.22}$$

and the steady state inclination of the tilted segment is obtained by setting $\frac{\partial E}{\partial \psi}\big|_A = 0$.

The Eqn. 2.22 will in general have non-trivial solution for the steady state inclination of the segment ψ. To prove this point, it suffices to look at the anisotropy of $K(\psi)$ alone. Cylindrical shape of the cell requires the parameters to be a function of $\cos 2\psi$ because of $\psi \to \pi - \psi \to \pi + \psi \to -\psi$ symmetry. Thus, K can be written as $K(\psi) = \sum_m k_m \cos(2m\psi)$. Just retaining first two modes $m = 1, 2$ shows that inclination of segment which is different from ring and cable segments is possible. Taking this form of K and miminizing Eqn. 2.22 as a function of ψ gives the solution $\psi_0 = \cos^{-1}\sqrt{\frac{1}{2}\left(1 - \frac{k_1}{4k_2}\right)}$, where $k_{1,2}$ are the coefficients of first two modes in expansion of K. The phase diagram in Fig. 2.14, shows a continuous transition from a ring-segment with $\psi = \pm\pi/2$, to a tilted segment with $\psi = \pm\cos^{-1}\sqrt{\frac{1}{2}\left(1 - \frac{k_1}{4k_2}\right)}$, as $k_1/4k_2$ is varied. Because the net polarization of these *active* tilted segments is along ψ, short segments will appear to *move* on helical tracks while longer tilted segments will appear as moving helices.

2.8 Summary and Future Directions

To summarize, we have studied in detail, the instabilities of an active fluid of polar acto-myosin filaments on a cylindrical surface. Rings, cables and nodes(asters) emerge as the generic steady state patterns as a result of this analysis. These steady state structures can be stationary or moving depending on the arrangement of polar order in them. Spontaneous formation of rings starting from a uniform density of FtsZ filaments has been seen in the experiments on reconstituted liposomes [4] where FtsZ filaments assemble into rings and sometimes short-pitched helices. We observed phase transitions in the steady state patterns upon changing cell diameter or motor driven activity. This work also studies the transitions between different steady states as new actin filaments are nucleated. The corresponding phase diagram has been obtained by comparing an "energy functional" for the three configurations viz. nodes, cable-segment and ring-segment. We predict the transition between these three configurations as the cell radius R,the contractility parameter ζ and the domain area A are changed. Transition from the nodes to rings via the growth of cables is relevant to the assembly of acto-myosin rings in Fission Yeast cells. Strong coupling between the cell wall synthesis machinery and MreB, main component of bacetrial cytoskelaton sets the

track for dynamics of MreB and thereby further cell growth. The effect of this coupling on the organization of MreB filaments is studied by incorporating additional anisotropies in the parameters of the theory.

We have predicted the spontaneous formation of rings, cables and asters of acto-myosin filaments on cylindrical surface. However an interesting question will be to ask how does the transition from one phase to another takes place. This can be answered by following the quenches numerically from one parameter regime to the other. This will also enable a closer contact to the experimental observations on Fission yeast. Having obtained rings, cables and nodes as steady state solutions on the cylindrical surface next question would be to ask what patterns one obtains when the cell has spherical shape and are they stable. As motivated in chapter 1 we would also like to understand the patterns of active polar filaments on the composite surfaces. Next chapter addresses some of these questions.

Bibliography

[1] J. Huang, Y. Huang, H. Yu, D. Subramanian, A. Padmanabhan, R. Thadani, Y. Tao, X. Tang, R.W. Solnder and M. Balasubramanian, J. Cell Biol. **199**, 831(2012).

[2] T.D. Pollard and J.Q. Wu, Nat. Rev. Mol. Cell Bio. **11**, 149 (2010).

[3] M. Mishra, Y. Huang, P. Srivastava, R. Srinivasan, M. Sevugan, R. Shlomovitz, N. Gov, M. Rao and M. Balasubramanian, J. Cell Science **125**, 3850(2012).

[4] M. Osawa, D.E. Anderson and H. P. Erickson, Science **320**, 792 (2008).

[5] M.C. Marchetti, J.F. Joanny, S. Ramaswamy, T.B. Liverpool, J.Prost, M. Rao and R.A. Simha, arXiv:1207.2929.

[6] J. Toner and Y.H. Tu, Phys. Rev. E **58**, 4828 (1998).

[7] Sarasij R.C. and M. Rao, Phys. Rev. Lett. **88**, 088101 (2002).

[8] A.E. Carlsson, A.D. Shah, D. Elking, T.S. Karpova, and J.A. Copper, Biophys. J. **82**, 2333 (2002).

[9] M. Lord and T.D. Pollard, J. Cell Biol. **167**, 315 (2004).

[10] K. Gowrishankar and M. Rao, arXiv:1201.3938 [cond-mat.soft].

[11] W.H. Press, B. P. Flannery, S. A. Teukolsky, and W. T. Vetterling, *Numerical Recipes in Fortran : The Art of Scientific Computing*, Cambridge University Press, 1999.

[12] P. Srivastava et al. under preparation.

[13] A. J. Bray, Adv. Phys. **51**, 481 (2002).

[14] A. M. Turner, V. Vitelli and D. R. Nelson, Rev. Mod. Phys. **82**, 1301 (2010).

[15] S. v.Teeffelen and Z. Gitai, The EMBO J., **30**, 4856(2011).

[16] See Table IV in, M.E. Fisher, Rev. Mod. Phys. **46**, 597 (1974).

[17] E.C. Garner et al., Science **333**, 222 (2011); J. D. Escobar et al., Science **333**, 225 (2011).

Chapter 3

Stability of the Axi-symmetric Patterns of Active Polar Filaments on Other Geometries

In the last chapter, we proposed the dynamical equations for acto-myosin filaments on a general curved surface with explicit coupling of the polar orientation to cell geometry. We studied in detail, the spontaneous formation of rings, cables and nodes of actin filaments on the surface of a cylindrical cell. In the present chapter we extend the analysis to the surfaces of spherical, saddle shaped and conical geometry. We will be interested in classifying the stable steady state patterns of acto-myosin filaments on these curved surfaces. We will largely restrict ourselves to the formation and dynamics of axi-symmetric patterns on these curved surfaces.

3.1 Patterns of Actin Filaments on Spherical Cells

Before proceeding to the analysis of steady state patterns of acto-myosin filaments on various geometries, we display the general dynamical equations for the concentration and polar orientation of the filaments proposed in the last chapter. The equation for concentration of the acto-myosin filaments followed a continuity equation with the current involving an

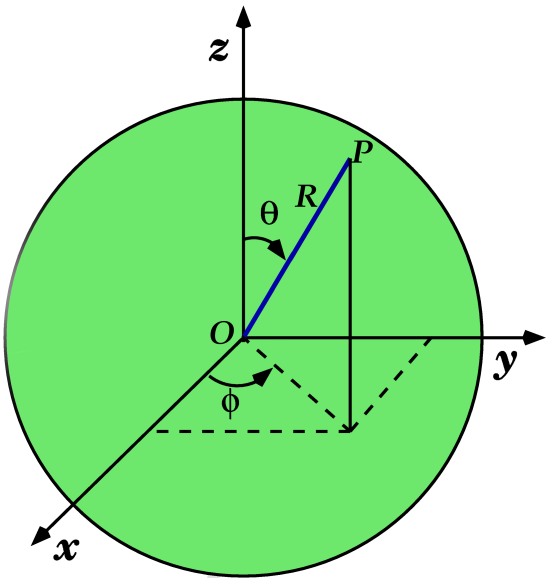

FIGURE 3.1: Spherical co-ordinate system showing polar and azimuthal angles.

explicit coupling between the curvature and polar orientation.

$$\partial_t c = -\nabla \cdot \mathbf{J}, \quad \text{where} \quad J_i = v_0 c n_i + \Lambda^{kl}_{ij} \kappa^j_k c n_l - D \nabla_i c \tag{3.1}$$

Equation for the polar orientation was proposed as

$$\frac{\partial \mathbf{n}}{\partial t} + \lambda \left(\mathbf{n} \cdot \nabla\right) \mathbf{n} = K_1 \nabla^2 \mathbf{n} + K_2 \nabla \left(\nabla \cdot \mathbf{n}\right) + \zeta \nabla c + \left(\alpha - \beta |n|^2\right) \mathbf{n} + \boldsymbol{\gamma}\, \boldsymbol{\kappa}\, \mathbf{n} \tag{3.2}$$

where ∇ is differential operator on the surface of sphere [1]. The interpretation of each of these terms is same as that in the previous chapter. Analysis in the last chapter was restricted to the cylindrical geometry. We now proceed with the similar analysis on spherical geometry. We first show that, similar to the cylindrical geometry, the curvature-orientation coupling leads to the renormalization of parameters.

Symmetry arguments discussed in the section 2.3 remain valid for the present case except that the form of curvature tensor is now changed. This increases the independent and non-zero components of Λ and γ to four, of the forms (a) Λ^{ii}_{ii} with $i = \{\theta, \phi\}$, and (b) Λ^{ij}_{ji} with $i \neq j$ and $i, j = \{\theta, \phi\}$. Spherical co-ordinate system is displayed in Fig. 3.1 illustrating the polar and azimuthal angle denoted by θ and ϕ respectively. Curvature tensor for spherical

geometry is $\kappa = \begin{pmatrix} 1/R & 0 \\ 0 & 1/R \end{pmatrix}$, where R is the cell radius. Using the symmetry arguments and the form of curvature tensor the parameter v_0 gets renormalized to $v_\theta = v_0 + \Lambda_\theta/R$ and $v_\phi = v_0 + \Lambda_\phi/R$, leading to the anisotropic active current. Similarly, the parameter α now gets modified to $\alpha_\theta = \alpha - \frac{K_1}{R^2 \sin^2\theta} + \frac{\gamma_\theta}{R}$ and $\alpha_\phi = \alpha - \frac{K_1}{R^2 \sin^2\theta} + \frac{\gamma_\phi}{R}$. Renormalization of these parameters along with the form of derivatives in the spherical geometry has been provided in Appendix A.

As a result of the anisotropy induced by the curvature-orientation coupling we obtained, rings, cables and asters as steady state patterns on the surface of a cylindrical cell. We now ask what happens to these patterns when the cellular shape is made spherical. As declared earlier in this chapter, we focus mainly on the axi-symmetric patterns of the active polar filaments on the surface of sphere. This implies that the derivatives with respect to ϕ vanish reducing the Eqns. (3.1) and (3.2) to one-dimensional equations. In the following section, we first numerically integrate one dimensional equations to find that the rings are unstable solutions and then obtain the dynamics of rings.

3.2 Rings on Sphere

3.2.1 Rings as Unstable Solutions

With the derivatives along azimuthal direction going to zero, Eqns. 3.1 and 3.2 get reduced to the following one-dimensional equations (complete equations are displayed in the Appendix A)

$$\partial_t c = -\frac{1}{R\sin\theta}\left[\frac{\partial}{\partial\theta}\left(\sin\theta\left(v_\theta c n_\theta - \frac{D}{R}\frac{\partial c}{\partial\theta}\right)\right)\right] \tag{3.3a}$$

$$\partial_t n_\theta = \frac{K_1}{R^2\sin\theta}\frac{\partial}{\partial\theta}\left(\sin\theta\frac{\partial n_\theta}{\partial\theta}\right) + \frac{\zeta}{R}\frac{\partial c}{\partial\theta} + \left(\alpha_\theta - \beta|\mathbf{n}|^2\right) n_\theta \tag{3.3b}$$

$$\partial_t n_\phi = \frac{K_1}{R^2\sin\theta}\frac{\partial}{\partial\theta}\left(\sin\theta\frac{\partial n_\phi}{\partial\theta}\right) + \frac{\zeta}{R\sin\theta}\frac{\partial c}{\partial\theta}\left(\alpha_\phi - \beta|\mathbf{n}|^2\right) n_\phi \tag{3.3c}$$

For simplicity we have taken one constant approximation i.e. $K_2 = 0$. To numerically integrate these equations, we choose the units and parameter values similar to those enlisted in the table 2.1 in previous chapter. Since we are not interested in studying the transition from disordered to polar ordered phase, we choose the same (positive) numerical value of α_θ and α_ϕ. The radius of spherical Fission yeast cells in [4] is in the range $3 - 6\mu$m. We fix the value of R at 4μm. We choose the implicit method to evolve the Eqns. (3.3a),(3.3b), (3.3c) with the boundary conditions clamped to $(n_\theta, n_\phi) = (0, 0)$ and $\partial_\theta c = 0$ at $\theta = 0$ and $\pi/2$. Starting from the uniform concentration with some randomness as initial condition, we find that the ring is quickly assembled. Profiles of the concentration and texture within the ring are shown in the Fig. 3.2 . We also find that when the ring forms at equator it is perfectly balanced and does not move (Fig. 3.2(a)). On the other hand, if the ring forms slightly away from the equator it slips towards the nearest pole (Fig. 3.2(b)).

Having obtained the rings as unstable solution on the surface of the sphere, we now follow the dynamics of ring as it moves on the frictional substrate of spherical geometry.

3.2.2 Dynamics of Acto-myosin Rings

To find the dynamics of the angular position of ring, we first note that the numerical solution described in the previous section shows clear separation between (a) a 'fast' process of the formation of ring during which the concentration and polar orientation profiles are set within the ring, and (b) a 'slow' process during which the acto-myosin ring slips towards the poles and whose dynamics we wish to follow.

Since the dynamics of ring texture is 'fast' and is slaved to the dynamics of concentration, it is sufficient to look at the dynamics of the latter. The concentration is non-zero only within the width $w << R$ of ring which is centered at $\theta_0(t)$. In the following, we implicitly assume that the ring width does not change during the ring slippage. As we will see in the next chapter, experiments performed on the spherical Fission yeast cell show that the width of the acto-myosin rings does not significantly change as the ring slips.

For a moving ring solution

$$c(\theta, t) = c(\theta - \theta_0(t)) \tag{3.4}$$

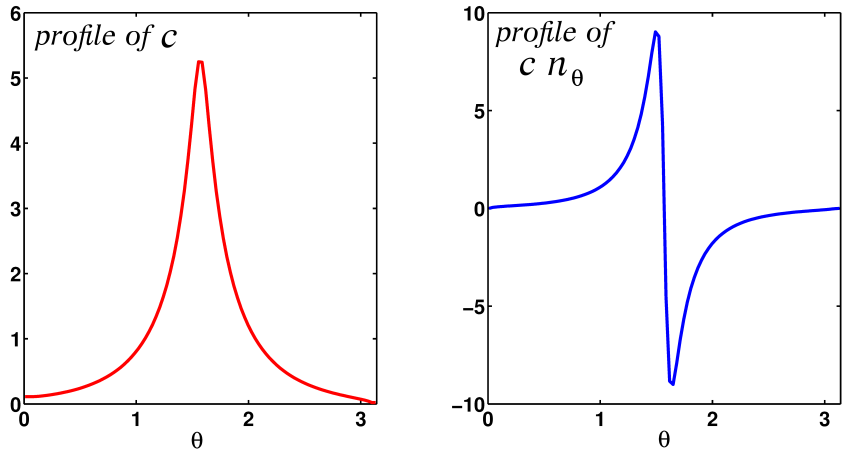

(a)

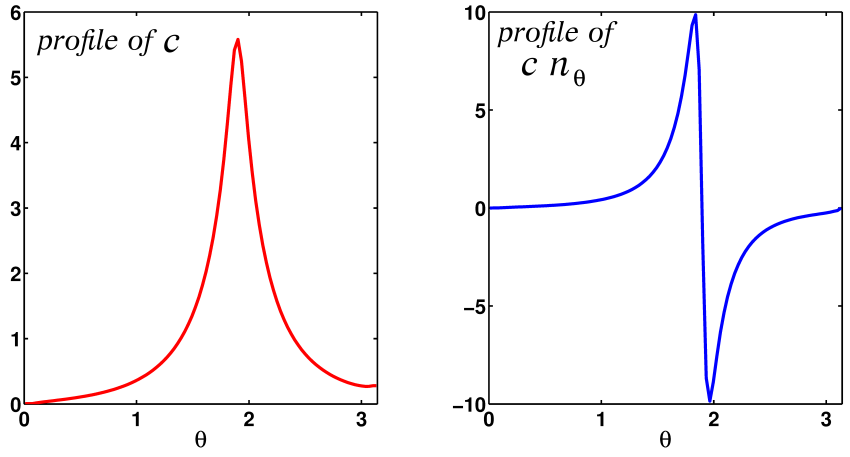

(b)

FIGURE 3.2: Profiles of c and cn_θ plotted against the polar angle θ for a ring formed at, (a) the equator and, (b) ring displaced away from the equator.

Using this in the continuity equation Eqn. 3.1 gives

$$c'\theta_0(t) = \nabla \cdot \mathbf{J}_{tot} \tag{3.5}$$

where c' is derivative of c with respect to its argument, $\theta - \theta_0(t)$. Since the ring is moving against a frictional substrate, where the friction comes from the Fission yeast cortex, we include the contributions due to the active stress generated flows in $\mathbf{J}_{tot}$ (Section 1.2.1), in addition to the active currents of Eqn. 3.1. $\mathbf{J}_{tot}$ thus can be written as $\mathbf{J}_{tot} = c\mathbf{v} + \mathbf{J}$, where $\mathbf{J}$ is given by Eqn. 3.1. $\mathbf{v}$ is the hydrodynamic velocity which, in the limit of high friction, is determined by

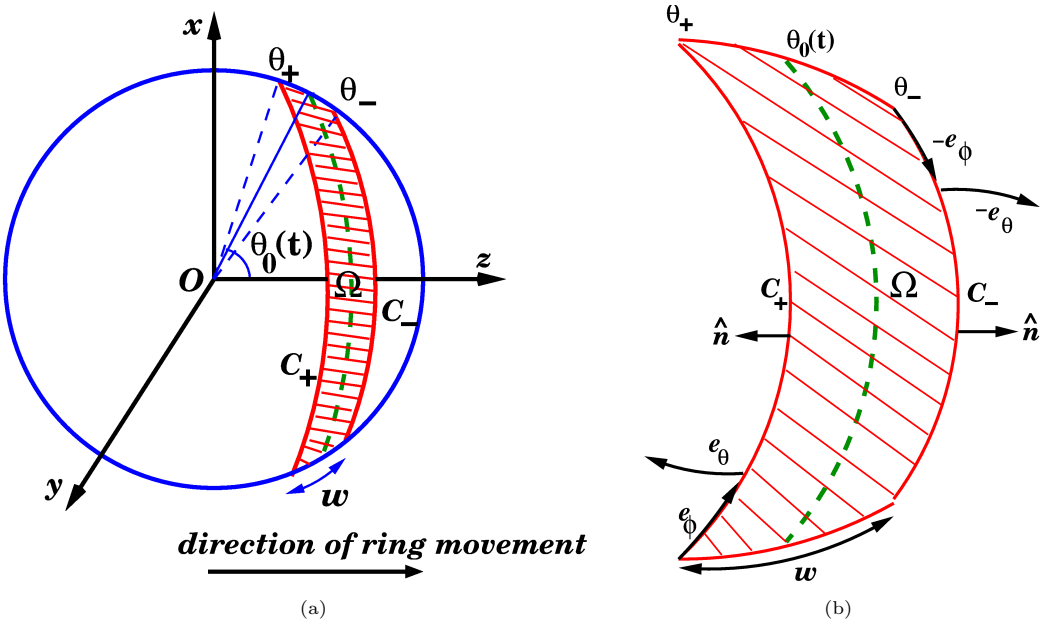

FIGURE 3.3: Geometry of the slipping ring on the spherical surface : (a) The ring represented by the shaded strip Ω and bounded by the two circles $\mathcal{C}_+$ and $\mathcal{C}_+$ at angular positions θ_+ and θ_-, respectively, has a constant width w. The centre of the ring (dashed green line) has angular coordinate $\theta_0(t)$, and slips in the direction indicated in the figure. (b) A blown-up version of the same ring, showing the unit (outward) normal and tangent vectors at $\mathcal{C}_+$ and $\mathcal{C}_+$.

$$\Gamma_{ij} v_j = \nabla_j \sigma^a_{ij} \tag{3.6}$$

σ^a_{ij} is the active stress given as $\sigma^a_{ij} = -Wcn_in_j$ and Γ_{ij} is the anisotropic effective friction offered by the Fission yeast cortex. Inverting the Eqn. 3.6 to solve for $\mathbf{v}$ we get

$$v_i = \mu_{ij} \nabla_k \sigma^a_{jk} \tag{3.7}$$

where μ_{ij} is the anisotropic mobility of the ring and is given by the inverse of friction matrix Γ_{ij}.

To obtain the dynamics of ring position, we integrate both sides of the Eqn. 3.5 across the ring whose centre is at $\theta_0(t)$ and width is w. Let us call this region of integration Ω (Fig. 3.3(a)) and the curve bounding the region $\mathcal{C} \equiv \mathcal{C}_+ \cup \mathcal{C}_-$. To evaluate these integrals, we make use of two integration formulae for vector fields on a spherical surface, which we state here without proof [1].

1. For a scalar field f
$$\int_{\Omega} \nabla f \cdot \hat{e}_i \, d\,a = \int_{\mathcal{C}} f \, \hat{e}_i \cdot \hat{n} \; d\,l \tag{3.8}$$

2. For a vector field $\vec{A}$
$$\int_{\Omega} \nabla \cdot \vec{A} \; d\,a = \int_{\mathcal{C}} \vec{A} \cdot \hat{n} \; d\,l \tag{3.9}$$

where the area element $d\,a \equiv R^2 \sin\theta d\theta d\phi$ and the line element $d\,l = R \sin\theta d\phi = r\, d\phi$ evaluated along the boundary $\mathcal{C}$. The vector $\hat{n}$ denotes unit outward normal to the boundary (Fig. 3.3(b)). Making use of the expressions given by Eqns. (3.8) and (3.9) and noting that,

$$\vec{\nabla} = \hat{e}_\theta \frac{1}{R} \frac{\partial}{\partial \theta} \tag{3.10}$$

we find the final formula for the angular velocity of the ring,

$$\dot{\theta}_0(t) = -\frac{1}{R} \frac{J_{tot}\Big|_{\mathcal{C}_+} - J_{tot}\Big|_{\mathcal{C}_-}}{N\Big|_{\mathcal{C}_+} + N\Big|_{\mathcal{C}_-}} \tag{3.11}$$

where $J_{tot}\Big|_{\mathcal{C}_\pm}$ is the magnitude of the total current evaluated at the boundaries $\mathcal{C}_\pm$. Also, $N\Big|_{\mathcal{C}_\pm}$ is the total number of filaments, at the boundaries $\mathcal{C}_\pm$. The form of the above equation is independent of the precise texture of the orientation density within the ring, *as long as it is contractile*. The current J_{tot} has contributions from both, (a) the active forces, and (b) the active currents. In the limit of high friction Eqn. 3.11 can be written as the following force balance

$$\text{Angular velocity of the ring} = \text{Mobility} \times \text{Force} \tag{3.12}$$

In case of a ring which is perfectly placed at the equator, the total currents J_{tot} on both the edges are same and balance out each other. However, when the ring is slightly displaced away from the equator, the total currents at the two edges are no more the same and there is a net force acting on the ring, resulting in the polewards sliding of the ring.

3.3 Asters on Sphere

Another plausible solution on the surface of sphere are asters. The scale of these asters is set by the ratio of Diffusion constant D and v_0 [2]. In the limit when $\frac{D}{v_0} << R$, the effect of curvature of the spherical cell will be neglible and locally the geometry will be planar. In [2],[3], Gowrishankar et al. found that the inward pointing asters were steady state solutions of the dynamical equations for concentration and polar orientation. At high contractility, these asters formed a square lattice. Now, let us decrease the radius of the spherical cell so that the curvature effects are no longer negligible. It will now be interesting to ask what is the most favored arrangement of these asters on the surface of a sphere. In the context of arrangement of N electrons on the surface of sphere interacting with each other by Coulomb repulsion, this problem is known as the Thomson problem. Answering this question in the context of asters will require the knowledge of the specific nature of interactions between the asters and is not taken up in the present work.

3.4 Mechanical Model

We now come back to the implications of Eqn. 3.12 in the context of an acto-myosin ring placed on the surface of sphere. Eqns. 3.11 and 3.12 predict that such a ring will

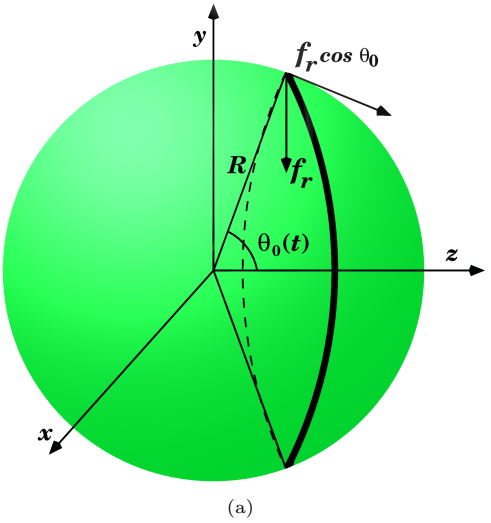

(a)

FIGURE 3.4: Direction of the contractile force density f_r due to the acto-myosin ring.

be unstable in its position and will slide towards the poles. These predictions indeed are observed in the experiments performed on spherical Fission Yeast cells which acquire their spherical shape due to removal of the rigid cell wall. Using our model based on the coupling between acto-myosin contractility and cell shape we make comparisons between the theory and experimental observations [4] in next chapter. Acto-myosin contractility is the driving force for the ring dynamics. We denote this active contractile force density by f_r and infer the features of f_r by analyzing the fluorescence images of myosin-II intensity during the ring slippage (Fig. 3.4). This discussion follows in the next chapter. Here we just state the features of the force density f_r that we use to write (and later verify) a simple mechanical model for the ring dynamics. The mean force density is (a) uniform along the ring and, (b) constant in time as the ring slips [4]. Direction of the contractile force density f_r due to the acto-myosin ring is shown in the Fig. 3.4. Noticing that the tangential component of f_r is responsbile for the ring slippage, ring dynamics can be written as

$$R\dot{\theta}_0(t) = \Lambda f_r \cos\theta_0 \tag{3.13}$$

where θ_0 is instantaneous position of the ring and Λ is mobility per unit length. This simple mechanical model can be solved to give time dependence of angular position of the ring as

$$\theta_0(t) = \frac{\pi}{2} - 2\,\mathrm{arccot}\left[e^{-\frac{t}{\tau_s}}\cot\left(\frac{\pi}{2} - \frac{\theta_0(0)}{2}\right)\right] \tag{3.14}$$

Where $\theta_0(0)$ is the initial position of the ring and $\tau_s = \frac{R}{\Lambda f_r}$ is the time scale of ring slippage. In the next chapter we compare this expression with the experimental trajectories of the acto-myosin rings on spherical Fission yeast cells.

We now extend the mechanical model of Eqn. 3.13 to the conical and saddle shaped geometries.

3.5 Other Geometries

Likewise, axi-symmetric solutions solutions on the surfaces of cones and saddles can be obtained and similar mechanical model can be proposed for the dynamics of acto-myosin

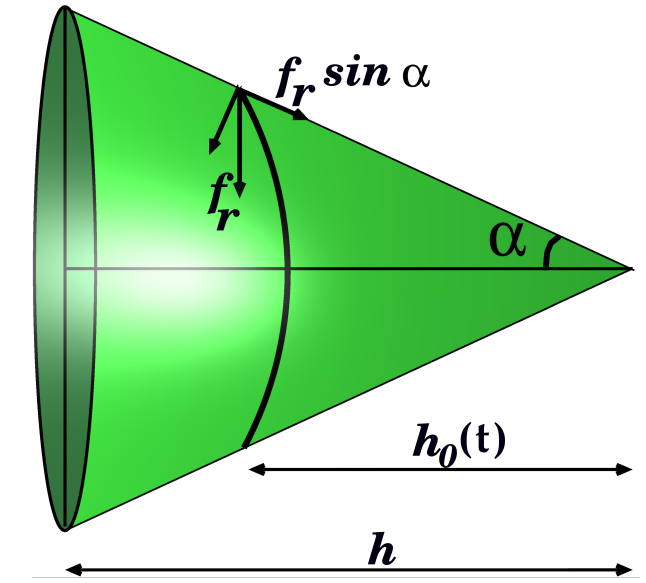

(a)

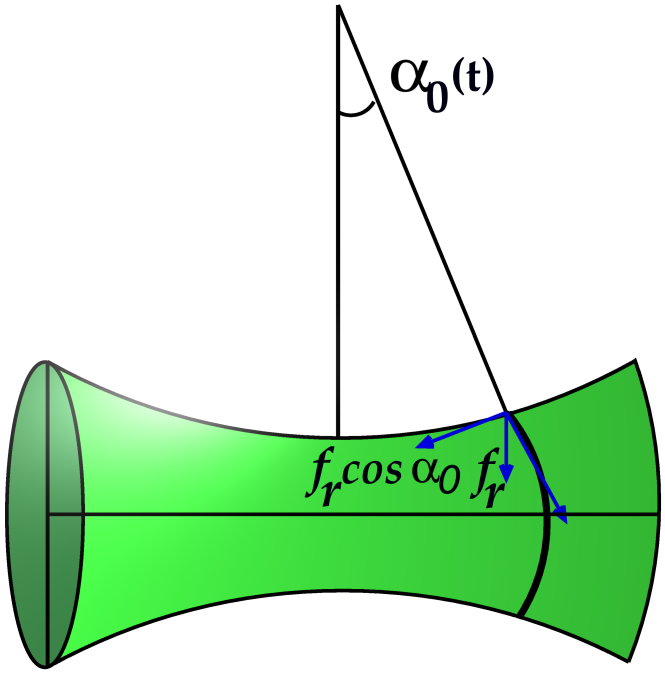

(b)

FIGURE 3.5: Contractile acto-myosin rings placed on non-deformable (a) cone and (b) saddles shaped surfaces. The direction of contractile force density f_r and the tangential component responsible for ring dynamics are shown in both.

rings in the limit of small width of the ring.

3.5.1 Cone

With the similar assumptions about the nature of contractile force density, we now write down the dynamics of a ring placed on the surface of a cone (Fig. 3.5(a)). A right angled cone is specified by its height h and the vertex angle 2α (Fig. 3.5(a)). For an acto-myosin ring on the surface of a cone the force balance (Eqn. 3.13) will read

$$\dot{h}_0(t) = -\frac{\Lambda f_r}{2} \sin 2\alpha \tag{3.15}$$

where $h_0(t)$ is the instantaneous position of the ring and α is half vertex angle of the cone. This can be easily solved to give time dependence of ring location as

$$h_0(t) = h_0(0) - \Lambda f_r t \sin 2\alpha \tag{3.16}$$

The characteristic velocity of ring sliding on the surface of a cone scales as $\sin 2\alpha$.

3.5.2 Saddle-shaped Geometry

A Saddle shaped surface is parametrized by the two radii R_α and R_β (Fig. 3.5(a)). Polar angle is denoted by α while the azimuthal angle is denoted by β. Ring like solution on the surface of a saddle will be independent of the angle β. Location of the ring is specified by the instantaneous angular position $\alpha_0(t)$ (Fig 3.5(b)). The force balance will now read

$$\dot{\alpha}_0(t) = -\frac{\Lambda f_r}{R_\alpha} \cos \alpha_0 \tag{3.17}$$

Note that the Eqn. 3.17 is very similar to the Eqn. 3.12. Characteristic time scale of the slipping will also show linear scaling with the radius R_α.

Table 3.1 summarizes the results of [3] and present work and lists the stable steady state patterns on planar, cylindrical, spherical, cone shaped and saddles-shaped geometries.

Substrate Geometry	Stable patterns
Planar	Asters (vortices are unstable)
Cylindrical	Rings, Cables, patches
Spherical	Asters(rings are unstable)
Saddle-Shaped	Rings, Asters

TABLE 3.1: Patterns of acto-myosin filaments on the substrates of various geometries

3.6 Composite Shapes : Examples and Predictions

Having obtained the stable steady state patterns of acto-myosin filaments on the surface of various geometries, we now use these results to speculate the steady state patterns on the composite surfaces. These composite surfaces can be obtained by combining the simple planar, cylindrical, spherical, cone shaped and saddle shaped geometries. We combine various shapes to obtain the composite shapes that are relevant to (a) endocytic buds and, (b) dividing cells.

3.6.1 Endocytic Buds

The process of endocytosis involves the invagination of plasma membrane. Endocytic buds can take various shapes and sizes depending on the cargo that they internalize and the specific pathway. Shape of the endocytic buds before the scission resembles the shape of a sphere joined to the flat membrane by a neck which can be of saddle or cylindrical shape

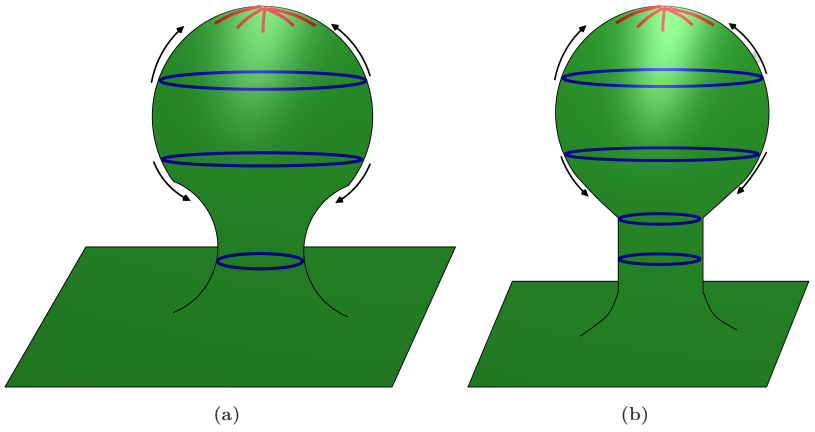

FIGURE 3.6: Shape of endocytic buds obtained as composite of simple shapes. (a) spherical cap attached to plane via saddle-shape neck, (b) spherical cap attached to plane via a cylindrical region.

(Fig. 3.6) [5]. Following the analysis and as depicted in the Fig. 3.6, a ring of acto-myosin filaments, if formed on the spherical regions will be unstable. Such ring will slip towards the poles or towards the neck (Fig. 3.6). When the ring reaches the neck, it will stabilize and it can lead to the constriction as a result of the active contractile force generated in the ring.

3.6.2 Shape of the Dividing Cells

Cytokinesis is the final stage of cell division during which the cell is separated into two daughter cells. In animal cells, during cytokinesis the formation of the acto-myosin rings happens at the equatorial region which then initiates the constriction by formation of cleavage furrow [6]. The placement of acto-myosin ring in equatorial region is guided by specific proteins (e.g. Mid1p in fission yeast cells). Contractile acto-myosin ring initiates the cleavage furrow leading to the locally saddle-shaped region. Shape of the dividing cell (Fig. 3.7(a)) can again be achieved by combining two spheres or cylinders by a cone or saddle shaped neck (Fig. 3.7(b)). If the ring forms on the tense spherical region it is unstable while when it forms in the saddle shaped region it stabilizes.

One of the predictions from this analysis indicates that the acto-myosin rings on spherical cells do not stably maintain their position and slip towards the poles and resulting in failed cytokinesis. Indeed, M. Balasubramanian et al. have observed that the Fission Yeast cells which were not of proper shape i.e. cylindrical shape, the fidelity of cytokinesis was compromised [7]. With the predictions made from the analysis presented in this chapter, these experiments were further pursued, in order to determine the role of cellular shape in stable maintenance of the acto-myosin ring. We discuss these experiments and present a comparison between the theoretical predictions of the simple mechanical model introduced in this chapter and experimental observations in the next chapter.

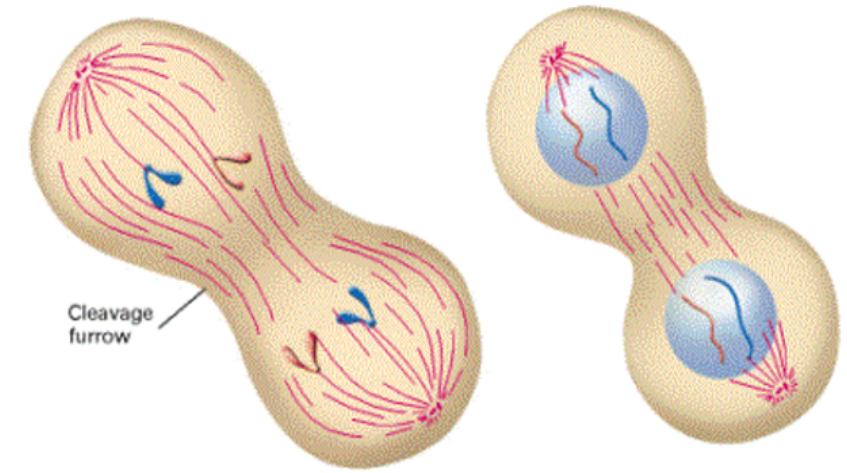

(a)

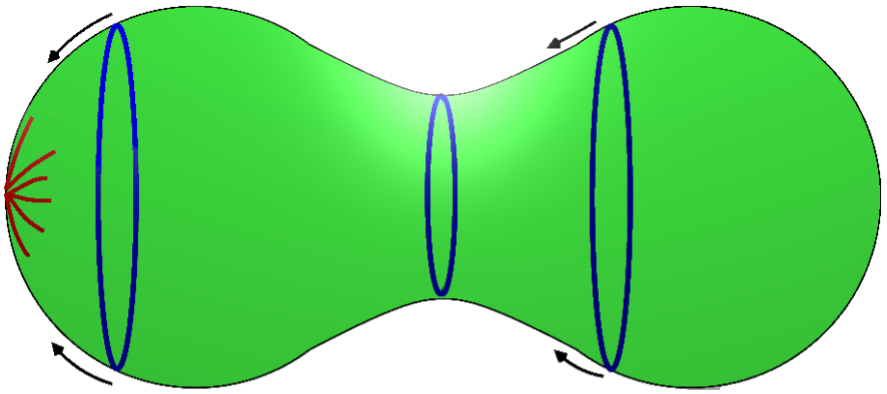

(b)

FIGURE 3.7: (a) Dividing cell in anaphase and telophase with the cleavage furrow, (b) Shape of the dividing cell as a composite of two spherical regions connected by a saddle shaped neck.

Bibliography

[1] G.B. Arfken and H.J. Weber, 'Mathematical Methods for Physicists, 4^{th} Edition', *Academic Press* ,(1995)

[2] K. Gowrishankar, 'Dynamics of Shape and Composition of an Active Composite Membrane', *Thesis Submitted to Jawaharlal Nehru University*(2009).

[3] K. Gowrishankar and M. Rao, arXiv:1201.3938 [cond-mat.soft].

[4] M. Mishra, Y. Huang, P. Srivastava, R. Srinivasan, M. Sevugan, R. Shlomovitz, N. Gov, M. Rao and M. Balasubramanian, J. Cell Science **125**, 3850(2012).

[5] R.C. Sarasij, S. Mayor and M. Rao, Biophys. J. **92**, 3140(2007).

[6] G. Salbreux, J. Prost and J.F. Joanny, Phys. Rev. Lett. **103**, 058102(2009).

[7] W. Ge, T.G. Chew, V. Wachtler, S.N.Naqvi and M.K.Balasubramanian, Mol. Biol. Cell **16**, 4124(2005).

Chapter 4

Stability of the Acto-myosin Rings in Fission Yeast Cells

In the previous chapter, we found that the cellular shape plays an important role in determining the stability of steady state patterns of the polar active filaments. Specifically we found that the acto-myosin rings formed on the spherical surfaces were unstable and slipped towards poles. This dynamics of ring slippage was also obtained from a force balance in high friction limit. These predictions on instability of rings on spherical surfaces have been confirmed by the experiments on spherical Fission Yeast cells where the stable positioning of acto-myosin rings has been observed to be affected by the cellular shape. In addition, these experiments provide important cues about the nature of the active contractile stresses responsbile for ring slippage. In this chapter we describe these experiments and present a comparison between the theoretical predictions and experimental observations.

4.1 Introduction

Cytokinesis is the final step of the cell division during which a medial ring consisting of actin filaments, myosin-II and many other proteins is assembled at the division site. This ring then constricts and leads to the separation of the two daughter cells. For a successfull cell division, accurate spatio-temporal regulation of the positioning, assembly and contraction of the acto-myosin rings is required. A signature that the cellular shape can be an important factor

in determining stable positioning of the ring was indicated in [1], where the experiments on Fission Yeast cells with non-cylindrical morphology, showed misplaced division septa. This highlighted an interplay between the cellular shape and cytokinesis. Cell geometry was also found to be crucial in determining the site and orientation of cell division axis in experiments on Sea Urchin [2]. Continuing with this, we investigate the role of cell shape and active mechanical stresses in stable positioning and contraction of the acto-myosin rings assembled on Fission Yeast cells [3].

4.2 Stability of the Acto-myosin Rings in Fission Yeast Cells

Wildtype(WT) Fission Yeast cells are cylindrical in shape with hemispherical end caps. To study the effects of the cellular shape on the stability of rings, the shape of Fission Yeast cells needs to be altered. This is achieved by removal of the cell wall using an enzyme cocktail [3]. These cells without the cell wall are stabilized osomotically using an appropriate medium (0.5 M Sorbitol). Cells without the cell wall acquire a spherical shape and are referred to as spheroplasts in the rest of this chapter. To visualize the actomyosin ring in these cells, a GFP-fused version of myosin II regulatory light chain, Rlc1p-GFP, or the Calponin-Homology-Domain of IQGAP-related protein Rng2p is expressed in the wild-type cells that were later used for the generation of spheroplasts. To correlate the dynamics of acto-myosin ring slippage with the cellcycle, mCherry-tubulin is also imaged (Fig. 4.1(a)). Spheroplasts without the cell wall were found to successfully assemble the actomyosin rings. In most cases, these actomyosin rings in spheroplasts were mechanically unstable and slid along the cortex, towards the poles while the integrity of the ring was maintained (Fig. 4.1(a)-(b)) [3]. The sliding instability occurred even when the spheroplasts were not exactly spherical (Fig. 4.1(b)-i).

Based on these observations, ring slippage on the spheroplasts can be attributed to (a) non-cylindrical cellular shape or, (b) lack of the cell wall which can also lead to the destabilization of acto-myosin ring position. To rule out the second possibility, the behaviour of actomyosin rings formed on the hemispherical end caps of cylindrical Fission Yeast cells was observed. If non-cylindrical shape were responsible for the ring instability, as opposed to the

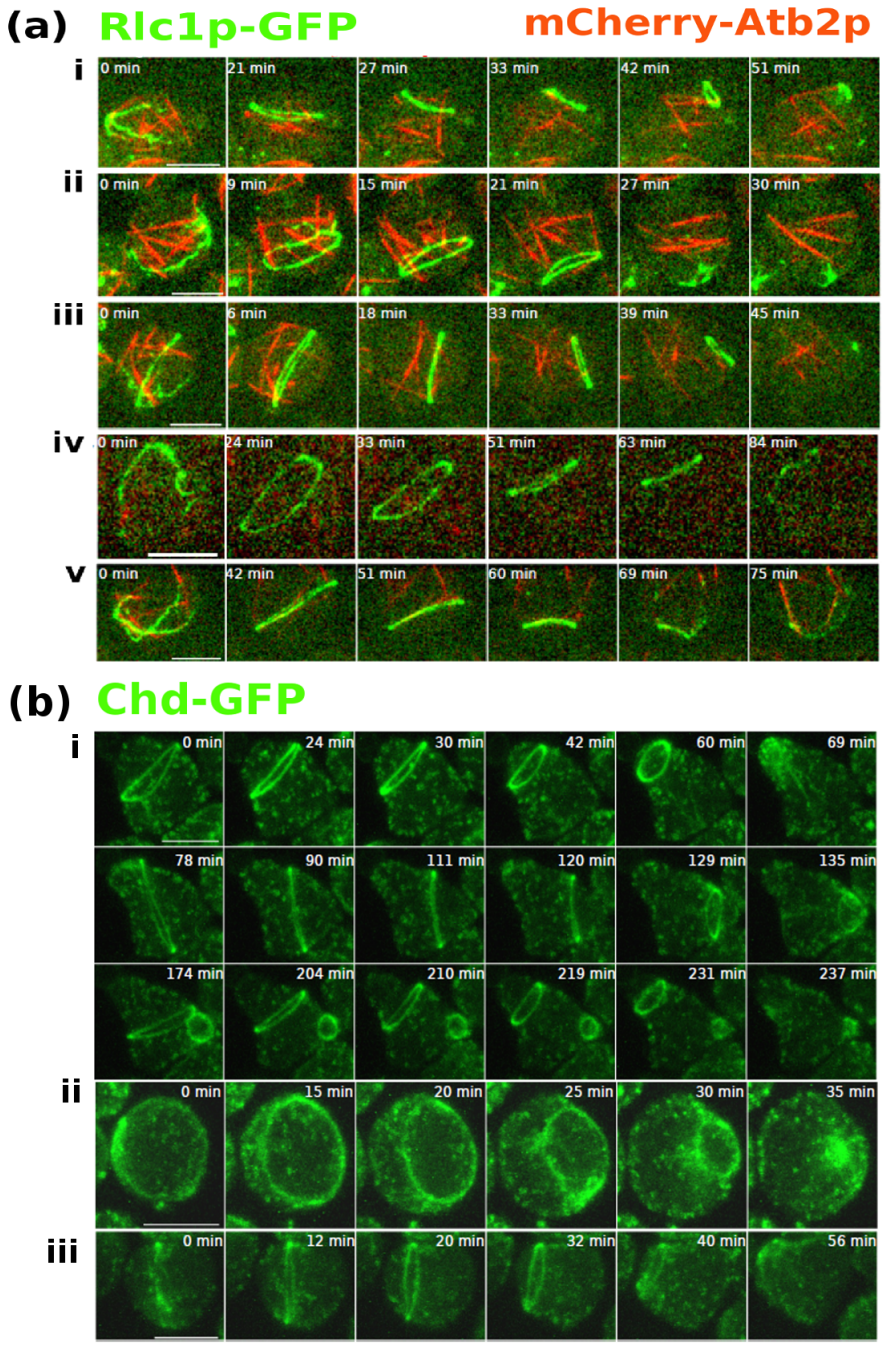

FIGURE 4.1: Acto-myosin ring slippage in spheroplasts and conical cells expressing (a) Rlc1p-GFP and mCherry-Atb2p and (b)chd1-GFP. Spheroplasts were imaged using spinning disc confocal microscopy. 39 of the 68 observed rings slipped towards the pole of the cell instead of constricting centripetally (Scale bar 5μm) [3].

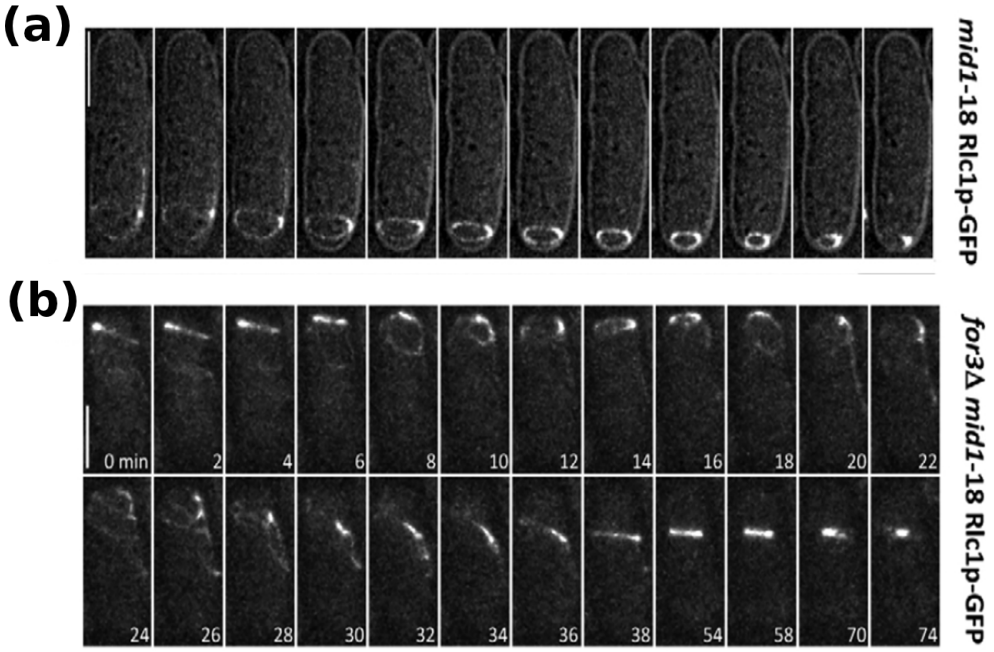

FIGURE 4.2: (a) Acto-myosin ring slippage on end caps of WT Fission Yeast cells, (b) Ring constriction when it is formed in the medial region of the cell [3].

absence of cell wall, acto-myosin rings formed at the hemispherical end caps of cylindrical cells should also exhibit the same sliding instability (Fig. 4.2). This was achieved on the cells which were defective in Mid1p protein. Mid1p protein localizes in the medial region of the Fission Yeast cells and is important for the division plane positioning. In the cells defective of the mid1p protein, acto-myosin rings, if formed at the hemispherical end caps slide towards the poles (Fig. 4.2(a)). In the instances where the rings were formed in the cylindrical region of the Fission yeast cell, normal ring constriction and septation followed (Fig. 4.2(b)).

The behaviour of actomyosin rings in the cells lacking Myo52p (a non-essential type V myosin) was also studied. Morphology of these cells shows sections of cell cortex bulging out as a sphere in medial regions. Consistent with the observations in spheroplasts and cell ends, acto-myosin rings assembled medially but due to the local spherical geometry, they were not stable in positions and slipped. As soon as these rings reached cylindrical regions they became stable and constricted [3].

These experiments on the spheroplasts, spherical mutants and WT Fission Yeast cells established that cell geometry is an important factor in determining the stability of the cortical ring [3]. The driving force for the ring contraction is identified to be the acto-myosin contractility [3], [4]. We now propose a simple mechanical model where the dynamics of ring slippage is obtained as a balance of active mechanical stresses generated by acto-myosin contractilility and the dissipation generated by the effective friction of the substrate.

4.3 The Mechanical Model

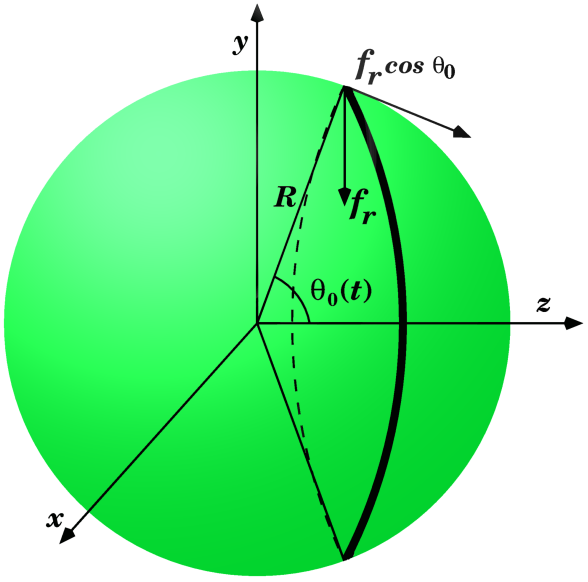

FIGURE 4.3: Contractile ring on the surface of spherical cell of radius R. $f_r \cos\theta_0$ is the tangential component of contractile force per unit length f_r, resulting in the poleward sliding of the ring. $\theta_0(t)$ is the instantaneous position of the ring and can take values from $\frac{\pi}{2}$ to 0 corresponding to ring placed at the equator and the poles respectively.

Fig.4.3 schematically shows an acto-myosin ring placed on the surface of a sphere. Active contractile stress due to acto-myosin filaments in the ring has normal as well as tangential components. Normal components of the stress are balanced by elastic stress of the osmotically tense membrane of spheroplasts while tangential components of the active mechanical stress are balanced by dissipative stresses. In order to be able to describe the ring slippage using only the angular position of the ring we need to ascertain that the force density is uniform along the length of the ring. This we test by analyzing the fluorescence intensity

I of myosin II along the circumference of the ring. The intensity I is computed by first integrating the myosin II intensity over the ring width and then binning over 5 pixels along the circumference of the ring. I is then normalized by its maximum value along the ring for each individual cell. The resulting plots are shown in the Fig. 4.4 (a) for four spheroplast cells. Uniformity of the myosin intensity along the ring allows us to describe ring using its instantaneous angular position. This uniformity has intersting implications about the assembly of acto-myosin to which we return in later part of this chapter. In addition, the mean intensity of myosin is also constant in time. This is seen in the myosin II fluorescence images where we plot mean intensity in time Fig. 4.4(b)(blue lines) and implies that mean force per unit length due to acto-myosin contractility is constant in time. We also plot mean ring width calculated as the full width at half maximum in time. This also remains roughly constant in time. This implies that the acto-myosin component of the ring turns over as the ring slides. A later experiment confirmed this and put the turnover time scale to $\sim$ 16s for these experiments (see discussion).

4.3.1 Predictions and Comparison with the Experiments

Having made these quantifications about myosin II intensity, we can write down the force balance as, $\gamma v_\theta = f_r \cos\theta_0$. $v_\theta = R\dot{\theta}_0$, where $\theta_0(t)$ is instantaneous position of the ring, R is the radius of cell and γ is the effective friction. This equation gives a characteristic time scale $\tau_s = \frac{R}{\Lambda f_r}$ for sliding, where Λ is mobility (inverse friction) per unit length. This can be solved to give time dependence of the angular position of the ring

$$\theta_0(t) = \frac{\pi}{2} - 2\,\mathrm{arccot}\left[e^{-\frac{t}{\tau_s}}\cot\left(\frac{\pi}{2} - \frac{\theta_0(0)}{2}\right)\right] \tag{4.1}$$

This equation immediately implies that the ring dynamics depends only on the instantaneous position of the ring. This fact is verified by making relative shifts of experimentally obtained data of angular position versus time for different cells along time axis. Angular position of the ring versus time curves for 15 cells without this time shift are shown in Fig. 4.6 (a) and (c) for cell ends and spheroplasts respectively. After time shifts these curves collapse on a master curves when plotted against scaled time $\frac{t}{\tau_s}$ shown in Fig. 4.6 (b) and (d) for cell ends and spheroplasts respectively. Fig. 4.6(e) and (g) show comparison between

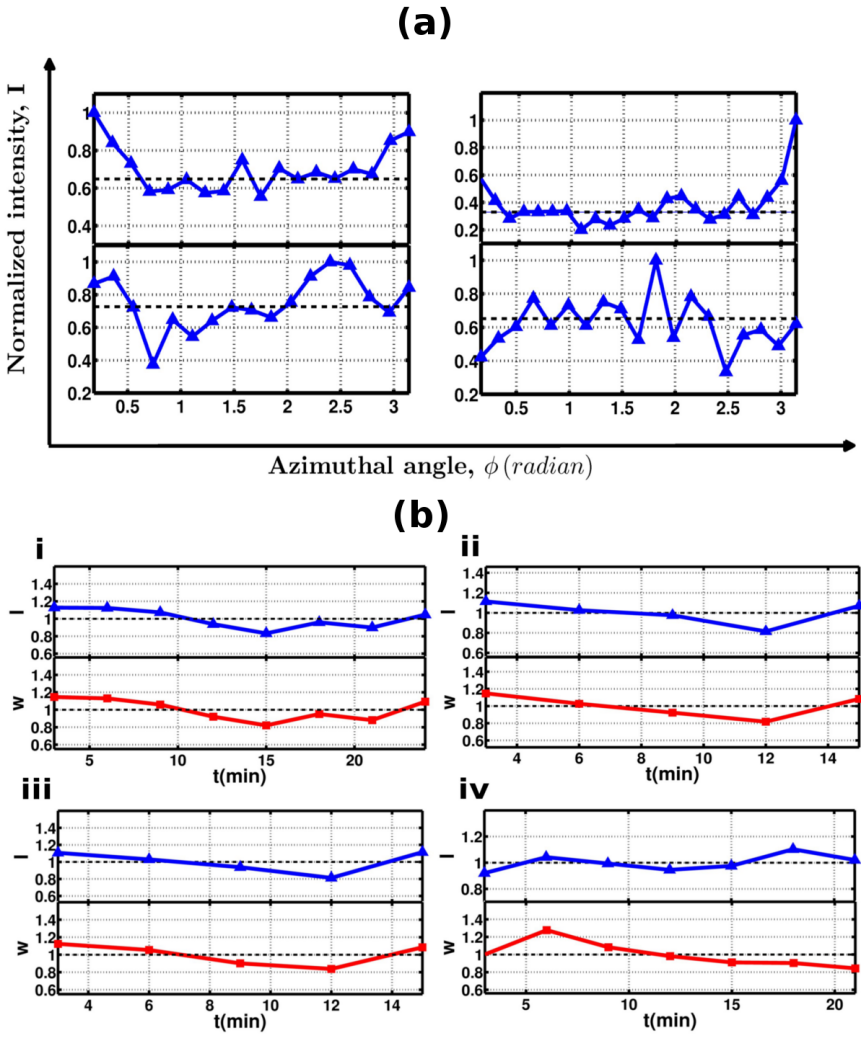

FIGURE 4.4: (a) Plot of Myosin II fluorescence intensity along the circumference of the ring parametrized by the azimuthal angle (in radians) for 4 spheroplast cells. The intensity I is computed as is described in the text. These images show that the Myosin II fluorescence intensity is uniform along the ring. The higher intensity at the two ends is a result of projection effects. (b) (i)-(iv) Myosin II intensity (I) averaged over the ring circumference (blue) and the average ring width w (red) as a function of time (min) for 4 spheroplast cells. The time series is plotted by normalizing to its mean (represented by the horizontal black lines). These images show that the Myosin II fluorescence intensity I per unit length of the ring and the ring width w are roughly constant in time.

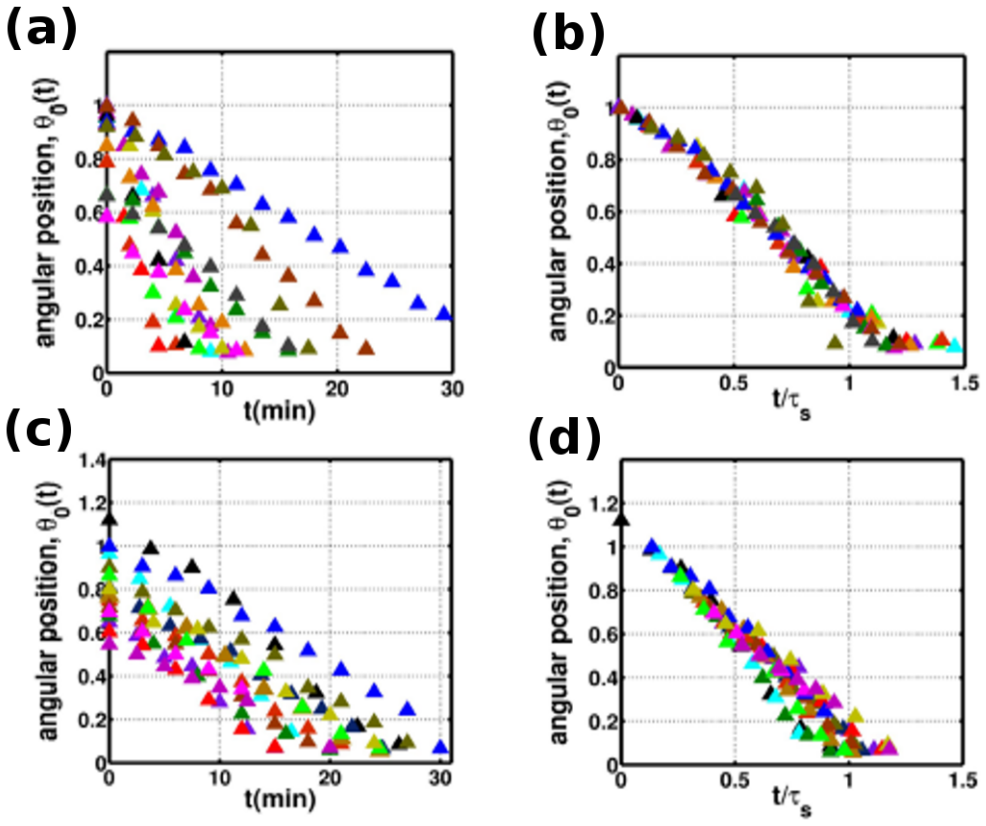

FIGURE 4.5: (a) and (c) show angular positions (in radians) of the ring versus time (in minutes) for cell ends and spheroplasts (for 15 events each), respectively, obtained from the fluorescence images. We use the Eqn. 4.1 to reorganize the data in (a) and (c). We make relative shifts along the time axis so as to obtain a smooth profile of θ_0 versus t. Each data set is fitted to the expression for the angular position versus time (Eqn. 4.1) using τ_s as parameter. This value of τ_s is then used to replot the data with the scaled time $\frac{t}{\tau_s}$, resulting into a master curve shown in (b) and (d) for cell ends and spheroplasts respectively.

trajectories obtained from the experiments (data points) and the analytic expression 4.1 using τ_s as parameter. The distribution of $\Lambda f_r = \frac{R}{\tau_s}$ has been plotted in the insets of Fig. 4.6(a)-(c), which is peaked at 0.12μm/min and 0.17μm/min for spheroplasts and cell ends. The characteristic velocity Λf_r is thus independent of the cell size. Finally, the characteristic time for the ring slippage scales linearly with the cell size. This is also verified from the experimental data. We plot the time taken to traverse a fixed angular distance on the surface of spheroplasts with the the radii of spheroplasts. The slippage time T shows linear scaling with the cell radius R reinforcing the validity of assumptions of this simplified model.

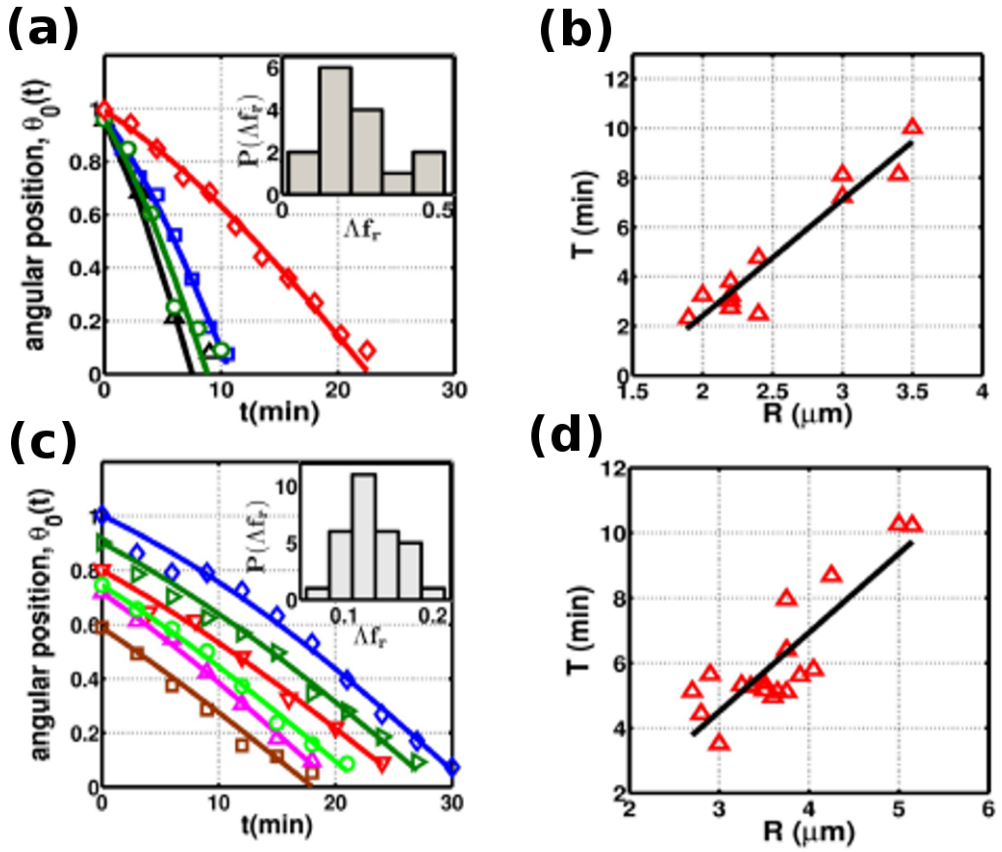

FIGURE 4.6: Angular position versus time plots are shown for (a) cell ends and (c) spheroplasts from the experiments (data points) and from the theory (Eqn. 4.1) using τ_s as parameter. Distribution of the characteristic velocity $\Lambda f_r = R\tau_s$ is shown in insets for both (a) cell-ends and (c) spheroplasts. The narrowly peaked distribution implies that the velocity is independent of cell size and the time scale of slipping scales linearly with R. (b) and (d) show linear scaling of time taken to traverse a fixed angular distance on the surface of cell with the cell size.

4.4 Discussions and Future Directions

To summarize, we have shown that the cellular shape plays an important role in determining the stability of acto-myosin rings. If these rings are formed on cylindrical regions of the WT Fission Yeast cells then they are stable in position and constrict leading to successfull cytokinesis. On the other hand, if they are formed on spherical or conical shaped cells (spheroplasts/spherical mutants/end-caps of WT Fission Yeast cells), they do not stably maintain their position and slide polewards. This sliding instability of actomyosin rings on

locally spherical and conical geometries can be quantitatively understood using a mechanical model based on contractile forces exerted by the ring at the cell surface. We verify several predictions from this model, in particular the scaling of the ring slippage time with cell radius. We now highlight the implications of good agreement between our model and experimental observations.

1. **Uniformity of the contractile force density along the ring** :- A key assumption of our model is that the contractile force per unit length is uniform along the ring verified by the fluorescence images of myosin II. A uniform force density is required for the integrity of the ring since if it were not, different parts of the ring would have slipped with different angular velocities, leading to a disruption of the ring. Since the ring assembly proceeds by local recruitment of F-actin and Myo-II an interesting question to ask is, how this uniformity is established and maintained. One possibility could be that there are molecular checkpoints which trigger the constriction only after the uniformity of force density is established. Another explanation could be that inhomogeneities in myosin recruitment lead to inhomogeneities in active contractile forces along the ring circumference, driving circumferential currents. These currents then quickly re-establish the homogeneity of the ring.

2. **Constancy of the mean force density in time** :- Analysis of the Myo-II fluorescence images also shows that the mean intensity per unit length is constant in time during ring sliding. The fact that force per unit length is constant in time also reflects in the linear scaling of slippage time with cell radius. Good agreement between the simple mechanical model and the experiments indicates that the turnover kinetics of myosin II is not the rate limiting for ring shrinkage. This can only happen if the filament and myosin turnover rate is high. To confirm if this is the case, Fluorescence Recovery After Photobleaching (FRAP) experiments to estimate the turnover rate of myosin II in slipping rings spheroplasts were carried out. Myo-II was found to be highly dynamic with a $t^{1/2}$ of 16 ± 3s and is much smaller than the ring slippage time. Our analysis shows that the Myo-II concentration levels remain constant throughout the constriction while a previous work has shown that myosin II concentration increases during constriction in cells [5]. The difference between the two may be rooted in the fact that in our case

cytokinesis is decoupled with the septation. It will be an interesting question to ask if this is the case. If the difference between the two is significant, it will imply that the septation itself affects the recruitment and turnover of the components of acto-myosin ring.

The role of cellular shape is established to be crucial factor in determining the stability of acto-myosin rings. Experiments with the spheroplasts, cylindrical yeast cells and physical description of the actomyosin dynamics on spherical geometries imply that the cytokinetic ring would inherently be unstable in a spherical region and the cylindrical geometry of the wild type cell facilitates maintenance of the actomyosin ring position for maximal fidelity of cytokinesis.

In previous and present chapter we have seen that the cellular geometry has important role in patterning the active polar fluid as well as stability of the patterns. Thus far we encountered tense membranes so that the cellular shape was non-deformable. As mentioned in Chapter 1, when the plasma membrane is deformable, active stresses and currents generated in the cortical actin can give rise to interesting shape instablities of the plasma membrane as well as patterning of acto-myosin in cortical actin. In the next chapter we study the consequences of this interplay between the cellular shape and acto-myosin contractility.

Bibliography

[1] W. Ge, T.G. Chew, V. Wachtler, S.N.Naqvi and M.K.Balasubramanian, Mol. Biol. Cell **16**, 4124(2005).

[2] N. Minc, D. Burgess and F. Chang, Cell **144**, 414(2011).

[3] M. Mishra, Y. Huang, P. Srivastava, R. Srinivasan, M. Sevugan, R. Shlomovitz, N. Gov, M. Rao and M. Balasubramanian, J. Cell Science **125**, 3850(2012).

[4] T.D. Pollard and J.Q. Wu, Nat. Rev. Mol. Cell Bio. **11**, 149 (2010).

[5] J.Q. Wu and T. D. Pollard, Science **310**, 310(2005).

Chapter 5

Active Deformation of an Active Composite Membrane

Cells regulate their shape dynamically in order to engage with the extracellular environment and to bring about various cellular processes e.g. cell locomotion, cell division. Cell shape changes invariably involve an intimate coupling to the deformation of acto-myosin meshwork just beneath the plasma membrane. A number of experiments, as we discuss in this chapter, provide evidence for the interplay between the dynamic active cortical actin and cell shape deformation in a variety of cell types which can either be stationary, spreading or motile. In this chapter we study the interplay between cortical actin and the plasma membrane. Our aim is to understand the consequences of such interplay on the emergence of self organized actin and membrane waves,ruffles and budding. Apart from engaging in the actin polymerization that leads to the steady propulsion, actin nucleation at the PM also leads to formation of cortical actin meshwork which provides both elastic stresses and frictional resistance to the flow and comprises of a rigid, active, elastic meshwork and dynamic, active filaments.

We start by quoting some examples of the acto-myosin and membrane waves and ruffles observed in experiments. We then briefly review the existing theoretical models that have been proposed to understand the emergence of these dynamic patterns.

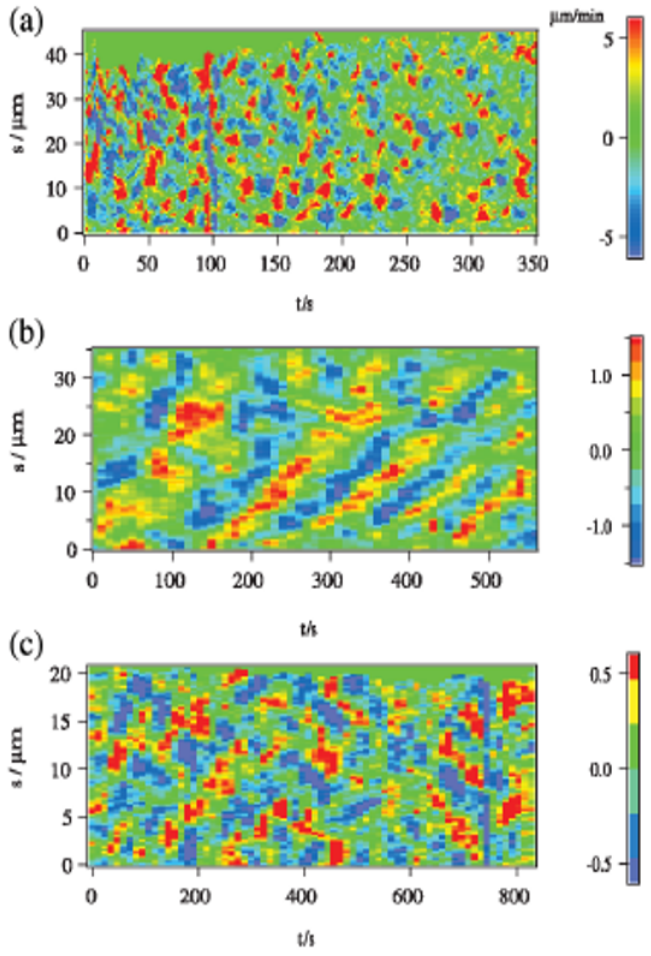

FIGURE 5.1: Maps of the normal velocity of the membrane for (a) mouse embryonic fibroblasts, (b) fly wing disk cells andc (c) mouse T-cells. y-axis corresponds to the arclength along the leading edge and x-axis is the time. The diagonal patterns in the maps indicate lateral membrane waves (Courtesy: [1]).

5.1 Membrane Waves and Ruffles in Spreading and Motile cells

Actin and membrane waves as well as ruffles are generically observed patterns at the leading edge of motile and spreading cells. Sheetz et al. observed lateral waves of protrusion and retraction on the cell membrane in Mouse Embryonic Fibroblasts, T-cells and wing disk cells from fruit flies using TIRF microscopy (Fig. 5.1) [1]. Determination of the velocity of these waves and the spatio-temporal correlations of the protrusion and retraction indicated that the contractility of acto-myosin gel is the underlying mechanism for generation of wave like behaviour. Another study by Mogilner et al. shows that the self organized waves of acto-myosin coupled with the adhesive properties of substrate play crucial role in determining the shape as well as in regulating the migration pattern of the motile fish keratocyte

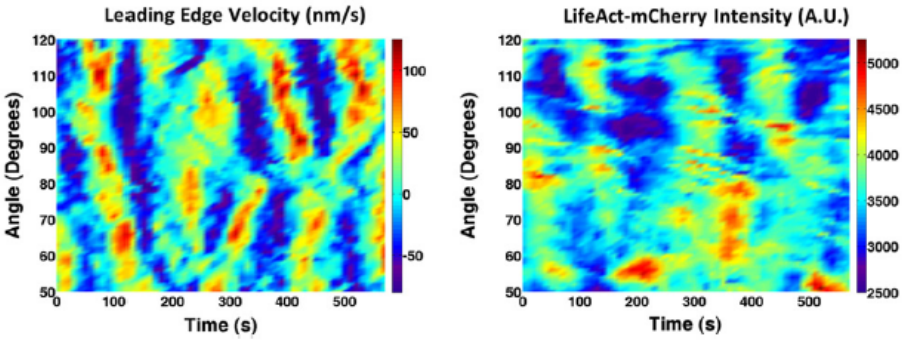

FIGURE 5.2: Left panel : Normal velocity map of the leading edge for XTC cell spreading on a substrate (Courtesy : [6]). Right panel : fluorescence intensity of Life-act indicating the dynamics of concentration of F-actin at the leading edge (Courtesy : [6]).

cells [2]. A large number of similar experimental studies have provided evidence for the strong coupling between the dynamics of actin at the leading edge and the shape dynamics of plasma membrane [2],[3],[4],[5].

Cells spreading on a substrate also exhbited similar actin and membrane waves e.g. XTC cells spreading on a substrate (poly-L-lysine) [6]. In these cells, the changes in the F-actin concentration were simultaneously imaged which correlated with the normal velocity patterns of the plasma membrane at the leading edge (Fig. 5.2). Tavelling actin waves generated due to the acto-myosin contracility induced by Myosin-II have also been observed in the reconstitued actin structures [7]. A recent article by Mogilner et al. gives an overview of experiments as well as the theoretical models on actin travelling waves in motile, spreading and stationary cells [5].

5.2 Existing Theoretical models

Several models have been proposed to understand the formation of acto-myosin and membrane waves. These models broadly fall into the categories of (a) curvature based models and, (b) reaction-diffusion based models. We now briefly discuss these models highlighting the mechanisms in each model that give rise to waves.

5.2.1 Curvature-based Models

To explain the membrane waves generated due to actin and myosin, Gov et al. proposed the curvature based models. These models utilize the curvature sensing properties of the proteins regulating the actin dynamics at the plasma membrane (e.g. actin nucletors or actin polymerizing proteins) and the membrane proteins [8],[9]. The mechanism that gives rise to the formation of waves is described as follows. Curvature sensing membrane proteins activate actin polymerization to which myosin motors attach producing a contractile normal force. This creates a local depression in the membrane leading to the seggregation of activators away from the region of the dip. This is followed by the myosin motors resulting into the propagating waves [8]. Similarly, in [9], the density fluctuations and thermal diffusion of the curved activators of actin polymerization coupled with the the dynamics of membrane shape lead to waves, while the activators themselves get activated in response to an extarnal stimulus. Wavelike response in these models crucially depends on the sign of spontaneous curvature preferred or induced by the activator proteins.

5.2.2 Reaction-Diffusion based Models

In a variety of systems, autocatalytic reaction-diffusion based mechanism has been used to explain the dynamics of membrane at the leading edge. Common ingredients in these models are the autocatlytic activators of actin polymerization at the plasma membrane. These activators lead to polymerization of actin at the plasma membrane. These activators are in turn inhibited by the F-actin thus leading to waves [6]. Likewise, in [10] the system of actin nucleators interacting with the F-actin also exhibits travelling wave solutions. A relevant example for this mechanism is the dynamics of Hem-1 and F-actin in neurtophils. Hem-1 is a component of SCAR/Wave complex that acts as actin regulatory proteins near the plasma membrane. Studies in [11] show that the actin polymerization is stimulated by this complex but at high concentration of F-actin this complex is removed from the membrane. Activation of the actin assembly combined with the delayed inhibition by F-actin constitutes an excitable system which exhibits generation of actin-waves [6].

To understand the spontaneous formation of actin and membrane waves as well as membrane instabilities, we now propose a coarse grained model for the coupled dynamics of plasma membrane shape and the cortical actin for spreading and motile cells. As has been discussed in the previous chapters, form of the dynamical equations are determined by the generic symmetry arguments.

5.3 Theoretical Framework : Coupled dynamics of Plasma Membrane and Cortical Actin

Actin nucleators, such as Arp2/3, polymerize actin at the leading edge and result in actin polymerization based steady cell propulsion. In addition to this, actin nucleation at the PM also leads to the formation of cortical actin meshwork which comprises of a rigid, active, elastic meshwork and dynamic, active filaments. As stated in the Chapter 1, at time scales longer than the binding/unbinding time scales of the crosslinkers, cortical actin behaves effectively as an active fluid.

At the leading edge of motile and spreading cells two main cellular structures containing actin are filopodia and lamellipodia (Fig. 5.3). These two structures are predominantly nucleated by ' formin' and 'Arp2/3' respectively. Arp2/3 nucleates a branched structure of filaments where new filaments grow at a preferred angle from the existing filaments. *formin*'

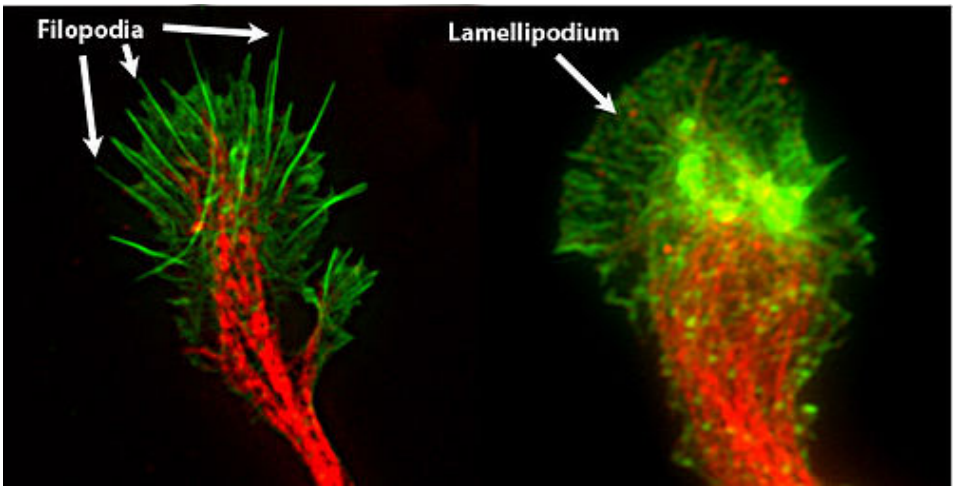

FIGURE 5.3: Fluorescently labelled growth cones showing (a)filopodial, (b) lamellipodial structure at the leading edge (Courtesy: http://en.wikipedia.org/wiki/Growthcone).

based nucleation leads to the elongated structure of actin filaments. We call the filaments that exert normal forces to the plasma membrane as vertical filaments. While the filaments that produce '*in-plane*' active stresses are termed horizontal filaments. Fig. 5.4(a) schematically depicts the two kind of filaments motivated by the EM pictures of the cortical actin shown in Fig. 5.4(b).

We denote the two dimensional concentrations of the horizontal and vertical actin by $c(\mathbf{r}, t)$ and $\rho(\mathbf{r}, t)$ respectively (referred as 'H-actin' and 'V-actin' hereafter). Steady state of (de)polymerization of the former leads to a constant total number of horizontal actin filaments while steady state of (de)polymerization of the vertical actin filaments pushing against the membrane leads to steady state cell propulsion [9]. We describe the shape of PM in Monge gauge which will be the appropriate description for the flat lamellipodium. Membrane shape is described by the height field $h(\mathbf{r}, t)$ with the local normal $\mathbf{N} = (-\nabla h, 1)/\sqrt{1 + (\nabla h)^2}$, where ∇ is the two-dimensional derivative. The cortical actin is described using $\mathbf{P} = (\mathbf{p}, p_z)$, where $\mathbf{p}$ is the projection of $\mathbf{P}$ on local tangent plane, defined as $p_i = (\delta_{ij} - N_i N_j) P_j$.

There are two ways to derive the dynamical equations. Starting from an effective free energy functional the equations of motion can be derived from a detailed Poisson bracket formalism

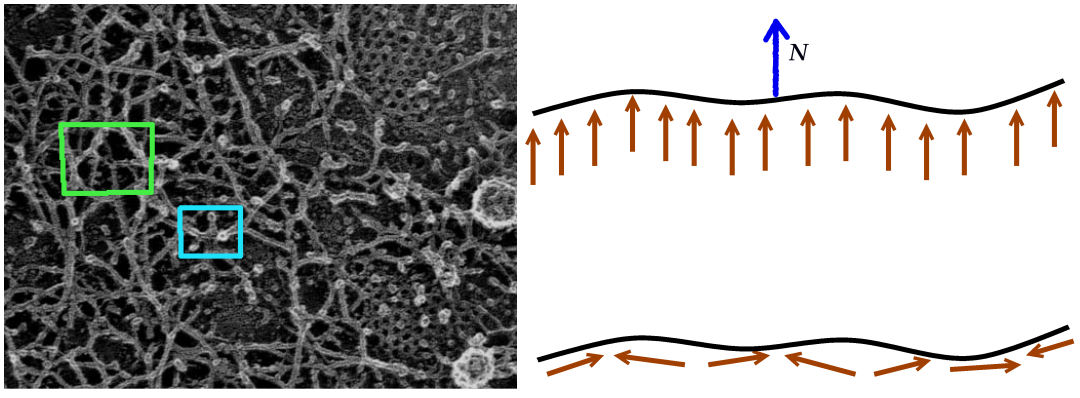

(a) (b)

FIGURE 5.4: (a) Cryo-electorn micrograph image of the cortex in Normal Rat Kidney cells showing a static crosslinked meshwork showing actin filaments with the orientations normal (blue rectangle) and horizontal (green rectangle), (Courtesy : Morone et al, http://www.nanobio.frontier.kyoto-u.ac.jp/lab/slides/4/e.html), (b) Decomposition of the cortical actin stresses at the plasma membrane in tangential and normal components.

for a passive permeable membrane coupled to an active orientable fluid in three dimensions. These equations can then be averaged along the z direction to obtain effective equations for the dynamical variables. This procedure is carried out in detail in [12]. Another approach consists of proposing the dynamical equations for the slow variables using general symmetry based arguments. The final form of the equations obtained using both these methods is same. It is the later approach that we adopt in this chapter.

5.3.1 Symmetries and the Dynamical Equations

The dynamical equations for a membrane subjected to the active stresses and currents due to both, H-actin and V-actin are constructed by appealing to the symmetry arguments. We list the symmetry arguments that we use to construct the dynamical equations and which give rise to new couplings between the cortical actin and the membrane shape.

1. The pressence of actin nucleators on the inner side of the membrane gives rise to the formation of cortical actin leading to a well defined '*inside*' and '*outside*' of the membrane. The nucleation of V-actin at the leading edge results in pushing the membrane '*outward*' shown by the direction $\vec{V}$ in the Fig. 5.5(a) [9]. This implies that the $h \to -h$ symmetry is broken for the motile or spreading cells.

2. The dynamical equations should be invariant under the simultaneous rotations of the local membrane normal $\mathbf{N}$ and the three-dimensional polar orientation vector $\mathbf{P}$ (Fig. 5.5(b)).

Taking these symmetry considerations into account, we now propose the coupled dynamical equations for the cortical actin described by the concentration fields $c(\mathbf{r}, t)$, $\rho(\mathbf{r}, t)$ and the polar orientation vector $\mathbf{P}$, and the membrane height $h(\mathbf{r}, t)$.

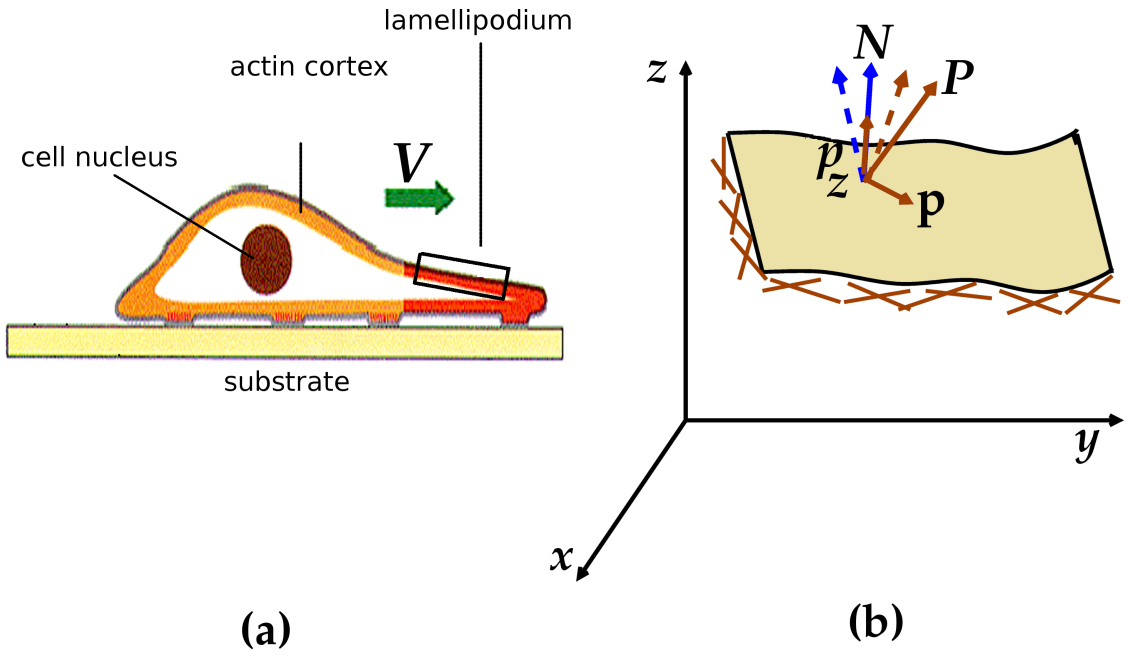

FIGURE 5.5: (a) Schematic of a motile cell. (b) Schematic diagram of a blown up part of the leading edge of the membrane, depicting the symmetry of the system under simultaneous rotation of membrane normal $\mathbf{N}$ and the vector $\mathbf{P} = (\mathbf{p}, p_z)$.

5.3.1.1 Dynamics of Filament Concentration

The concentration of horizontal actin filaments follows a conservation law on the time scales smaller than the actin turnover time scales.

$$\partial_t c = -\nabla \cdot [v_0 c\mathbf{p} + \mu_1 c \nabla h - D\nabla c] \tag{5.1}$$

The current for concentration consists of an active advection by the in-plane polar order $\mathbf{p}$, a slope dependent current and a contribution form diffusive current with diffusion constant D. As we will see later, the slope dependent current is a coupling allowed by symmetry.

The dynamics of concentration of vertical actin filaments to the lowest orders is given by

$$\partial_t \rho = -k_{off}\rho + k_{on} - \nabla \cdot \left[l_1 \rho^2 \nabla h + l_2 \rho \mathbf{p} + l_3 \nabla(c\mathbf{p} \cdot \nabla h) - l_3 \nabla(\nabla^2 h) - D_\rho \nabla \rho\right] \tag{5.2}$$

where $k_{off/on}$are the rates of (un)binding of nucleators of vertical actin and $l_{1,2,3}$ are phenomenological coupling parameters.

5.3.1.2 Dynamics of Filament Orientation

The three-dimensional polar orientation vector $\mathbf{P}$ can be resolved in the in-plane component $\mathbf{p}$ and a normal component p_z. As we have mentioned earlier, the normal component is associated with the V-actin which pushes against the membrane. We assume that this component relaxes fast in comparison to the in-plane vector $\mathbf{p}$. This can be physically achieved by having an anisotropic friction coefficient at the plasma membrane of the form $\Gamma_m = \delta_{ij} + \gamma_m N_i N_j$. For large and positive values of γ_m, p_z relaxes fast. The dynamics of in-plane polar order $\mathbf{p}$ is given as

$$\partial_t \mathbf{p} = -\Lambda_1 \mathbf{p} \cdot \nabla \mathbf{p} + \mu_2 \rho c \nabla h + K_1 \nabla^2 \mathbf{p} + K_2 \nabla(\nabla \cdot \mathbf{p}) + \zeta \nabla c + (A - B|\mathbf{p}|^2)\mathbf{p} \tag{5.3}$$

Eqn. 5.3 has contributions from a) non-linear self advection, b) symmetry allowed coupling to height field via μ_2 which reorients $\mathbf{p}$ along ∇h, c) active torques resulting in relative alignment of filaments, c) anchoring of $\mathbf{p}$ along concentration gradients due to contractile activity and d) local non-linearity leading to a fixed non-zero magnitude of $\mathbf{p}$ beyond a threshold mean density c^* of actin filaments.

5.3.1.3 Dynamics of Membrane Shape

Membrane shape in the Monge Gauge is described by the height $h(\mathbf{r}, \mathbf{t})$ over a reference plane (Fig. 5.5(b)). The dynamics of height field is given by

$$\begin{aligned} \partial_t h &= -\mu_3 \mathbf{p} \cdot \nabla h - \Lambda_2 \nabla \cdot (\rho c \mathbf{p}) + \Lambda_3 \nabla c \cdot \nabla h + \Sigma \nabla^2 h - \kappa \nabla^4 h \\ &\quad -\kappa_1(\rho) \nabla^2 c - \kappa_2 \nabla^2 \rho + a\rho + b\rho(\nabla h)^2 \end{aligned} \tag{5.4}$$

The R.H.S. of this equation contains following contributions, a) advection of the height field by $\mathbf{n}$ via coupling parameter μ_3, b) membrane buckling due to active stresses $\nabla \cdot c\mathbf{n}$,(c) a symmetry allowed coupling between gradients of c and slope, c) membrane elasticity terms with surface tension Σ and bending rigidity κ (d) spontaneous curvature due to horizontal and vertical actin and, (e) symmetry allowed couplings to ρ.

The parameters $\mu_{1,2,3}$ are phenomenological parameters which appear in the dynamical equations as the coefficients of membrane slope. At first glance, the dependence on membrane slope via terms like $\mathbf{p} \cdot \nabla h$ seems to break the rotational invariance. In next section we show that these new coupling terms obey the required invariance stated in the beginning of this sectio.

5.3.2 Discussion of Coupling to the Membrane Slope

As stated earlier, the dynamical equations are required to obey the invariance under simultaneous rotations of the local membrane normal $\mathbf{N}$ and $\mathbf{P}$ implying that the variation $\delta(\mathbf{N} \cdot \mathbf{P}) = 0$. Also, there is no 'up-down' symmetry which allows for a linear term in $\delta(\mathbf{N} \cdot \mathbf{P})$ to be included in the dynamical equations. Further in Monger Gauge, $\mathbf{N} \approx \left(-\nabla h, \sqrt{1-(\nabla h)^2}\right)$ and $\mathbf{P} = (\mathbf{p}, p_z)$ where $p_z = \mathbf{N} \cdot \mathbf{P}$ and $p_{\perp i} = (\delta_{ij} - N_i N_j) P_j$. Using these, the term $\delta(\mathbf{P} \cdot \mathbf{N})$ produces following terms to the lowest orders

$$\begin{aligned} \delta(\mathbf{P} \cdot \mathbf{N}) &= \delta P \cdot \mathbf{N}_0 + \mathbf{P}_0 \cdot \delta \mathbf{N} \\ &= \delta \mathbf{P} \cdot \hat{z} + \mathbf{p}_{0\perp} \cdot \nabla_\perp h + p_z \sqrt{1-(\nabla_\perp h)^2} \end{aligned} \tag{5.5}$$

where $\mathbf{N}_0 = \hat{z}$. This implies that the terms of the form $\mathbf{p} \cdot \nabla h$ in the dynamical equations are consistent with the symmetry arguments.

Before proceeding further, we make a note of the other non-equlibrium driven systems where such coupling is present. In sedimenting lattice under the effect of gravity similar coupling between the in-plane diplacements and the vertical displacements gives rise to the clumping instability [13]. Similarly a slope dependent coupling is present in case of the

drifting polymers under the effect of an external field [14]. The common point in all these examples is the broken rotational invariance because of pressence of an external direction which in our case is provided by actin based cell propulsion on a substrate.

5.3.3 Mechanisms of Instabilities

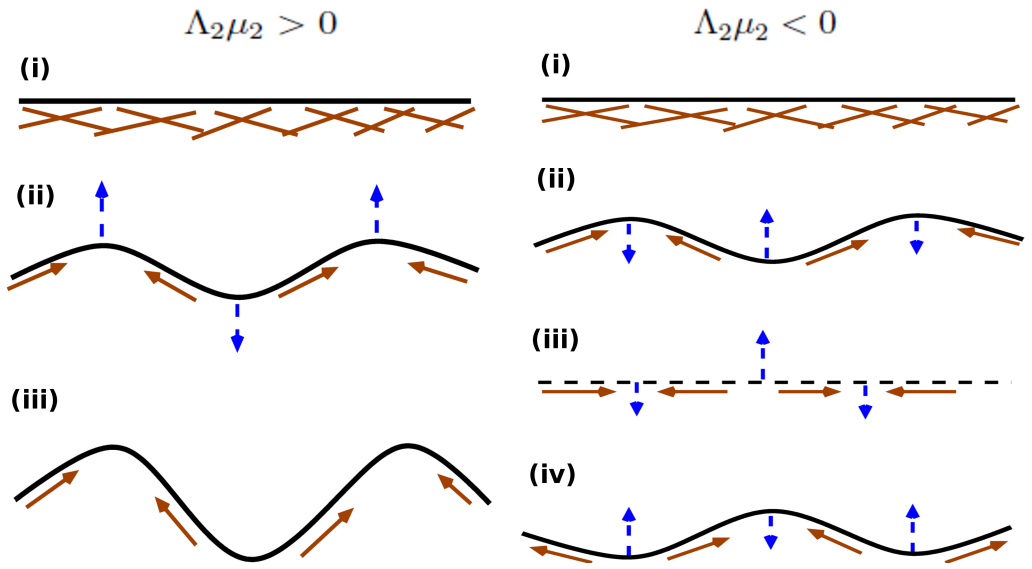

FIGURE 5.6: Mechanisms of instabilities and waves : (a) $\Lambda_2\mu_2 > 0$ (Left Panel) : A long wavelength perturbation to an initially flat membrane (i) re-orients the filaments (brown arrows) along the height gradient (ii). This creates non-zero divergence $\nabla \cdot c\mathbf{n}$ which further pushes membrane in the direction of blue-dotted making an initially flat membrane unstable (iii). (b) $\Lambda_2\mu_2 > 0$ (Right Panel): Figure illustrates the case when $\Lambda_2 < 0$ and $\mu_2 > 0$. A long wavelength perturbation will re-orient filaments along the height gradient as (a)(i-ii). However this will now pull the membrane in the direction shown by blue-dotted arrows reaching (iii). The arrangement of arrows in (iii) will give rise to instabilities as shown in (iv) giving rise to wave like behaviour.

Before analyzing the instabilities exhibited by a membrane coupled to cortical actin we ask the question : what mechanisms can give rise to the instabilities and waves ? There are various active mechanisms in the proposed framework which can lead to instabilities. The feedback between active current which is proportional to the polar orientation and the reorientation of filaments along the concentration gradients gives rise to density clumping and formation of asters [15]. Other mechanisms that can give rise to instabilities of a deformable membrane coupled with active fluid are listed below :

1. **Coupling between h and $\mathbf{p}$:** This coupling is incorporated in the parameters Λ_2 and μ_2 of Eqns. 5.3 and 5.4 respectively and is explained in Fig. 5.6. $\Lambda_2\mu_2 > 0$ makes

the membrane unstable while $\Lambda_2\mu_2 < 0$ leads the membrane to develop 'kinematic waves'.

2. **Coupling between h and c :** Coupling between height and concentration of horizontal actin filaments is via an active current proportional to the height gradient and the spontaneous curvature terms incorporated in the parameters μ_1 and κ_1 respectively. The fact that the current for actin filaments is proportional to the height gradients introduces interesting new and lower order instabilities and can lead to the membrane instabilities or waves of the acto-myosin concentration as well as of membrane height with growing amplitudes. The mechanism by which these are obtained is same as the situation depicted in Fig. 5.6 where the brown arrows now denote active current.

We now look at the differnt limits of the proposed dynamical equations.

5.4 Active Membrane

Integrating out the dynamics of in-plane concentration of horizontal actin and in-plane polar order parameter $\mathbf{p}$ gives rise to following set of coupled equations for shape and the vertical actin filaments concentration.

$$\partial_t h = g_1\nabla^2 h - \nabla^4 h - g_2\nabla^2\rho + g_3\rho + g_4\rho(\nabla h)^2 \tag{5.6a}$$

$$\partial_t \rho = -\nabla\cdot\left[B_1\rho^2\nabla h - B_2\nabla(\nabla^2 h) - \nabla\rho\right] \tag{5.6b}$$

Where new parameters are effective parameters obtained by integrating out the two fields and then rescaling. These equations are same as the equations for an active membrane with active forces normal to the membrane [16]. Thus the dynamics of an active membrane emerges from a passive membrane coupled to this active cortical fluid.

5.5 Instabilities of the Plasma Membrane and Cortical Actin

We now analyze the instabilities of a flat membrane with in-plane polar order parameter. In this section we work in the limit where the dynamics of concentration of vertical actin

is fast giving rise to a steady state concentration ρ_0 of vertical actin. This leads to steady state propulsion of the cell with a mean $|\mathbf{V}| \propto \rho_0$. With this, we are left with membrane height h over a reference plane and concentration c and polar orientation $\mathbf{p}$ of the horizontal actin. We apply perturbation of the form $c = c_0 + \delta c(\mathbf{x}, t)$, $\mathbf{p} = \mathbf{p}_0 + \delta\mathbf{p}(\mathbf{x}, t)$ and $h = h_0 + \delta h(\mathbf{x}, t)$ to the dynamical equations. We then expand these equations upto linear order in perturbation. Perturbations are then decomposed into fourier modes using $\delta c = \int d\mathbf{q} c_q e^{\imath \mathbf{q}\cdot\mathbf{x}}$ $\delta\mathbf{p} = \int d\mathbf{q}\mathbf{p}_q e^{\imath\mathbf{q}\cdot\mathbf{x}}$ and $\delta h = \int d\mathbf{q} h_q e^{\imath\mathbf{q}\cdot\mathbf{x}}$. The linearized equations for fourier amplitudes are given as

$$\partial_t \delta c = -v_0 c_0 \nabla\cdot\delta\mathbf{p} - v_0\mathbf{p}_0\cdot\delta c - \mu_1 c_0 \nabla\delta h + D\nabla^2\delta c \tag{5.7a}$$

$$\partial_t \delta\mathbf{p} = -\Lambda_1\mathbf{p}_0\cdot\nabla\delta\mathbf{p} + K_1\nabla^2\delta\mathbf{p} + K_2\nabla(\nabla\cdot\delta\mathbf{p}) + \mu_2 c_0\nabla\delta h + \zeta\nabla\delta c + (A - 3Bp_0^2)\delta\mathbf{p} \tag{5.7b}$$

$$\partial_t \delta h = -\mu_3\mathbf{p}_0\cdot\nabla\delta h - \Lambda_2 c_0\nabla\cdot\delta\mathbf{p} + \Sigma\nabla^2\delta h - \kappa_1\nabla^4\delta h \tag{5.7c}$$

5.5.1 Shape and Polar Order

5.5.1.1 Low Mean Concentration

As first step we first ignore the dynamics of concentration and focus on the instabilities that arise due to active dynamics of a membrane with in-plane vector field. Before proceeding with the analysis, note that the parameter A in Eqn. 5.7b is function of deviation of mean density of actin filaments from the Onsager value, denoted by c^*, at which transition from orientationally disordered to polar ordered phase takes place. We measure the concentration of actin filaments in units of c^* so that this transition takes place at $c_0 = 1$ where c_0 is the mean concentration of actin filaments. The parameter A changes its sign at $c_0 = 1$ and can be phenomenologically writtten as $A = A_0(c_0 - 1)$. We first fix $c_0 < 1$ so that $A < 0$. For this range of mean concentration the membrane is orientationally disordered. We ask whether a flat membrane with no orientational order is stable by applying perturbation to this state.

For this range of mean concentration the linearized equations for fourier amplitudes are

$$\partial_t \mathbf{p}_q = -Kq^2\mathbf{p}_q + A\mathbf{p}_q + i\mu_2 c_0 h_q \mathbf{q} \tag{5.8a}$$

$$\partial_t h_q = i\Lambda_2 c_0 \mathbf{q}\cdot\mathbf{p}_q - \Sigma q^2 h_q - \kappa q^4 h_q \tag{5.8b}$$

The eigenvalues of the stability matrix are given as (upto 4^{th} order in wavevector)

$$\Omega_1 = A - K_1 q^2 \tag{5.9a}$$

$$\Omega_2 = A - q^2\left(K_1 + \frac{\Lambda_2\mu_2 c_0^2}{A}\right) + q^4\frac{\Lambda_2\mu_2 c_0^2}{A}\left(AK_1 - A\Sigma - \Lambda_2\mu_2\right) \tag{5.9b}$$

$$\Omega_3 = -q^2\left(\Sigma + \frac{\Lambda_2\mu_2 c_0^2}{A}\right) - q^4\left(\kappa - \frac{\Lambda_2^2\mu_2^2 c_0^4}{A^3} + (K_1 - \Sigma)\frac{\Lambda_2\mu_2 c_0^2}{A^2}\right) \tag{5.9c}$$

For $A < 0$ the flat and disordered phase is stable when $\Lambda_2\mu_2 c_0^2 < \Sigma|A|$. For $\Lambda_2\mu_2 c_0^2 > \Sigma|A|$, the growth rate Ω_3 becomes positive for a band of wave vectors becomes unstable with fastest growing wave vector given by

$$q_{max} = \frac{A}{\sqrt{2}}\sqrt{\frac{A\Sigma + \Lambda_2\mu_2}{\Lambda_2^2\mu_2^2 c_0^4 - \kappa A^3 - A\Lambda_2\mu_2 c_0^2(K - \Sigma)}} \tag{5.10}$$

The growth rate showing instability is plotted in Fig. 5.7. This instability is expected to drive the membrane to form the tubules separated by a distance give by inverse of q_{max}^{-1} and is labelled in the phase diagram shown in Fig. 5.9.

5.5.1.2 High Mean Concentration

The mean concentration till now was such that $A < 0$ and the membrane did not have orientational order. Increasing mean concentration c_0 so that $A > 0$, leads to a zero wave vector instability in Ω_1 and the membrane develops macroscopic polar order with $|\mathbf{p}_0| = \sqrt{\frac{A}{B}}$. To analyse the stability of this phase we introduce perturbation to the flat membrane with polar order as $\mathbf{p} = \mathbf{p}_0 + \delta\mathbf{p}$ and $h = h_0 + \delta h$. Without loss of generality the direction of uniform polar order is taken to be parallel to $x-$axis. Linearized equations of motion for

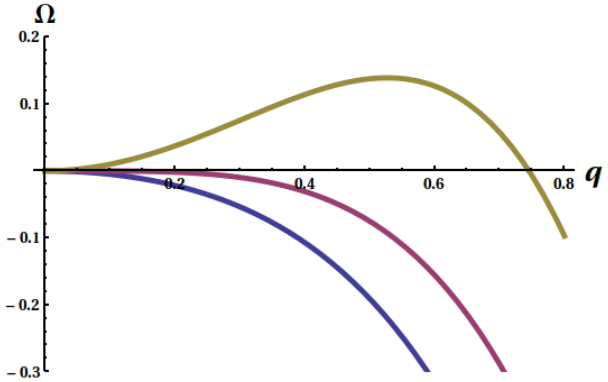

FIGURE 5.7: Low mean concentration of filaments : The unstable mode Ω_3 for three values of $\Lambda_2\mu_2$. The values of other parameters are selected as explained in the text.

the fourier amplitudes are given as

$$\partial_t p_{xq} = -\left(2A + i\Lambda_1\sqrt{\frac{A}{B}}q_x - K_1q^2 - K_2q_x^2\right)p_{xq} - K_2q_xq_yp_{yq} + i\mu_2c_0q_xh_q \quad (5.11a)$$

$$\partial_t p_{yq} = -\left(i\Lambda_1\sqrt{\frac{A}{B}}q_x - K_1q^2 - K_2q_y^2\right)p_{yq} - K_2q_xq_y\partial_{xq} + i\mu_2c_0q_yh_q \quad (5.11b)$$

$$\partial_t h_q = -i\Lambda_2c_0\left(q_xp_{xq} + q_yp_{yq}\right) - \left(\Sigma q^2 - i\mu_3\sqrt{\frac{A}{B}}q_x - \kappa q^4\right)h_q \quad (5.11c)$$

We denote a general perturbation $\mathbf{q} = (q_x, q_y) \equiv (q, \theta)$ in polar co-ordinates where $\theta = \arccos\left(\frac{\mathbf{p}_0\cdot\mathbf{q}}{|\mathbf{p}_0\cdot\mathbf{q}|}\right)$. Analyzing the instability of a general perturbation we find that the fastest growing wave vector is either parallel or perpendicular to the direction of order (Appendix B). Hence we analyze the cases of purely parallel and purely perpendicular perturbations. The growth rates of perturbations perpendicular to the ordering direction are given as

$$\Omega_1 = -2A - K_1q_y^2 \quad (5.12a)$$

$$\Omega_{2,3} = \pm q_y\sqrt{c_0^2\Lambda_2\mu_2} - \frac{K_1 + K_2 + \Sigma}{2}q_y^2 + \ldots \quad (5.12b)$$

For $A > 0$ uniformly polarized phase is stable for $\Lambda_2 = 0$. For $\Lambda_2\mu_2 < 0$ stability analysic predicts a pair of 'kinematic waves' transverse to ordering direction with velocities $\pm\sqrt{\Lambda_2\mu_2c_0^2}$. For $\Lambda_2\mu_2 > 0$, Ω_2 becomes positive with maximum growth rate occuring for a wave vector $q_{max} = \frac{\sqrt{\Lambda_2\mu_2c_0^2}}{K_1+K_2+\Sigma}$. This instability is expected to drive the membrane to develop ridges parallel to the direction of order. The mode showing instability is Ω_2, which is plotted as a

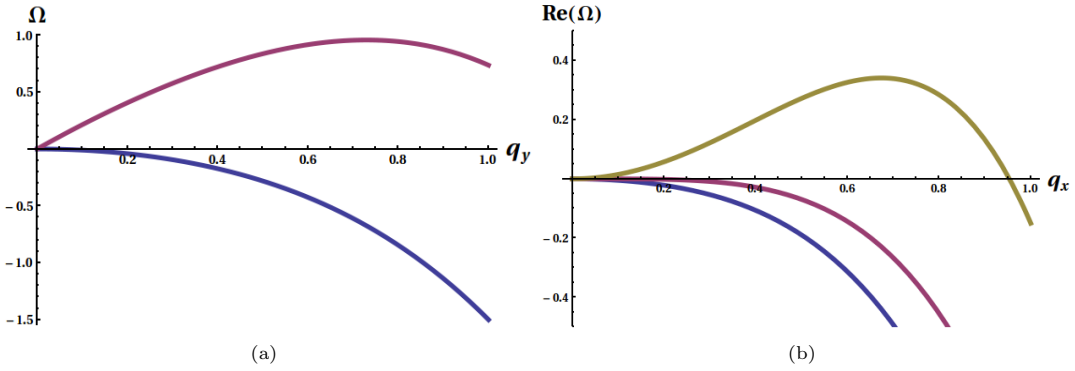

(a) (b)

FIGURE 5.8: Dispersion relation showing instability of flat membrane with polar order ($A > 0$). Growth rates when fastest growing wave vector is (a) perpendicular and (b) parallel to the direction of polar order.

function of q_y in Fig. 5.8(a). The corresponding region of instablity is labelled as stationary ridges in the phase diagram of Fig. 5.9.

The growth rates of perturbations parallel to ordering direction are given as

$$\Omega_1 = -i\Lambda_1 q_x\sqrt{\frac{A}{B}} - K_1 q_x^2 \tag{5.13a}$$

$$\Omega_2 = -i\mu_3 q_x\sqrt{\frac{A}{B}} + q_x^2\left(\frac{\Lambda_2\mu_2 c_0^2}{2A} - \Sigma\right) \tag{5.13b}$$

$$\Omega_3 = -2A - i\Lambda_1 q_x\sqrt{\frac{A}{B}} - q_x^2\left(K_1 + K_2 + \frac{\Lambda_2\mu_2 c_0^2}{2A}\right) \tag{5.13c}$$

Ω_1 and Ω_3 do not exhibit any instability when $A < 0$. The mode Ω_2 is positive when $\Lambda_2\mu_2 c_0^2 > 2A\Sigma$ (Fig. 5.8(b)). This growth rate has non-zero imaginary part implying that the instability travels as it grows. Within linear regime this instability will drive the membrane towards formation of waves whos amplitude grows as they travel. This instability occurs in the shaded region of the phase diagram displayed in Fig. 5.9. In the shaded region of the phase diagram the growth rates of Eqns. (5.12b) and (5.13b) both are positive. While linear stability analysis will predict that the a wave vector with faster growth rate will be picked up in this regime, the final steady state will be determined by non-linearities. The phase diagram based on the stability analysis in this part is displayed in Fig. 5.9 which we explain in following section.

5.5.2 Phase Diagram

The results from linear stability analysis using coupled dynamics of height and polar order parameter are summarized in phase diagram fig 5.9 in space of mean density c_0 of actin filaments and the parameter $\lambda_2\mu_2$. As stated earlier, increasing mean density of actin filaments beyond a critical density c^* leads to transition from orientationally disordered state to ordered state with uniform polar order. This boundary is plotted as black vertical line in the phase diagram. Below $c_0 = 1$, A is negative and the orientationally disordered state of the flat membrane is stable. For low values of mean cocentration, membrane with no polar order is unstable beyond $\Lambda_2\mu_2 > \frac{A_0|(c_0-1)|\Sigma}{c_0^2}$. This boundary is plotted as a solid-green line. Beyond $c_0 = 1$ membrane develops uniform polar order. In this regime of mean concentration $\Lambda_2\mu_2 < 0$ region exhibits 'kinematic waves'. For $\Lambda_2\mu_2 > 0$ the membrane with uniform polar order is unstable and develops ridges parallel to the direction of order. Increasing $\Lambda_2\mu_2$ further leads to another instability. For $\Lambda_2\mu_2 > \frac{2A_0(c_0-1)\Sigma}{c_0^2}$ (solid red line) the instability corresponding to the waves with growing amplitude appears. In the shaded region both these instabilities exist and the one with the faster growth rate is picked up.

5.5.3 Shape and Acto-myosin Concentration

To study the effects of concentration of acto-myosin on the instabilities we now include the dynamics of concentration of horizontal actin filaments. For simplicity, we include the dynamics of concentration in the regime of high mean concentration of filaments so that the amplitude fluctuations decay with a time scale of A^{-1} and $\mathbf{p} = \sqrt{\frac{A}{B}}\hat{x} + \delta p_y \hat{y}$. Linearized equations for the fourier amplitudes of perturbations in concentration, angle fluctuations and height are given as following

$$\partial_t c_q = -\left(Dq^2 + iv_0\sqrt{\frac{A}{B}}q_x\right)c_q - iv_0c_0q_yp_{yq} + \mu_1c_0q^2h_q \tag{5.14a}$$

$$\partial_t p_{yq} = i\zeta q_y c_q - \left(K_1q^2 + i\Lambda_1\sqrt{\frac{A}{B}}q_x\right)p_{yq} + ic_0\mu_2q_yh_q \tag{5.14b}$$

$$\partial_t h_q = \left(\kappa_1q^2 - i\Lambda_2\sqrt{\frac{A}{B}}q_x\right)c_q - ic_0\Lambda_2q_yp_{yq} - \left(i\mu_3\sqrt{\frac{A}{B}}q_x - \Sigma q^2\right)h_q \tag{5.14c}$$

Here again we follow the similar analysis of looking at the perturbations with wave vector parallel and perpendicular to the ordering directions separately. If fastest wave vector is perpendicular to the ordering direction the growth rate Ω_2 of Eqn. (5.12b) gets modified to $\sqrt{v_0\zeta + c_0^2\Lambda_2\mu_2}q_y$ upto linear order. Thus any non-zero contractility ζ or Λ_2 makes the flat homogeneous membrane unstable. If the fastest wave vector is parallel to the ordering direction the growth rates are modified as follows

$$\Omega_1 = -\left(K_1 q_x^2 + i\Lambda_1\sqrt{\frac{A}{B}}q_x\right)p_{yq} \tag{5.15a}$$

$$\Omega_2 = -iq_x v_0\sqrt{\frac{A}{B}} + q_x^2\left(-D + \frac{c_0^2\Lambda_2\mu_1}{v_0 - \mu_3}\right) + \dots \tag{5.15b}$$

$$\Omega_3 = -iq_x\mu_3\sqrt{\frac{A}{B}} + q_x^2\left(\Sigma - \frac{c_0^2\Lambda_2\mu_1}{v_0 - \mu_3}\right) + \dots \tag{5.15c}$$

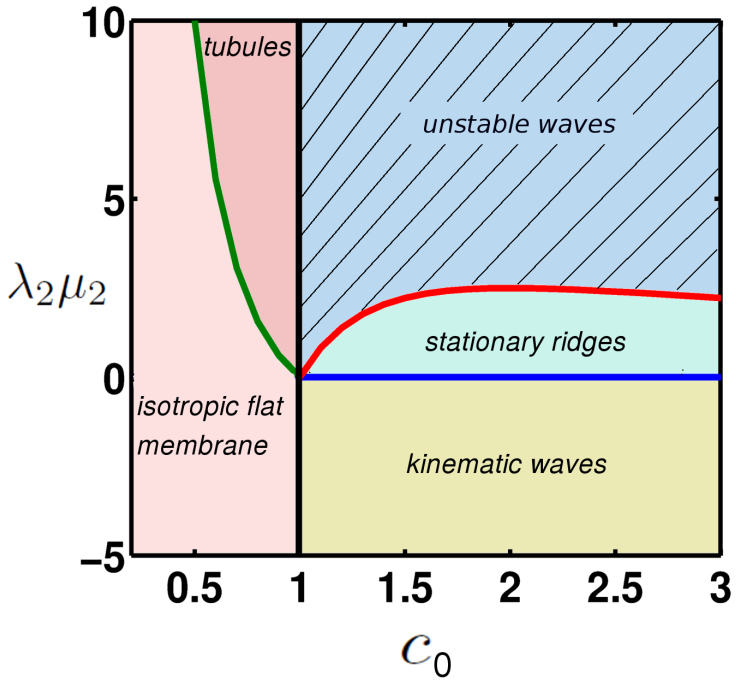

FIGURE 5.9: Phase diagram obtained from linear stability analysis about flat membrane with no orientational order. The phase boundaries have been obtained from linear stability analysis as explained in the text, and the corresponding phases are predicted from the nature of dispersion relations. The phase diagram shows interesting instabilities including : *tubules, kinematice waves, ridges* and *waves with growing amplitude.*

First mode Ω_1 does not show instability. If $v_0 > \mu_3$, second mode is unstable when $c_0^2\Lambda_2\mu_1 > D(v_0 - \mu_3)$, while if $v_0 < \mu_3$ third mode Ω_3 is unstable when $c_0^2\Lambda_2\mu_1 > \Sigma(\mu_3 - v_0)$. In the former case the instability competes with diffusion coefficient to build while in the latter case instability competes with the surface tension Σ. These instabilities travel as they grow and suggest travelling waves of the acto-myosin concentration and membrane height, a situation realized in various experiments described in the beginning of this chapter. Note that for $v_0 = \mu_3$ the lowest order expansion in powers of q_x gives $\pm q_x^{3/2}\sqrt{c_0\sqrt{\frac{A}{B}}\Lambda_2\mu_1} - i\mu_3\sqrt{\frac{A}{B}}q_x - \frac{D+\Sigma}{2}q_x^2$.

5.6 Current and Future Directions

In this chapter, we have explored in detail, long wavelength instabilities of a membrane coupled to the cortical actin. Our model does not make any assumption about the nature of specific interactions between the membrane proteins and the cortical actin, which go into setting the parameters of the theory. Under the influence of active currents and stresses active composite membrane self organizes into tubules, kinematic waves, ridges, ruffles and unstable waves. This analysis sets the stage for a diverse array of possible directions.

5.6.1 Direct Numerical Simulations

The results in this study have been obtained from linearized treatment of the dynamical equations. Although these results suggest the existence of travelling solutions and waves, these need to be confirmed from the direct numerical simulations to be as the steady states. A one mode Galerkin- truncated version of the dynamical equations also suggests the existence of waves [12]. Numerical simulation of these equations appears in [12] and confirms the existence of spontaneous oscillations. In addition, solutions with growing amplitudes drive the system to a state which will lead to spontaneous generation of waves and acts as a '*w*ave generator' state. This result has significance in the context of the ruffles and waves generated in the lamellipodia that we described in the beginning of this chapter.

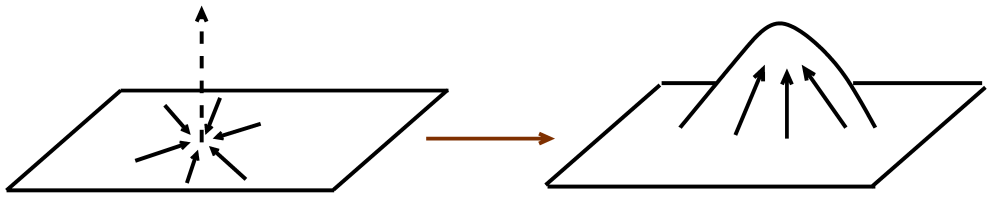

FIGURE 5.10: Out of plane buckling of the membrane under radial contractile stresses.

5.6.2 Travelling Actin Waves

The non-steady actin travelling waves (t-waves) are observed in a variety of systems, as discussed in the beginning of this chapter [5]. Various theoretical models have been proposed to explain these waves.The work discussed in this chapter provides a generic framework to obtain actin and membranal waves. However, in order to make closer contact to experiments the parameters of our theory are to be obtained from context-specific microscopic models.

5.6.3 Membrane Buckling Under Horizontal Stress

Asters emerge as steady state pattern as a result of coupled dynamics of concentration and polar orientation describing cortical actin fluid [15]. Inhomogeneities in concentration field act as source of asters since in steady state $K_1\nabla^2\mathbf{p} = -\zeta\nabla c$ leading to non-zero density of asters defined as $\rho_{aster} = -c\nabla\cdot\mathbf{p}$. The density of asters can be altered by modifying contractile activity ζ by changing local acto-myosin concentration. The size of these asters is fixed by balance of current in Eqn. 5.1. An aster configuration has radial contractile stresses and active currents towards the aster core. This can lead to the out of plane buckling of membrane via the term $-\Lambda_2\nabla\cdot c\mathbf{p}$ when the composite membrane is in the regime of elastic response.

5.6.4 Active Elastomeric Membrane

Throughout this thesis, we have treated the cortical actin as an active fluid. This treatment is valid for the time scales that are large than the remodelling time scale of the cortical actin (typically of the order of 10s). However, in addition, the cortical actin consists of a static crosslinked meshwork. On time scales larger than the time scales of cross-linker dynamics,

we assumed that the dynamics of this elastic crosslinked meshwork is fast and averages out to give renormalize values of the parameters. However, the effect of contractile stresses on the crosslinked meshwork can be explicitly taken into account and is a natural direction to take following the analysis presented in this thesis.

Bibliography

[1] H.G. Dobereiner, B.J. Dubin-Thaler, J.M. Hofman, H.S. Xenias, T.N. Sims, G. Giannone, M.L.Dustin, C.H. Wiggins and M.P. Sheetz, Phys. Rev. Lett. **97**, 038102(2006).

[2] E.L. Barnhart, K.C. Lee, K. Keren, A. Mogilner and J.A. Theriot, PLoS Biol. **9**, e1001059(2011).

[3] K.O. Okeyo, T. Adachi, J. Sunaga and M. Hojo, Journal of Biomechanics **42**, 2540(2009).

[4] D.T. Burnette, S. Manley, P. Sengupta, R. Sougrat, M.W. Davidson, B. Kachar and J.Lippincott-Schwartz, Nat. Cell Biol. **13**, 371(2011).

[5] J. Allard and A. Mogilner, Curr Opin Cell Biol **25**:1-9 (2011).

[6] G.L. Ryan, H.M. Petroccia, N. Watanabe and D. Vavylonis, Biophys. J. **102**, 1493(2012).

[7] A.C. Reymann, R. Boujemaa-Paterski, J.L. Martiel, C.guerin, W. Cao, H.F¿ Chin, E.M. De La Cruz. M. Thery and L. Blanchoin, Science **336**, 1310(2012).

[8] R. Shlomovitz and N. Gov, Phys. Rev. Lett. **98**, 168103(2007).

[9] N.S. Gov and A. Gopinathan, Biophys J. **90**, 454(2006).

[10] K. Doubrovinski and K. Kruse, Phys, Rev. Lett. **107**, 258103(2011).

[11] O.D. Weiner, W.A. Marganski, L.F. Wu, S.J. Altschuler and M.W. Kirschner, PloS Biol. **5**, e221(2007).

[12] A. Maitra, P. Srivastava, S. Ramaswamy and M. Rao, Manuscript under preparation.

[13] R. Lahiri, M. Barma and S. Ramaswamy, Phys. Rev. E **61**, 1648(2000).

[14] D. Ertas and M. Kardar, Phys. Rev. E **48**, 1228(1993).

[15] K. Gowrishankar and M. Rao, arXiv:1201.3938.

[16] S. Ramaswamy, J. Toner and J. Prost, **84**, 3494(2000).

Appendix A

Dynamical Equations in the Spherical Geometry

A.1 Form of the Dynamical equations in Spherical Geometry

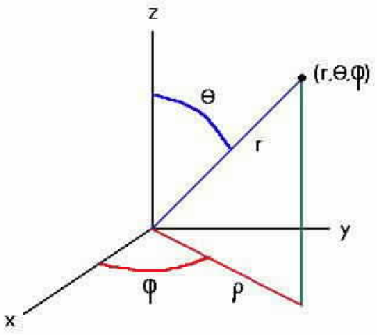

FIGURE A.1: Spherical co-ordinate system

Fig. A.1 shows the spherical coordinate system. Position of a point on the surface of sphere with radius R is characterized by polar and azimuthal angles denoted by θ and ϕ respectively. Expressions for the first and second order differential operators on the surface of a spherical cell are provided below [1].

1. Gradient of the concentration c

$$\nabla c = \hat{e}_\theta \frac{1}{R}\frac{\partial c}{\partial \theta} + \hat{e}_\phi \frac{1}{R\sin\theta}\frac{\partial c}{\partial \phi} \tag{A.1}$$

2. Divergence of the vector field $\mathbf{n}$

$$\nabla \cdot \mathbf{n} = \frac{1}{R\sin\theta}\left[\frac{\partial}{\partial\theta}\left(\sin\theta n_\theta\right) + \frac{\partial n_\phi}{\partial\phi}\right] \tag{A.2}$$

3. Scalar Laplacian

$$\nabla^2 c = \frac{1}{R^2\sin\theta}\left[\frac{\partial}{\partial\theta}\left(\sin\theta\frac{\partial c}{\partial\theta}\right) + \frac{1}{\sin\theta}\frac{\partial^2 c}{\partial\phi^2}\right] \tag{A.3}$$

4. Vector Laplacian acting on the vector $\mathbf{n}$

$$\nabla^2\mathbf{n}|_\theta = \nabla^2 n_\theta - \frac{1}{R^2\sin^2\theta}n_\theta - \frac{2\cos\theta}{R^2\sin^2\theta}\frac{\partial n_\phi}{\partial\phi} \tag{A.4}$$

$$\nabla^2\mathbf{n}|_\phi = \nabla^2 n_\phi - \frac{1}{R^2\sin^2\theta}n_\phi + \frac{2\cos\theta}{R^2\sin^2\theta}\frac{\partial n_\phi}{\partial\phi} \tag{A.5}$$

Using above expressions for the differential operators form of the dynamical equation for concentration is obtained as

$$\begin{aligned}
\partial_t c &= -\frac{1}{R\sin\theta}\left[\frac{\partial}{\partial\theta}\left(\sin\theta J_\theta\right) + \frac{\partial J_\phi}{\partial\phi}\right], \quad \text{where} \\
J_\theta &= v_\theta c n_\theta - \frac{D}{R}\frac{\partial c}{\partial\theta}, \quad \text{and} \\
J_\phi &= v_\phi c n_\phi - \frac{D}{R\sin\theta}\frac{\partial c}{\partial\phi}
\end{aligned} \tag{A.6}$$

Similarly the equation for polar orientation is given as

$$\partial_t n_\theta = \frac{K_1}{R^2 \sin\theta}\frac{\partial}{\partial\theta}\left(\sin\theta\frac{\partial n_\theta}{\partial\theta}\right) - \frac{K_1 n_\theta}{R^2\sin^2\theta} - \frac{2\cos\theta}{R^2\sin^2\theta}\frac{\partial n_\phi}{\partial\phi} + \frac{\zeta}{R}\frac{\partial c}{\partial\theta} + (\alpha + \frac{\gamma_\theta}{R} - \beta|\mathbf{n}|^2)n_\theta \tag{A.7}$$

$$\partial_t n_\phi = \frac{K_1}{R^2 \sin\theta}\frac{\partial}{\partial\theta}\left(\sin\theta\frac{\partial n_\theta\phi}{\partial\theta}\right) - \frac{K_1 n_\phi}{R^2\sin^2\theta} + \frac{2\cos\theta}{R^2\sin^2\theta}\frac{\partial n_\theta}{\partial\phi} + \frac{\zeta}{R\sin\theta}\frac{\partial c}{\partial\theta} + (\alpha + \frac{\gamma_\phi}{R} - \beta|\mathbf{n}|^2)n_\theta \tag{A.8}$$

Clubbing together the linear terms in $\mathbf{n}_\theta$ and n_ϕ we obtain the renormalization of α to α_θ and α_ϕ as $\alpha_{\theta,\phi} = \alpha - K_1/(R^2\sin^2\theta) + \gamma_{\theta,\phi}/R$

Bibliography

[1] G.B. Arfken, H.J. Weber and F. Harris, *Mathematical Methods for Physicists, 5^{th} edition*, Academic Press.

Appendix B

Instabilities of flat membrane with uniform polar order

B.1 Analysis of a general perturbation

In this section we analyze the instability of a general peturbation as mentioned in Sec. 4.5. The general perturbation applied to a flat membrane with uniform polar order along x-axis can be represented by magnitude q and an angle θ where $\theta = \arccos(\frac{\mathbf{p}_0 \cdot \mathbf{q}}{|\mathbf{p}_0 \cdot \mathbf{q}|})$, where $\mathbf{p}_0 = \sqrt{\frac{A}{B}}\hat{x}$ (The notations are same as those used in the chapter 4). Since we are concerned with only the angle dependence of the unstable wave vector and its growth rate we choose values of of other parameters corresponding to stable polar ordered phase. Out of the three modes one has non-zero zeroth order term and does not become unstable. Dispersion relation for other two modes are given below (upto linear order in q) :

$$\Omega_{1,2} = -\frac{i}{2}\left(1+\mu_3\right) q \cos\theta + Bq \tag{B.1}$$

where,

$$B = \frac{q}{2\sqrt{2}}\sqrt{4\lambda_2\mu_2\left(1-\cos 2\theta\right) - \left(\mu_3 - 1\right)^2\left(1+\cos 2\theta\right)} \tag{B.2}$$

For $\theta < \theta_c$ where $\theta_c = \frac{1}{2} \arccos \frac{4\lambda_2\mu_2 - (\mu_3 - 1)^2}{4\lambda_2\mu_2 + (\mu_3 - 1)^2}$ B is imaginary and contributes to the velocity of travelling wave. In this case the growth of instability is determined by quadratic order term in the expansion. For $\theta > \theta_c$ second term is real and one of the modes becomes unstable. However the fastest growing wave vector has maximum along $\theta = \frac{\pi}{2}$ (Fig. B.1). A plot of B for $\theta > \theta_c$ and the wave velocity for $\theta < \theta_c$ is given in Fig. B.1.

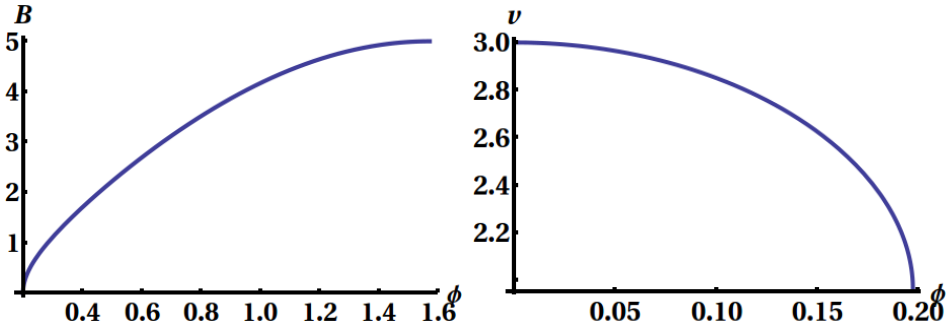

(a) (b)

FIGURE B.1: Coefficient of linear term in Eqn. with θ for (a) $\theta > \theta_c$ and (b) $\theta < \theta_c$